Data Evaluation and CNGS Beam Localization with the Precision Tracker of the OPERA Detector

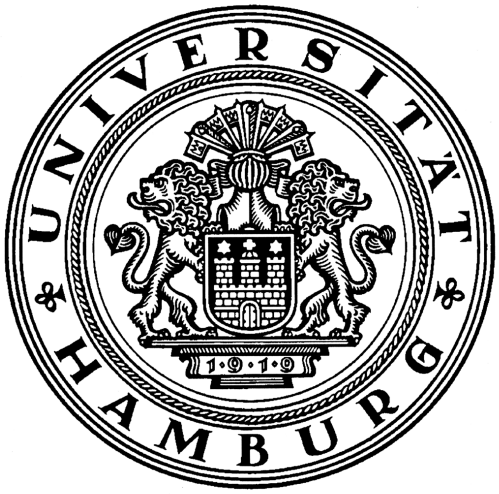

Diplomarbeit
am Institut für Experimentalphysik
der Universität Hamburg

vorgelegt von
Daniel Bick

14. Februar 2007

Gutachter der Diplomarbeit

Prof. Dr. Caren Hagner
Prof. Dr. Walter Schmidt-Parzefall

Abstract

In this diploma thesis, the data evaluation for the OPERA precision tracker is presented. Furthermore investigations of a precise CNGS beam localization with the precision tracker are performed. After an overview of past and present developments in neutrino physics, the OPERA detector is presented in this thesis. Emphasis is given to the precision tracker which has been partly commissioned in the end of the last year. A first analysis of the functionality with cosmic muons has been performed, as well as the inclusion of data in the OPERA software framework. Within this thesis some useful tools have been developed which are also presented. Finally, divergence effects from the nominal beam line of the CNGS neutrino beam and possible detection with the precision tracker are studied.

Zusammenfassung

Diese Diplomarbeit beschreibt die Datenauswertung sowie Untersuchungen zu einer präzisen Ortsbestimmung des CNGS Neutrinostrahls mit Hilfe des OPERA Driftröhrenspektrometers. Nach einem Überblick über geschichtliche und aktuelle Entwicklungen in der Neutrinophysik wird der OPERA Detektor in dieser Diplomarbeit kurz vorgestellt. Der Schwerpunkt liegt dabei auf dem Driftröhrenspektrometer, welches im vergangenem Jahr teilweise in Betrieb genommen werden konnte. Erste Analysen zur Funktionsweise mit kosmischen Myonen werden vorgestellt, ebenso die Einbindung der Daten in die OPERA Software Umgebung. Im Rahmen der Arbeit wurden einige nützliche Anwendungen erstellt, die präsentiert werden. Abschließend beschäftigt sich die Arbeit mit Auswirkungen eines von der nominellen Strahlachse abweichenden CNGS Neutrinostrahls auf das Neutrinospektrum sowie dessen Nachweismöglichkeiten durch das Driftröhrenspektrometer.

Contents

Chapter 1

Introduction

With the evidence for atmospheric neutrino oscillations in 1998 by the Super-Kamiokande experiment and the confirmation in the solar sector by the SNO experiment in 2002, the existence of non vanishing neutrino masses has now been shown and has since been confirmed by various other neutrino oscillation experiments. Yet, many related questions are still left unanswered and new ones are opened. The determination of these masses is one of the major challenges in current neutrino and astrophysics, as well as the question on how many neutrino species there are. The existence of non zero neutrino masses can only be explained by physics beyond the standard model.

The determination of neutrino oscillation parameters can only give constraints on the squared mass splittings but does not allow to determine absolute masses. Still, lowering these constraints helps understanding the behavior of neutrinos and a variety of experiments is currently searching for neutrino oscillations. From the deficit of atmospheric muon neutrinos observed by the Super-Kamiokande experiment, the mixing angle θ_{23} and the corresponding squared mass splitting Δm^2_{23} could already be pinned down quite well. Flavor change of atmospheric muon neutrinos is observed to be dominated by $\nu_\mu \rightarrow \nu_\tau$ oscillations which could as yet only be derived from observed disappearance of muon neutrinos. The OPERA experiment is designed to directly look for τ-appearance in a muon neutrino source. Atmospheric muon neutrinos are therefore *replaced* by an intense ν_μ source, provided by the CNGS beam shooting muon neutrinos from CERN to the Gran Sasso underground laboratory in Italy. For τ detection, a target of 1.8 ktons of lead interleaved with photographic emulsions is used in a hybrid detector. The experiment is expected to confirm the $\nu_\mu \rightarrow \nu_\tau$ oscillations observed in the atmospheric sector and measure $\sin^2 2\theta_{23}$ and $|\Delta m^2_{23}|$ within 10% of accuracy if $|\Delta m^2_{23}| > 10^{-3}\,\mathrm{eV}^2$.

In Chapter 2, this thesis starts with a summary of the current knowledge of neutrinos which is accompanied by a look at important historical and present experiments in this field. In the third chapter the OPERA detector is described. An emphasis is given to the muon spectrometer, especially the precision tracker developed and assembled by the University of Hamburg in cooperation with ITEP Moscow. Despite of the small neutrino cross-sections, a huge amount of data will be produced in the OPERA experiment which has to be stored, processed and analyzed. For the latter, the software package OpRelease is being developed of which the main characteristics are described in Chapter 4.

The inclusion of the precision tracker into the interface for converting raw data to a format readable by OpRelease has been done within this thesis. First characteristics

of the precision tracker with data from the commissioning have been analyzed and are presented in Chapter 5.

The OPERA detector operates at a baseline of $L = 732\,\text{km}$ from CERN. At these distances, even small misalignments of the beam line and hence false pointing can have immense effects on the neutrino flux and spectrum at the target. The effects of such a misalignment and the possibility of their detection with the precision tracker are investigated in Chapter 6.

Finally, a summary and outlook are given in Chapter 7.

Chapter 2

Neutrinos in and beyond the Standard Model

This chapter gives a short overview of neutrino physics. Firstly the standard model of elementary particles is briefly discussed. After that, a closer look on neutrinos and their properties is taken. The theory of neutrino oscillation is then explained and different neutrino experiments are summarized. At the end of this chapter neutrino masses are discussed.

2.1 The Standard Model of Elementary Particles

The standard model of particle physics describes the known elementary particles and their interactions. It contains twelve fundamental fermionic particles and their corresponding antiparticles. Interactions between these particles are mediated by gauge bosons. The known fundamental fermions are divided into two groups: six quarks and six leptons.

2.1.1 Forces

The standard model of particle physics comprises the theory of strong, weak and electromagnetic interactions of elementary particles. It is extraordinary successful in explaining data from various particle physics experiments. The particle interactions are described in terms of gauge theories, each interaction is mediated by different gauge bosons acting as its *force carrier*. Although the standard model does not explain gravity, it is mentioned here for completeness.

Gravity

The gravitational force is responsible for the attraction of masses. It was first described by Newton's law of universal gravitation and generalized in Einstein's general theory of relativity. Unlike to the other forces in the standard model, it is not yet described in terms of a gauge theory and there is as yet no evidence for a mediating particle for gravity. For this, the graviton has been postulated as a massless spin 2 particle, but has not been observed yet. Besides that, gravitational interactions between elementary

particles are of the order 10^{-40} smaller compared to the other forces so that they can usually be neglected.

Electromagnetic interactions

The electromagnetic force is mediated by the exchange of massless spin 1 bosons called photons. It mediates between electrically charged particles and can be observed e.g. as Coulomb forces, Lorentz forces or magnetism.

Weak interactions

The weak force is mediated by the $W^{\pm}$ (charged current) and Z^0 (neutral current) bosons. They couple to all leptons and quarks and to each other. Due to the high masses of the W and Z of around 90 GeV, weak interactions have a short range. The most familiar effect of the weak force is the beta decay. Weak interactions are the only interactions neutrinos take part in, hence they are of special importance in this thesis. Another distinctiveness of the weak force is its ability to change the flavor of a particle. Whenever a charged current process occurs in semi-leptonic or hadronic processes, a change of flavor is involved. There are no flavor changing neutral currents and also the lepton numbers (L_e, L_μ, L_τ) are conserved. Some more detailed aspects of weak interactions, especially for neutrino physics will be discussed in Section 2.2.1.

Electroweak unification

Electromagnetic and weak interactions have been combined in the electroweak theory. It states that weak and electromagnetic interactions are just two low energy aspects of the same force. According to the theory developed by Sheldon Glashow, Abdus Salam and Steven Weinberg in 1968, $W^{\pm}$ and Z^0 bosons and the photon are just superpositions of four gauge bosons W^1, W^2, W^3 and B [1].

Strong interactions

The strong force is much stronger than the electroweak forces, but acts only at a short range. The strong force is carried by (eight different) gluons which couple to the so-called color charge of a particle. There are three different colors (red, green, blue) and only quarks and gluons themselves carry this kind of charge. The theory of strong interactions is called *Quantum Chromodynamics* (QCD) and will not be discussed further in this thesis.

2.1.2 Quarks and Leptons

Six different types of quarks as well as leptons have been found in nature which are each arranged in three weak isospin doublets often called families or generations. Each particle has certain associated quantum numbers, listed in Table 2.1, which are generally conserved when this particle interacts. A quark doublet consists of a quark with charge $\frac{2}{3}$ and its *partner* with charge $-\frac{1}{3}$, a lepton doublet is made up of a charged lepton l and a neutrino ν_l:

	L	L_e	L_μ	L_τ	B	I_3	C	S	T	B^*	T_3	q
ν_e	1	1	0	0	0	0	0	0	0	0	$+\frac{1}{2}$	-1
e^-	1	1	0	0	0	0	0	0	0	0	$-\frac{1}{2}$	0
ν_μ	1	0	1	0	0	0	0	0	0	0	$+\frac{1}{2}$	-1
μ^-	1	0	1	0	0	0	0	0	0	0	$-\frac{1}{2}$	0
ν_τ	1	0	0	1	0	0	0	0	0	0	$+\frac{1}{2}$	-1
τ^-	1	0	0	1	0	0	0	0	0	0	$-\frac{1}{2}$	0
u	0	0	0	0	$\frac{1}{3}$	$\frac{1}{2}$	0	0	0	0	$+\frac{1}{2}$	$\frac{2}{3}$
d	0	0	0	0	$\frac{1}{3}$	$-\frac{1}{2}$	0	0	0	0	$-\frac{1}{2}$	$-\frac{1}{3}$
c	0	0	0	0	$\frac{1}{3}$	0	1	0	0	0	$+\frac{1}{2}$	$\frac{2}{3}$
s	0	0	0	0	$\frac{1}{3}$	0	0	-1	0	0	$-\frac{1}{2}$	$-\frac{1}{3}$
t	0	0	0	0	$\frac{1}{3}$	0	0	0	1	0	$+\frac{1}{2}$	$\frac{2}{3}$
b	0	0	0	0	$\frac{1}{3}$	0	0	0	0	-1	$-\frac{1}{2}$	$-\frac{1}{3}$
strong	n/a	n/a	n/a	n/a	yes	yes	yes	yes	yes	yes	yes	yes
em	yes	yes	yes	yes	yes	yes	yes	yes	yes	yes	yes	yes
weak	yes	yes	yes	yes	yes	no	no	no	no	no	yes	yes

Table 2.1: Properties of quarks and leptons and their conservation with respect to the interactions. L is the lepton number, B the baryon number, I_3 is the third isospin component, T_3 the third component of the weak isospin, C, S, T and B^* denote charm, strangeness, topness and beauty (bottomness) respectively. q is the electric charge in units of e. For the corresponding antiparticle a change in all signs applies.

$$\begin{pmatrix} u \\ d \end{pmatrix} \qquad \begin{pmatrix} s \\ c \end{pmatrix} \qquad \begin{pmatrix} t \\ b \end{pmatrix}$$

$$\begin{pmatrix} \nu_e \\ e^- \end{pmatrix} \qquad \begin{pmatrix} \nu_\mu \\ \mu^- \end{pmatrix} \qquad \begin{pmatrix} \nu_\tau \\ \tau^- \end{pmatrix}$$

Each particle has a corresponding antiparticle with the same mass and opposite sign for charge like quantum numbers. Free quarks cannot be observed, only *white*[1] bound states occur in nature. A bound quark state is called a hadron, a state of three quarks is called baryon whereas a quark-antiquark combination goes by the name meson. Out of the six quarks, three with equal weak isospin have weak eigenstates different from their strong force eigenstates. Weak and strong force eigenstates are connected by the Cabibbo-Kobayashi-Maskawa matrix V_{CKM}, each matrix element being connected to the strength of flavor changing weak interactions.

2.2 Neutrinos

The neutrino was first postulated by Wolfgang Pauli in 1930 [2]. To explain the continuous energy spectrum of electrons in β decays he assumed a neutral, invisible particle to

[1] A bound state is considered white when it contains either one quark of each color or a quark antiquark combination of the same color.

take part in the process. This additional particle would also account for the missing angular momentum observed. Pauli called the particle "neutron" but is was later renamed neutrino. After their introduction, neutrinos soon became well established in modern physics, although it was not until 1956 that the first neutrino was actually discovered by Frederick Reines and Clyde L. Cowan in an experiment called "Project Poltergeist" [3]. At the Savannah River reactor in the US state of South Carolina, they succeeded to observe the inverse beta-decay:

$$\bar{\nu}_e + p \rightarrow e^+ + n$$

Reines and Cowan arranged to detect the γ-emission following the capture of the neutron in a nucleus, which together with two photons from the annihilation of the positron with an electron gave a distinct signature for the process.

In 1962 Leon M. Lederman, Melvin Schwartz and Jack Steinberger showed that more than one type of neutrino exists. By studying the decay of pions, they observed that the emitted neutrino only reacts with muons but not with electrons. Hence the neutrino involved had to be different from the one known from β-decays - the muon-neutrino ν_μ was discovered [4]. After the discovery of a third charged lepton (the τ) in 1975 at SLAC[2] [5], it was also expected to have an associated neutrino. The ν_τ was discovered by the DONUT[3] experiment at Fermilab in 2000 [6].

The number of light[4] neutrino types N_ν has been determined by various experiments. The most precise measurements come from studies of Z production in e^+e^- collisions at LEP[5] at CERN[6]. In the reaction $e^+e^- \rightarrow Z^0 \rightarrow f\bar{f}$, where f is an elementary fermion, the total decay width as well as the partial widths for charged leptonic and hadronic events can be measured, hence the width for the *invisible* neutrinos can be determined. By comparing this to the theoretical expected decay width of neutrinos shown in Figure 2.1, one can calculate N_ν. The process has been measured by the LEP experiments ALEPH, DELPHI, L3 and OPAL which have obtained a combined result of $N_\nu = 3.00 \pm 0.08$ [8].

2.2.1 Weak Interactions Revisited - Charge Conjugation and Parity

Helicity and chirality

As mentioned before, neutrinos are fermionic and hence spin $\frac{1}{2}$ particles. Chirality is defined as the projection of a particle's spin $\mathbf{s}$ on its momentum $\mathbf{p}$ with the helicity operator λ:

$$\lambda = \mathbf{s} \cdot \frac{\mathbf{p}}{|\mathbf{p}|}$$

In 1958, Goldhaber succeeded to measure the helicity of neutrinos [9]. He found out that neutrinos are left-handed:

$$\lambda_{\nu_e} = -1.0 \pm 0.3$$

[2]SLAC - Stanford Linear Accelerator Center
[3]DONUT - Direct Observation of Nu Tau
[4]Neutrinos with a mass smaller than half the Z^0-mass $m_Z = 91.187\,\text{GeV}$
[5]LEP - Large Electron-Positron Collider
[6]CERN - Conseil Européen pour la Recherche Nucléaire - European Organization for Nuclear Research

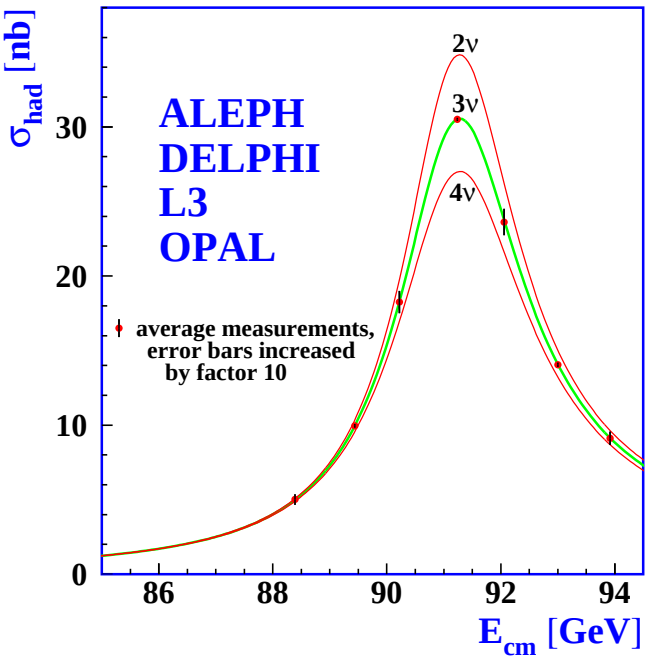

Figure 2.1: The number of light neutrinos has been obtained in all LEP experiments. The expected hadronic cross section is plotted for two, three and four neutrinos types. The experimental data agrees with three different neutrinos. Figure taken from [7].

Also, there are only right-handed antineutrinos. This can only be strictly fulfilled for massless particles. Once a particle has a non-zero mass, a left-handed particle can be transformed into a right-handed one by a Lorentz boost. The V-A theory handles this *problem* elegantly by introducing chiral operators which project the Dirac spinors for a particle to its left- and right-handed components.

Parity

A transformation which changes the signs of all spatial coordinates is called parity transformation: $\hat{P}\psi(\mathbf{x},t) = P\psi(-\mathbf{x},t)$. It has the eigenvalues $P = \pm 1$. Naïvely thinking, one would expect scalars to have a parity $P = 1$ and vectors to have $P = -1$, but there are also pseudo-scalars ($P = -1$) and axial vectors ($P = 1$). A parity transformation on a left-handed neutrino gives a right-handed neutrino[7] which is not observed in nature. Thus parity is not conserved. Parity violation was first shown in an experiment by Chien-Shiung Wu by observing the β^--decay of ^{60}Co. At a temperature of $T = 10\,\mathrm{mK}$ the spins of the ^{60}Co could be aligned in a magnetic field. The number of electrons emitted into the z direction was compared for parallel and anti-parallel spin alignment. Wu discovered, that almost only electrons with a spin anti-parallel to the z-direction were detected.

Charge conjugation

A transformation which changes a particle to its antiparticle is called charge conjugation transformation: $\hat{C}|f\rangle = |\bar{f}\rangle$. Charge conjugation of a left-handed neutrino gives a left-handed antineutrino which does not occur in nature. Hence, C-symmetry is maximally violated.

[7] Assuming massless neutrinos

CP violation

Applying both C and P transformations on a neutrino, a left-handed neutrino becomes a right-handed antineutrino and vice versa. It was assumed that CP invariance holds, but in 1964 CP violation was discovered examining the decay of neutral K-mesons [10]. It has also been observed with B mesons recently. In 1977 Cabibbo suggested that CP violation might also occur in neutrino oscillations [11]. As will be explained in Section 2.3.1, neutrino types mix similar to quarks. For three weak neutrino eigenstates, a 3×3 unitary mixing matrix is required leaving 9 real and 9 imaginary parameters. Most parameters are not linear independent leaving three real angles and one imaginary phase[8]. The imaginary CP violating phase could not yet be experimentally determined. Including time reversal T, the theory of CPT-symmetry is now established, to be an exact symmetry.

2.3 Neutrino Oscillations

Neutrino oscillations were originally proposed in terms of $\nu \leftrightarrow \bar{\nu}$ oscillations by Bruno Pontecorvo in 1957 [12]. In 1962, Maki suggested a mixing matrix for neutrino flavor transitions [13]. In case of neutrinos having mass, their weak and mass eigenstates do not necessarily have to be the same. A similar mechanism had been established for quarks by Cabibbo and was later extended by Kobayashi and Maskawa. Neutrino oscillations could then violate individual lepton numbers, while the total lepton number is still conserved. In 1969, Pontecorvo and Vladimir Gribow presented an oscillation model in terms of weak and mass eigenstates [14], which is still considered to be the right description for neutrino oscillations.

2.3.1 Neutrino Mixing

Neutrinos with a non-vanishing mass can have mass eigenstates $|\nu_i\rangle$ different from their weak eigenstates $|\nu_\alpha\rangle$. In weak interactions, the $W^\pm$- and Z^0-bosons would then couple to $|\nu_i\rangle$ instead of $|\nu_\alpha\rangle$. Each flavor can then be expressed as a superposition of mass eigenstates and vice versa.

$$|\nu_\alpha\rangle = \sum_i U^*_{\alpha i}|\nu_i\rangle, \quad |\nu_i\rangle = \sum_\alpha U_{i\alpha}|\nu_\alpha\rangle$$

with a unitary leptonic mixing matrix U. The matrix has been named after Pontecorvo, Maki, Nakagawa and Sakata and is therefore often called U_{PMNS}.

2.3.2 Neutrino Oscillations

Going to the rest frame of a neutrino ν_i with mass m_i and hence energy $E_i = m_i$ and proper time τ, it has to obey Schrödinger's equation:

$$i\partial_\tau|\nu_i(\tau)\rangle = m_i|\nu_i(\tau)\rangle$$

[8] As will be mentioned later, two more imaginary phases are required for Majorana type neutrinos.

which is solved by

$$|\nu_i(\tau)\rangle = |\nu_i(0)\rangle \cdot \exp(-im_i\tau).$$

Transforming this back to the laboratory frame with time t, the phase $m_i\tau$ can be expressed using Lorentz invariance as

$$m_i\tau = E_i t - \boldsymbol{p}_i \boldsymbol{L}$$

With the momentum $\boldsymbol{p}_i$ and the position $\boldsymbol{L}$. Using the energy-momentum relationship for relativistic particles ($m^2 \ll E^2$)

$$p_i \equiv |\boldsymbol{p}_i| = \sqrt{E_i^2 - m_i^2} \simeq E - \frac{m_i^2}{2E}$$

leads to

$$|\nu_i(\tau)\rangle = |\nu_i(0)\rangle \cdot \exp\left(-i\left(E(t-L) + \frac{m_i^2}{2E}L\right)\right)$$

for $\boldsymbol{p}_i \parallel \boldsymbol{L}$. The phase $E(t-L)$ is common to all interfering mass eigenstates and can hence be neglected. The probability for a transition from $|\nu_\alpha\rangle$ to $|\nu_\beta\rangle$ is therefore given by

$$P_{\nu_\alpha \to \nu_\beta} = \left| \left\langle \nu_\beta \left| e^{-i\frac{m_i^2}{2E}L} \right| \nu_\alpha \right\rangle \right|^2$$

which leads to

$$\begin{aligned} P_{\nu_\alpha \to \nu_\beta} = \delta_{\alpha\beta} &- 4\sum_{i>j} \mathrm{Re}(U_{\alpha i}^* U_{\beta i} U_{\alpha j} U_{\beta j}^*) \sin^2\left(\Delta m_{ij}^2 \frac{L}{4E}\right) \\ &+ 2\sum_{i>j} \mathrm{Im}(U_{\alpha i}^* U_{\beta i} U_{\alpha j} U_{\beta j}^*) \sin\left(\Delta m_{ij}^2 \frac{L}{2E}\right) \end{aligned} \tag{2.1}$$

where $\Delta m_{ij}^2 = m_i^2 - m_j^2$. The dependence on the sine motivates the expression "neutrino oscillation". For antineutrinos the sign of the last term changes [9].

The mixing matrix U can be parametrized as follows:

$$\begin{aligned} U = &\begin{pmatrix} 1 & 0 & 0 \\ 0 & \cos\theta_{23} & \sin\theta_{23} \\ 0 & -\sin\theta_{23} & \cos\theta_{23} \end{pmatrix} \times \begin{pmatrix} \cos\theta_{13} & 0 & \sin\theta_{13}e^{-i\delta} \\ 0 & 1 & 0 \\ -\sin\theta_{13}e^{i\delta} & 0 & \cos\theta_{13} \end{pmatrix} \\ &\times \begin{pmatrix} \cos\theta_{12} & \sin\theta_{12} & 0 \\ -\sin\theta_{12} & \cos\theta_{12} & 0 \\ 0 & 0 & 1 \end{pmatrix} \times \begin{pmatrix} e^{i\alpha_1/2} & 0 & 0 \\ 0 & e^{i\alpha_2/2} & 0 \\ 0 & 0 & 1 \end{pmatrix} \end{aligned}$$

consisting of four factors. θ_{ij} are three leptonic mixing angles. The last matrix contains two CP violating phases $\alpha_{1,2}$ for Majorana neutrinos and thus only having an effect if neutrinos are their own antiparticles which will be discussed shortly in Section 2.5.3. The other three factors each describe the mixing of two neutrino types, where θ_{23} can be

[9] This can be easily shown: CPT invariance requires $P_{\bar{\nu}_\alpha \to \bar{\nu}_\beta} = P_{\nu_\beta \to \nu_\alpha}$ and by changing $P_{\nu_\beta \to \nu_\alpha}$ to $P_{\nu_\alpha \to \nu_\beta}$ one has to change each matrix U in Equation 2.1 to its adjoint matrix U^* hence ending up with a change of sign in the imaginary part.

associated with the atmospheric[10] mixing angle θ_{atm} being mainly responsible for $\nu_\mu \rightarrow \nu_\tau$-oscillations. θ_{12} dominates the mixing of solar neutrinos[11] and is also called θ_{sol}. The remaining factor, called cross-mixing matrix, contains a CP violating phase δ which would lead to a difference between $P_{\nu_\alpha \rightarrow \nu_\beta}$ and $P_{\bar{\nu}_\alpha \rightarrow \bar{\nu}_\beta}$. Such a phase is only effective when all three mixing angles are non-zero and could also be rotated to any of the other matrices. As will be described later, both θ_{atm} and θ_{sol} have been found to be relatively large while the cross-mixing angle θ_{13} seems to be rather small, so including δ here emphasizes that CP violation vanishes for neutrino oscillations if θ_{13} vanishes.

2.3.3 Oscillations for two Neutrino Flavors

A simple look at neutrino oscillations is provided by assuming that only two neutrino flavors ν_e and ν_μ with mass eigenstates $\nu_{1,2}$ are relevant. This is the case when the squared-mass splittings are of different orders of magnitude. The weak eigenstates can then be connected to the mass eigenstates by a mixing matrix in the following way:

$$\begin{pmatrix} |\nu_e\rangle \\ |\nu_\mu\rangle \end{pmatrix} = \begin{pmatrix} \cos\theta & \sin\theta \\ -\sin\theta & \cos\theta \end{pmatrix} \begin{pmatrix} |\nu_1\rangle \\ |\nu_2\rangle \end{pmatrix} \tag{2.2}$$

Equation 2.1 then simplifies to:

$$P_{\nu_e \rightarrow \nu_e} = 1 - \sin^2(2\theta) \sin^2\left(\frac{1.27 \Delta m^2 L}{E_\nu}\right) \tag{2.3}$$

where Δm^2 is the difference of the squared masses of the different neutrino types in eV^2, $E_\nu \approx p$ its energy in GeV and L the distance in km.

2.3.4 Oscillations in Matter - MSW Effect

When neutrinos travel through matter, their coherent forward scattering from particles they encounter along the way can significantly modify their propagation [8]. Therefore neutrinos have a different effective mass when traversing through matter than in vacuum. Depending on the squared-mass splittings, oscillation probabilities thus may be different for neutrinos traveling through matter. This effect is called the Mikheyev-Smirnov-Wolfenstein (MSW) effect [15]. While electron type neutrinos can interact with the electrons in matter through both CC and NC reactions, muon and tau neutrinos only interact through neutral current reactions. Due to lepton universality this coupling is equal for all three neutrino types and the effects cancel out each other. So only oscillations including ν_e should be affected. Experiments indicate that the behavior of solar neutrinos is indeed influenced by a Large-Mixing-Angle (LMA) MSW effect.

[10] For a detailed description of atmospheric neutrinos see Section 2.4.2.

[11] Solar neutrinos are neutrinos produced in the sun. A more precise description can be found in Section 2.4.1.

2.4 Experimental Evidence for Neutrino Flavor Change and Oscillations

2.4.1 The Solar Neutrino Puzzle

The **S**tandard **S**olar **M**odel (SSM) describes the physical processes of our sun. The sun consists mainly of hydrogen being held together by gravitation. Towards the core of the sun, pressure and temperature get high enough to allow for thermonuclear processes. These include mainly fusion of four protons to one helium atom. The two main cycles for this process are the proton proton (pp) chain and the CNO (carbon - nitrogen - oxygen) cycle:

pp-chain:

$$\begin{aligned} p + p &\rightarrow d + e^+ + \nu_e \\ d + p &\rightarrow {}^3\mathrm{He} + \gamma \end{aligned}$$

Here the pp-chain splits up into four branches, mainly depending on the temperature.

pp I:

$${}^3\mathrm{He} + {}^3\mathrm{He} \rightarrow {}^4\mathrm{He} + p + p$$

pp II:

$$\begin{aligned} {}^3\mathrm{He} + {}^4\mathrm{He} &\rightarrow {}^7\mathrm{Be} + \gamma \\ {}^7\mathrm{Be} + e^- &\rightarrow {}^7\mathrm{Li} + \nu_e \\ {}^7\mathrm{Li} + p &\rightarrow {}^4\mathrm{He} + {}^4\mathrm{He} \end{aligned}$$

pp III:

$$\begin{aligned} {}^3\mathrm{He} + {}^4\mathrm{He} &\rightarrow {}^7\mathrm{Be} + \gamma \\ {}^7\mathrm{Be} + {}^1\mathrm{H} &\rightarrow {}^8\mathrm{B} + \gamma \\ {}^8\mathrm{B} &\rightarrow {}^8\mathrm{Be} + e^+ + \nu_e \\ {}^8\mathrm{Be} &\leftrightarrow {}^4\mathrm{He} + {}^4\mathrm{He} \end{aligned}$$

pp IV / HEP:

$${}^3\mathrm{He} + {}^1\mathrm{H} \rightarrow {}^4\mathrm{He} + \nu_e + e^+$$

CNO-cycle:

$$\begin{aligned} {}^{12}\mathrm{C} + {}^1\mathrm{H} &\rightarrow {}^{13}\mathrm{N} + \gamma \\ {}^{13}\mathrm{N} &\rightarrow {}^{13}\mathrm{C} + e^+ + \nu_e \\ {}^{13}\mathrm{C} + {}^1\mathrm{H} &\rightarrow {}^{14}\mathrm{N} + \gamma \\ {}^{14}\mathrm{N} + {}^1\mathrm{H} &\rightarrow {}^{15}\mathrm{O} + \gamma \\ {}^{15}\mathrm{O} &\rightarrow {}^{15}\mathrm{N} + e^+ + \nu_e \\ {}^{15}\mathrm{N} + {}^1\mathrm{H} &\rightarrow {}^{12}\mathrm{C} + {}^4\mathrm{He} \end{aligned}$$

In 0.04% of the time, a ${}^{16}\mathrm{O} + \gamma$ instead of the ${}^{12}\mathrm{C} + {}^4\mathrm{He}$ is produced in the last step. This minor branch is known as the CNO II cycle whereas the main branch is called CNO I

Name	Reaction	Flux [$\mathrm{cm^{-2}s^{-1}}$]	$E_{\nu,\max}$ [MeV]
pp	$p + p \rightarrow d + e^+ + \nu_e$	5.99×10^{10}	0.422
pep	$p + e^- + p \rightarrow d + \nu_e$	1.42×10^{8}	1.442
hep	$^3\mathrm{He} + p \rightarrow {}^4\mathrm{He} + e^+ + \nu_e$	7.93×10^{3}	18.8
^{7}Be	$^7\mathrm{Be} + e^- \rightarrow {}^7\mathrm{Li} + \nu_e$	4.84×10^{9}	0.861/0.384
^{8}B	$^8\mathrm{B} \rightarrow {}^8\mathrm{Be} + e^+ + \nu_e$	5.69×10^{6}	16.34
^{13}N	$^{13}\mathrm{N} \rightarrow {}^{13}\mathrm{C} + e^+ + \nu_e$	3.07×10^{8}	1.199
^{15}O	$^{15}\mathrm{O} \rightarrow {}^{15}\mathrm{N} + e^+ + \nu_e$	2.33×10^{8}	1.732

Table 2.2: Neutrino fluxes and energies predicted by the BS05(OP) SSM [20].

cycle [16]. The pp cycle is the dominating process in our sun. The standard solar model predicts 1.5% of the solar luminosity to be generated by the CNO cycle. Solar neutrino experiments set an upper limit of 7.3% to the fraction of energy that the sun produces via the CNO fusion cylcle [17].

For the pp-chain and the CNO I cycle, the net process is $4p \rightarrow {}^4\mathrm{He} + 2e^+ + 2\nu_e + 26.73\,\mathrm{MeV}$. About one third of the released energy is carried off by the neutrinos. Flux and energy for neutrinos originating from the different processes are shown in Figure 2.2. Neutrinos from the *pp* reaction[12] have the highest abundance, but are with an energy $< 422\,\mathrm{keV}$ hard to detect.

Neutrinos are the only particles being produced in the center of the sun that have the ability to penetrate to the surface and escape into space. Studying the properties of solar neutrinos thus makes it possible to study the processes in the core of our sun. In 1964 Bahcall and Davies suggested an experiment to test whether converting hydrogen nuclei to helium nuclei in the sun is indeed the process releasing its energy. The experiment was realized and is known under the name Homestake.

Homestake

The Homestake chlorine experiment started in 1968 under the supervision of Raymond Davies, Jr. at the Homestake gold mine in Lead, South Dakota. It was the first experiment to attempt the observation of solar neutrinos. The detector consisted of a tank containing 390 000 liters of liquid tetrachlorethylene (C_2Cl_4) located 1480 meters (4400 m.w.e.[13]) below the surface of the earth. With a threshold energy of 814 keV, chlorine detectors are mainly sensitive to neutrinos originating from ^{8}B reactions, but also to some extent to ^{7}Be, *pep*, ^{13}N and ^{15}O processes. Neutrino detection was done via the caption of the neutrino in the process $^{37}\mathrm{Cl} + \nu_e \rightarrow {}^{37}\mathrm{Ar} + e^-$, hence only electron type neutrinos could be detected. To determine the neutrino flux, the ^{37}Ar was removed from a large volume of liquid by flushing the tank with helium and its decay was observed in a small proportional counter [18]. First results did not show any significant excess of events above background, but after an improvement in the detector's electronics, a finite solar neutrino flux had been observed. The combined results of 108 runs between 1970 and 1994 lead to a flux of $2.56 \pm 0.16 \pm 0.16$ SNU[14] [19] which is about $\frac{1}{3}$ of the current

[12] see Table 2.2

[13] m.w.e. - meters water equivalent

[14] SNU - Solar Neutrino Unit is defined as 10^{-36} neutrino captions per atom per second.

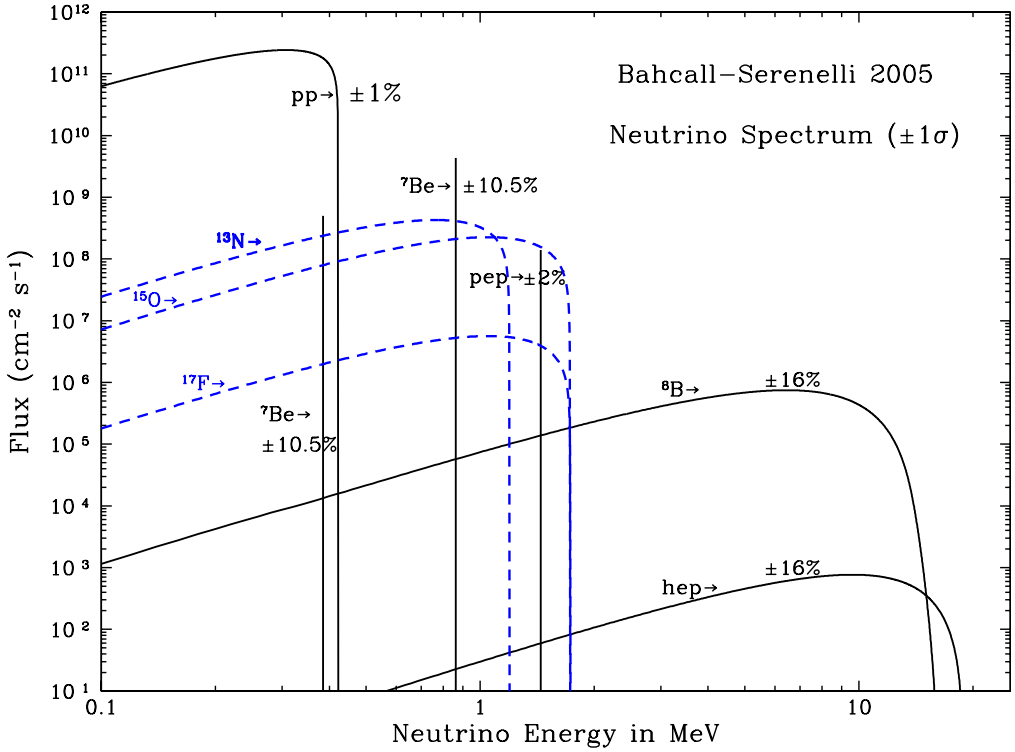

Figure 2.2: Neutrino flux at Earth predicted by the Standard Solar Model of 2005. Solid lines: neutrinos produced in the pp-chain, dashed lines: neutrinos produced in the CNO cycle. Figure taken from [20].

value of 8.1 ± 1.3 SNU predicted by the SSM (BS05(OP) [20]).

The discrepancy between the solar model and the experimental results was named the solar neutrino problem and had not been solved for another thirty years. The assumption of neutrino mixing could explain for the *missing* neutrinos to be, in fact, not missing but just being changed into one of the other flavors.

GALLEX, SAGE and GNO

Other radiochemical attempts to measure the solar neutrino flux were GALLEX[15] at Gran Sasso in Italy and SAGE[16] at Baksan in Russia. Instead of using chlorine for the neutrino capture, gallium was used reducing the threshold energy to 233 keV thus being also sensitive to lower energy neutrinos including neutrinos from *pp*-reactions. The reaction used is:

$$^{71}\mathrm{Ga} + \nu_e \rightarrow {}^{71}\mathrm{Ge} + e^-.$$

GALLEX presented the first evidence of *pp* solar-neutrino observation in 1992 [21] reporting a very low capture rate. SAGE observed a similar capture rate [22]. Both groups tested their detector setups with *man-made* neutrinos from ^{51}Cr successfully, demonstrating the reliability of these experiments. After GALLEX finished observations in 1997, a

[15]GALLEX - GAllium EXperiment
[16]SAGE - Soviet American Gallium Experiment

new collaboration was build called GNO (Gallium Neutrino Observatory) which continued the observations from 1998 to 2003. A joint analysis leads to: $69.3 \pm 4.1 \pm 3.6$ SNU [23], which is about half of the expected value of about 120 SNU [20].

Kamiokande and Super-Kamiokande

A second approach to detect solar neutrinos was the Kamiokande[17] experiment running from 1987 up to 1995. Located in the Kamioka mine in the Gifu Prefecture in Japan at a depth of 1000m (2700 m.w.e.) an ultra-pure water Čerenkov detector containing 2142 metric tons of water was built. The electron involved in the scattering process

$$\nu_x + e^- \rightarrow \nu_x + e^-$$

emits Čerenkov light which can be detected by a system of about 1000 photo multiplier tubes (PMTs). Čerenkov radiation is emitted when a charged particle travels through a medium at a speed greater than the speed of light in that medium. The direction of the emitted photons depends on the velocity $\beta = \frac{v}{c}$ of the particle as well as the refractive index n: $\cos\theta = \frac{1}{n\beta}$. The direction between the incoming neutrino and the recoil electron is related, thus a good separation between events from solar neutrinos and background could be achieved. For the first time a spatial correlation between the observed neutrino and the sun was observed. The neutrino flux was obtained from data with $E_e \geq 9.3\,\mathrm{MeV}$ and therefore only neutrinos from ^{8}B-reactions were detected [24].

While electron neutrinos scatter through both the interchange of Z and W bosons with electrons in matter, muon- and tau neutrinos can only participate in neutral current interactions. Hence elastic scattering is sensitive to all active neutrino types, however it is suppressed for μ- and τ-neutrinos, having a sensitivity of only $\sigma(\nu_{\mu,\tau}) \approx 0.16 \cdot \sigma(\nu_e)$. Because of the strong directional correlation, Kamiokande gave the first direct evidence that the sun emits neutrinos, but also measured a flux smaller than the one predicted by the SSM. Both low energy and high energy neutrinos were missing, although not in the same proportions. For the ^{8}B-neutrinos, a flux of $2.80 \pm 0.19 \pm 0.33 \times 10^6\,\mathrm{cm^{-2}s^{-1}}$ was observed [25], about half of the one expected.

Kamiokande's successor, Super-Kamiokande is a 50 kilotons water Čerenkov detector designed to study solar and atmospheric neutrinos which started observation in 1996. With the new detector, a much higher counting rate could be achieved and the threshold could be lowered to 5 MeV. In November 2001 an accident occurred at Super-Kamiokande and a substantial number of the 11146 photo multipliers was destroyed. It was rebuilt within a year with about half the number of PMTs. The experiment before the accident is called Super-Kamiokande I, after the accident it is called Super-Kamiokande II. The ^{8}B flux measured from ν-e scattering is similar to the one observed by Kamiokande, namely $2.35 \pm 0.02 \pm 0.08 \times 10^6\,\mathrm{cm^{-2}s^{-1}}$ [26]. Kamiokande and Super-Kamiokande were also used for the observation of atmospheric neutrinos which will be discussed in Section 2.4.2.

Evidence for flavor change of solar neutrinos

Convincing evidence for neutrino flavor change was given by the Sudbury Neutrino Observatory (SNO). Located 2092 m (6010 m.w.e.) underground in INCO Limited's Creighton

[17] Kamioka Nucleon Decay Experiment

nickel mine, near Sudbury, Ontario in Canada a large acrylic vessel filled with 1 kton of highly pure heavy water is used as a Čerenkov detector. The heavy water is on loan from Atomic Energy of Canada Limited (AECL). The vessel is surrounded by 9456 inward-looking and 91 outward-looking highly sensitive photo multiplier tubes. Neutrino interactions in the D_2O result in the generation of Čerenkov light and the photons thus produced can be detected by the photo multiplier tubes. The following processes can occur, when a solar neutrino from a ^{8}B-decay passes the detector:

$$\begin{array}{ll} \nu_e + d \rightarrow p + p + e^- & \text{charged current} \\ \nu_x + d \rightarrow \nu_x + p + n & \text{neutral current} \\ \nu_x + e^- \rightarrow \nu_x + e^- & \text{elastic scattering.} \end{array}$$

Elastic scattering (ES) is sensitive to all neutrino flavors, though the electron neutrino reaction is preferred by a factor of approximately 6.5 compared to muon and tau neutrinos. While the CC reaction is only sensitive to electron neutrinos, the NC reaction is equally sensitive to all active neutrino flavors. It is hence possible to simultaneously measure the solar ν_e flux and the total flux of all active neutrinos species. The contributions from the CC reaction and the elastic scattering can be distinguished by using different $\cos\theta$ distributions, where θ is the angle of the electron momentum with respect to the direction from the sun to the earth. ES produces electrons with a strong forward peak while CC events have an angular distribution which can be described by $1-\frac{1}{3}\cos\theta$ [8]. The electron produced in ES and CC reactions can be observed through the Čerenkov light emitted by the electron. The NC reaction is detected through a more complicated process, the produced neutron is captured by a deuterium from the D_2O creating an excited state then emitting a photon of 6.25 MeV. This γ Compton-scatters in the detector, the electrons involved then emit observable Čerenkov light.

The SNO experiment was designed to be carried out in three distinct phases corresponding to three ways of detecting neutrinos. The first phase, also called the D_2O-phase, already demonstrated that the total active neutrino flux from the sun, observed via neutral current (NC) reactions, is consistent with the Standard Solar Model, whereas solar neutrinos being detected via the CC reaction on the deuterium and the elastic scattering of electrons yields only about $\frac{1}{3}$ of the expected value. The measured ν_e-flux differs from the Super-Kamiokande ES results by $3.3\,\sigma$.

For the second phase or salt phase of SNO, experimenters dissolved 2 tons of ultra pure salt (NaCl) into the heavy water to increase the separability of the CC and NC reactions. Also the detection efficiency of the NC reactions is increased. The neutron produced in NC reactions can now be captured by the chlorine having a significantly higher cross-section than deuterium. Also, instead of just one photon multiple γ's are emitted with a total energy of 8.6 MeV thus producing more Čerenkov light. The following ^{8}B solar neutrino fluxes were measured:

$$\begin{aligned} \phi_{\mathrm{CC}} &= 1.68^{+0.06+0.08}_{-0.06-0.09} \times 10^6\,\mathrm{cm}^{-2}\mathrm{s}^{-1} \\ \phi_{\mathrm{NC}} &= 4.94^{+0.21+0.38}_{-0.21-0.34} \times 10^6\,\mathrm{cm}^{-2}\mathrm{s}^{-1} \\ \phi_{\mathrm{ES}} &= 2.35^{+0.22+0.15}_{-0.22-0.15} \times 10^6\,\mathrm{cm}^{-2}\mathrm{s}^{-1}. \end{aligned}$$

The fluxes are shown in Figure 2.3 [27]. Data from SNO, Super-Kamiokande and other experiments were combined in global fits giving the following constraints for oscillation

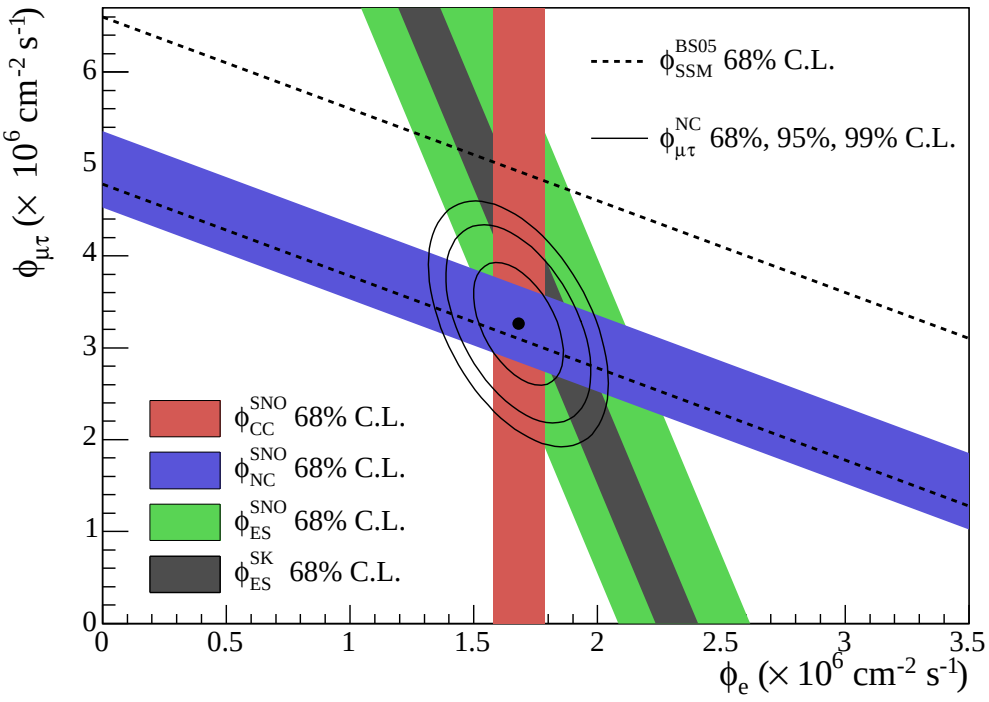

Figure 2.3: Fluxes of ^{8}B solar neutrinos deducted from SNO's salt phase measurements. The flux of electron neutrinos is plotted versus the flux of μ and τ neutrinos. The narrow band for the elastic scattering is taken from Super-Kamiokande results [27].

parameters shown also in Figure 2.6:

$$\Delta m^2_{12} = 8^{+0.6}_{-0.4} \times 10^{-5}\,\mathrm{eV}^2$$
$$\tan^2\theta_{12} = 0.45^{+0.09}_{-0.07}.$$

The third phase called helium phase has just been finished. To improve NC flux measurement further, forty ^{3}He proportional counters had been installed as neutral current detectors (NCDs) in the heavy water. The neutron could then be captured by the Helium producing a proton and tritium thus providing a distinct NC event measurement.

2.4.2 Atmospheric Neutrinos

Atmospheric neutrinos are produced from the decays of particles in hadronic showers resulting from interactions of cosmic rays with the Earth's atmosphere. In those interactions, mainly pions and kaons are produced of which a large fraction then decay as follows:

$$K^0 \to \pi^+\pi^- \qquad \pi^0 \to 2\gamma$$
$$K^0 \to \pi^0\pi^0 \qquad \pi^+ \to \mu^+\nu_\mu$$
$$K^+ \to \mu^+\nu_\mu \qquad \pi^- \to \mu^-\bar{\nu}_\mu$$
$$K^- \to \mu^-\bar{\nu}_\mu$$

hence always ending up with either photons or a μ-ν_μ pair. The muon itself will decay further into an electron, its corresponding neutrino and another muon neutrino. Therefore one would expect an electron type / muon type neutrino ratio of about

$$\frac{N(\nu_e + \bar{\nu}_e)}{N(\nu_\mu + \bar{\nu}_\mu)} \simeq \frac{1}{2}.$$

Neutrinos originating from the Earth's atmosphere have much higher energies than solar neutrinos ranging from about 100 MeV up to 10 TeV. Therefore, both atmospheric muon and electron neutrinos can be detected with the Super-Kamiokande Čerenkov detector via charged current interactions $\nu_x + N \to l_x + X$.

An electron from a neutrino reaction will shower in the detector whereas a muon will travel straight on. This leads to a distinct pattern of the Čerenkov light providing information on the flavor of the incoming neutrino. Also, the direction of the light cone is related to that of the incoming neutrino, so that its direction can be determined.

Since neutrinos pass the Earth almost unaffected, the flux of atmospheric neutrinos should be independent of the zenith angle in the case of no oscillations. Comparing the flux of upward- and downward-going neutrinos can therefore give evidence for neutrino oscillations. A neutrino being produced on the other side of the Earth has traveled an approximately 12756 km longer distance than one produced in the atmosphere above a detector.

First evidence of atmospheric neutrino oscillation was given by the Super-Kamiokande experiment in 1998. Their data shows evidence for two flavor $\nu_\mu \to \nu_\tau$ oscillations with $\sin^2 2\theta_{\text{atm}} > 0.82$ and $5 \times 10^{-4} < \Delta m^2 < 6 \times 10^{-3}\text{eV}^2$ at 90% confidence level. Figure 2.4 shows the angular distributions measured by Super-Kamiokande. While the ν_e-rate is as expected, the ν_μ-rate is significantly decreasing for the upward direction. The non-observation of atmospheric ν_e appearance points to $\nu_\mu \to \nu_\tau$ mixing as the dominant oscillation mode [30].

Super-Kamiokande I has observed more than 15000 atmospheric neutrino events within an energy range from about 100 MeV to 10 TeV and with a neutrino flight length from about 10 km to 13000 km. The up-down asymmetry of the atmospheric neutrino flux leads to a best fit value for $\sin^2\theta_{\text{atm}} > 0.92$ and $1.5 \times 10^{-3} < \Delta m^2 < 3.4 \times 10^{-3}\,\text{eV}^2$ [31]. The allowed region for the oscillation parameters is shown in Figure 2.5.

From Equation 2.3 follows, that $P_{\nu_\mu \to \nu_\mu}$ should be minimal for $1.27\Delta m^2_{\text{atm}} \frac{L}{E} = \frac{\pi}{2}$. For a Δm^2 as found by Super-Kamiokande this should occur when $\frac{L}{E} \approx 500\,\frac{\text{km}}{\text{GeV}}$ which is consistent with the data.

A search for the appearance of tau neutrinos from $\nu_\mu \leftrightarrow \nu_\tau$ oscillations for atmospheric neutrinos has also been performed. In 1489.2 days of atmospheric data taking, $138 \pm 48^{+15}_{-32}$ τ events of upward going tau leptons have been observed exceeding the expected value of 78 ± 26. This analysis disfavors the hypothesis of no ν_τ appearance by

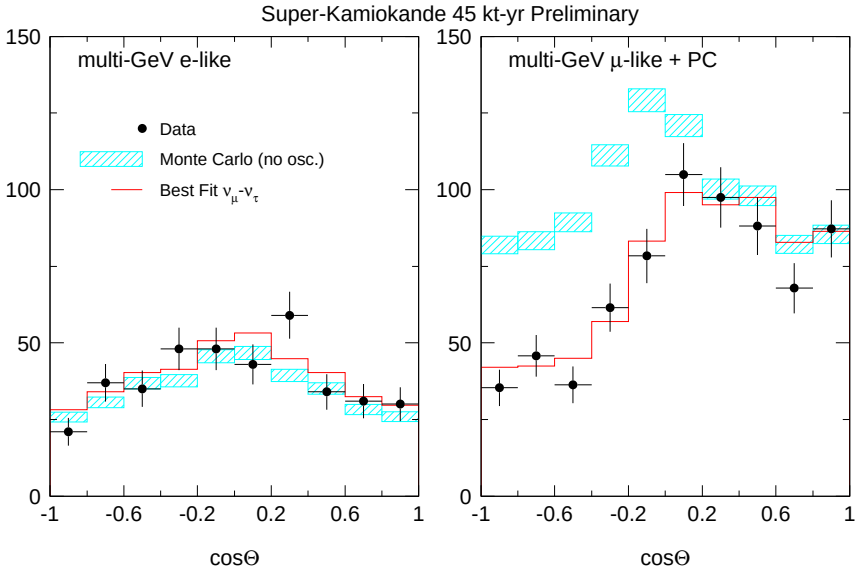

Figure 2.4: Angular distributions for e-like and μ-like events at the Super-Kamiokande detector recorded by December 1998 [29].

$2.6\,\sigma$ and is consistent with a $\Delta m^2 = 2.4 \times 10^{-3}\,\mathrm{eV}^2$ for full mixing in $\nu_\tau \leftrightarrow \nu_\mu$ oscillations [32]. In contrast to this, the goal of the OPERA experiment is to demonstrate the ν_τ appearance with higher significance.

MACRO

The MACRO[18] experiment at Gran Sasso also investigated oscillations of atmospheric neutrinos using liquid scintillator counters for time measurement and streamer tubes for tracking allowing an angular resolution ranging from 0.2° to 1°. The experiment could verify the Super-Kamiokande data achieving best fit values of $\sin^2\theta = 1$ and $\Delta m^2 = 2.3 \times 10^{-3}\,\mathrm{eV}^2$ [33].

SOUDAN2

Another experiment measuring up- and downward stopping muons initiated by atmospheric neutrinos was SOUDAN2 at the Soudan Mine in Minnesota. Here a 963 ton iron tracking calorimeter was used, operating at a depth of 2070 m.w.e. to reduce background. The tracking was done with hytrel plastic drift tubes. The experiment could also confirm ν_μ disappearance from upward going neutrinos, a best fit of $\Delta m^2 = 1.77 \times 10^{-3}\,\mathrm{eV}^2$ and $\sin^2\theta = 0.97$ is presented in [34].

2.4.3 Reactor neutrinos

There are several neutrino sources on earth. Neutrinos ($\bar{\nu}_e$) are involved in nuclear fission and therefore plentiful produced in nuclear reactors. Since reactions in nuclear plants are

[18]MACRO - Monopole Astrophysics and Cosmic Ray Observatory

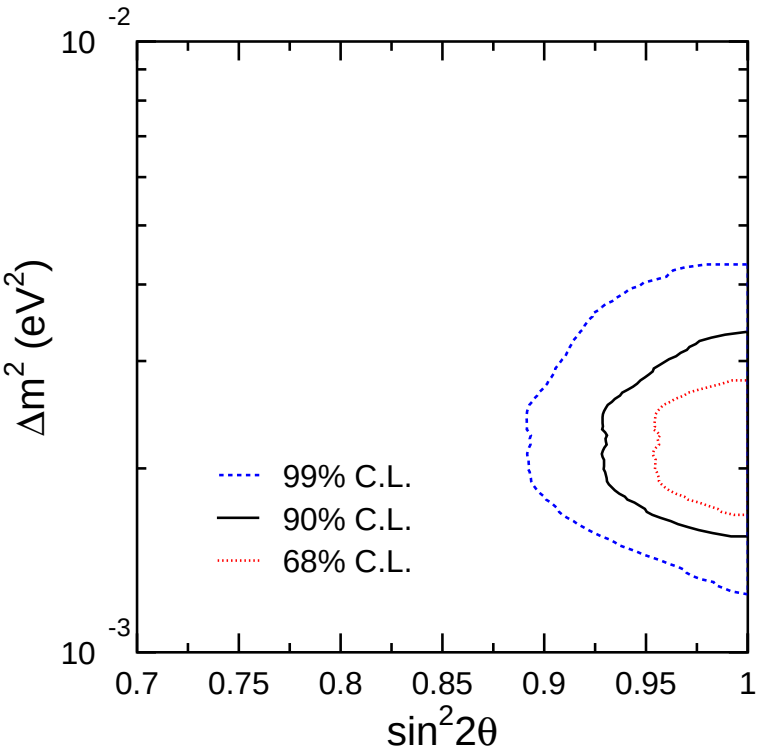

Figure 2.5: Allowed oscillation parameters for $\nu_\mu \leftrightarrow \nu_\tau$ oscillations measured at the Super-Kamiokande experiment [31].

precisely monitored, the neutrino flux from reactors can be well predicted. It is directly related to the thermal power P of a reactor:

$$\phi_\nu = 1.5 \times 10^{12} \frac{P\,[\mathrm{MW}]}{L^2\,[\mathrm{m}^2]}$$

with the distance L to the detector. The study of reactor $\bar{\nu}_e$ allows to test both results from solar and atmospheric neutrino experiments. There are several short and medium baseline experiments located close to nuclear reactors.

KamLAND

The KamLAND[19] experiment studies oscillations of ν_e's emitted by reactors at a distance of typically 180 km. It is located at the site of the former Kamiokande experiment. The long baseline setup enables KamLAND to test the oscillation solution of solar neutrinos. To detect the neutrinos, the inverse β-decay

$$\bar{\nu}_e + p \rightarrow e^+ + n$$

[19]KamLAND - Kamioka Liquid Scintillator Anti-Neutrino Detector

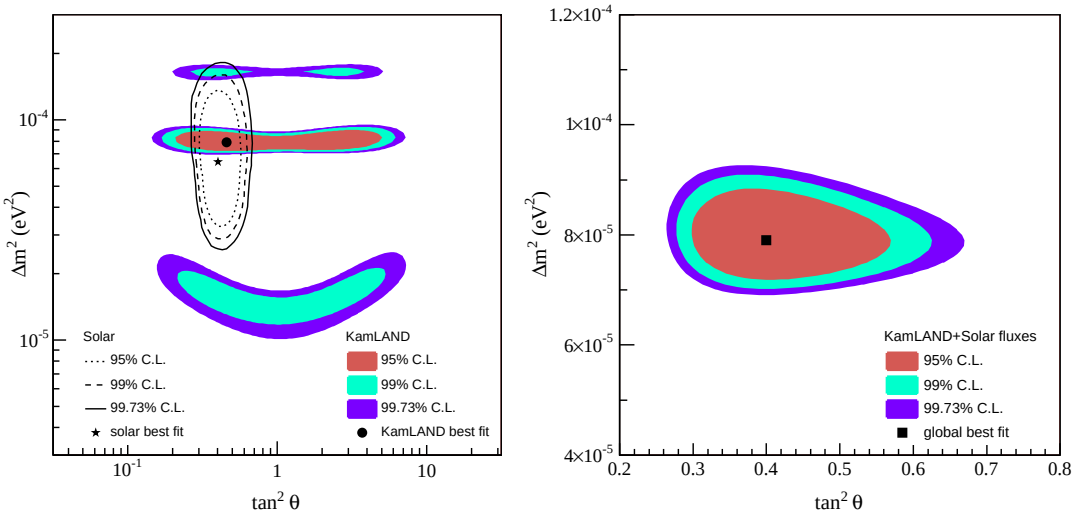

Figure 2.6: Neutrino oscillation parameter region for θ_{12} and Δm_{12}. Left: allowed regions from KamLAND (color) and global fit from SNO and Super-Kamiokande (dashed) [36]. Right: Combined results for a two-neutrino oscillation analysis.

in 1 kton of ultra-pure liquid scintillator is used. Detecting both the positron and a delayed 2.2 MeV photon from neutron capture allows to reduce background [35].

A $\bar{\nu}_e$ disappearance at long baselines could be demonstrated. KamLAND's oscillation parameters give strong evidence for a LMA solution for solar neutrinos. The KamLAND results also confirmed the observations made at SNO. A combined analysis for the solar mixing angle and Δm^2_{sol} can be found in Figure 2.6.

CHOOZ

CHOOZ was a short baseline (SBL) experiment searching for $\bar{\nu}_e$ disappearance at a distance of 1115 m / 998 m to the Chooz nuclear reactors B1 and B2 next to the Meuse River in France. Both reactors have a combined power of 8.5 GW. To detect the neutrino flux, 4.8 tons of liquid scintillator with a 0.1% admixture of Gadolinium were used. Detection is done via the inverse β-decay. A coincidence of two 0.511 MeV γs as a primary signal as well as the ~ 8 MeV γ-signal from the neutron capture of the Gd as a secondary signal gives a distinct signature for a neutrino event.

No evidence for neutrino oscillations has been found for parameter regions of $\Delta m^2 > 7 \times 10^{-4}\,\text{eV}^2$ for maximal mixing[20] or $\sin^2 2\theta = 0.10$ for a large Δm^2 [37].

Currently, the succeeding experiment Double-CHOOZ is in preparation. It will use two identical detectors, a *near* detector at ~ 150 m to the reactors in addition to the *far* detector in the old location. To improve sensitivity, an increase in statistics and a reduction of systematic errors and background is planned [38].

[20] Maximum mixing is fulfilled for $\sin^2\theta = 1$

Palo Verde

Palo Verde was another reactor experiment at the Palo Verde Generating Station near Phoenix in Arizona. The detector consisted of 12 tons of liquid scintillator with an admixture of 0.1% of Gd. Like the CHOOZ experiment, no oscillation were found [39].

These results from SBL reactor experiments lead to the conclusion that $\nu_e \leftrightarrow \nu_\mu$ are not the dominant channel for atmospheric oscillations.

2.4.4 Neutrino Beams

Another *man made* neutrino source are neutrino beams. As being described in Section 3.2, intense ν_μ beams can be produced using accelerators. This is e.g. done for the NuMI beam at Fermilab or CNGS at CERN. These ν_μ sources can be used to probe results from atmospheric neutrino experiments.

K2K

At the KEK to Kamioka long-baseline experiment, a ν_μ beam was produced using an accelerator. The ν_μ flux could be measured by a complex of near detectors as well as the Super-Kamiokande detector at a distance of 235 km. The number of observed events at Super-Kamiokande was significantly less than the number expected from the near detectors assuming no oscillations, 107 events were observed, whereas 151^{+12}_{-10} were expected for no oscillation. This leads to values of $\sin^2 2\theta = 1$ and $\Delta m^2 = 2.8 \times 10^{-3}\,\mathrm{eV}^2$ as also indicated in Figure 2.7 [40].

MINOS

MINOS[21] is a long baseline experiment looking for ν_μ-disappearance in the NuMI beam from Fermilab. The composition and energy spectrum is measured in two detectors, the 1 kton near detector 1 km from source at Fermilab National Laboratory and the 5.4 kton far detector situated 735 km away at a depth of 714 m in an underground laboratory at Soudan, Minnesota. Both consist of a sandwich structure of 2.54 cm thick steel plates and 1 cm thick plastic scintillators. Charged current ν_μ events appear as long muon tracks accompanied by short hadronic showers near the event vertex.

An important feature of the NuMI beam is the ability to vary the energy spectrum of the focused muons by adjusting the magnetic horns. This allows operation of the experiment with different neutrino spectra. For the initial run, the low energy setup is used with a medium neutrino energy of approximately $E_\nu = 3.5\,\mathrm{GeV}$. A luminosity of $3.7 \times 10^{20}\,\mathrm{pot}$ per year is planned which is higher than the foreseen $4.5 \times 10^{19}\,\mathrm{pot}$ per year for the CNGS beam. However, the threshold energy for ν_τ production is 3.4 GeV, so because of this choice, a measurement of ν_τ appearance is not possible at MINOS. The goal of the MINOS experiment is to improve the precision of Δm^2_{23} significantly.

Recently, the MINOS collaboration published first results of the first year of data taking. Preliminary analysis of this data is consistent with the oscillation scenario reported by Super-Kamiokande and K2K as shown in Figure 2.7. The best fit parameters obtained are $\Delta m^2_{23} = 3.05^{+0.60}_{-0.55} \times 10^{-3}\,\mathrm{eV}^2$ and $\sin^2\theta_{23} = 0.88^{+0.12}_{-0.15}$ [41].

[21] MINOS - Main Injector Neutrino Oscillation Search

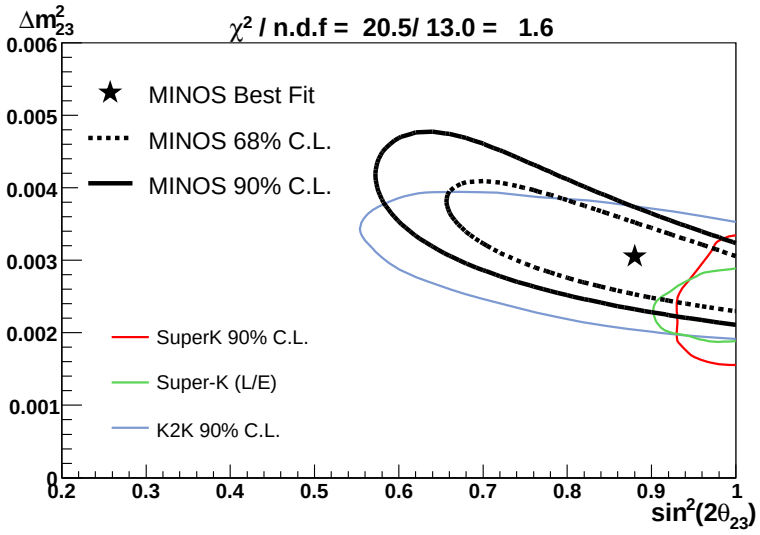

Figure 2.7: MINOS preliminary allowed region. The black solid (dashed) line shows the MINOS 90% (68%) confidence limit in Δm^2_{23} and $\sin^2 2\theta_{23}$. From [41].

2.4.5 Other Oscillation Experiments

LSND

LSND[22] was a neutrino detector at the Los Alamos National Laboratory. The experiment took place over six years finding evidence for $\bar{\nu}_e$ appearance in neutrinos of the decay of resting muons:

$$\mu^+ \rightarrow e^+ + \nu_e + \bar{\nu}_\mu.$$

and claims to have found a $\bar{\nu}_e$-rate exceeding the expected background. The best fit for $\nu_\mu \rightarrow \nu_e$-oscillations from LSND is $\sin\theta_{13} > 0.003$ and $\Delta m^2_{13} = 1.2\,\mathrm{eV}^2$ [42]. The related KARMEN[23] experiment could not confirm the observations [43].

MiniBooNE[24] is an experiment at Fermilab which is motivated by LSND's oscillation results currently trying to verify the parameters. [44]

2.5 Neutrino Masses

The experiments described above have revealed, that neutrinos do have mass. Values for two neutrino squared-mass differences as well as two out of four mixing parameters have been found. Furthermore a limit of $\sin^2\theta_{13} < 0.03$ could be derived.

Using $s_{ij} \equiv \sin\theta_{ij}$ and $c_{ij} \equiv \cos\theta_{ij}$ and omitting the possible CP violating phases for Majorana particles, U_{PMNS} can be written as follows:

$$U = \begin{pmatrix} c_{12}c_{13} & s_{12}c_{13} & s_{13}e^{-i\delta} \\ -s_{12}c_{23} - c_{12}s_{23}s_{13}e^{i\delta} & c_{12}c_{23} - s_{12}s_{23}s_{13}e^{i\delta} & s_{23}c_{13} \\ s_{12}s_{23} - c_{12}c_{23}s_{13}e^{i\delta} & -c_{12}s_{23} - s_{12}c_{23}s_{13}e^{i\delta} & c_{23}c_{13} \end{pmatrix}.$$

[22]LSND - Liquid Scintillator Neutrino Detector
[23]KARMEN - KArlsruhe Rutherford Medium Energy Neutrino
[24]BooNE - Booster Neutrino Experiment

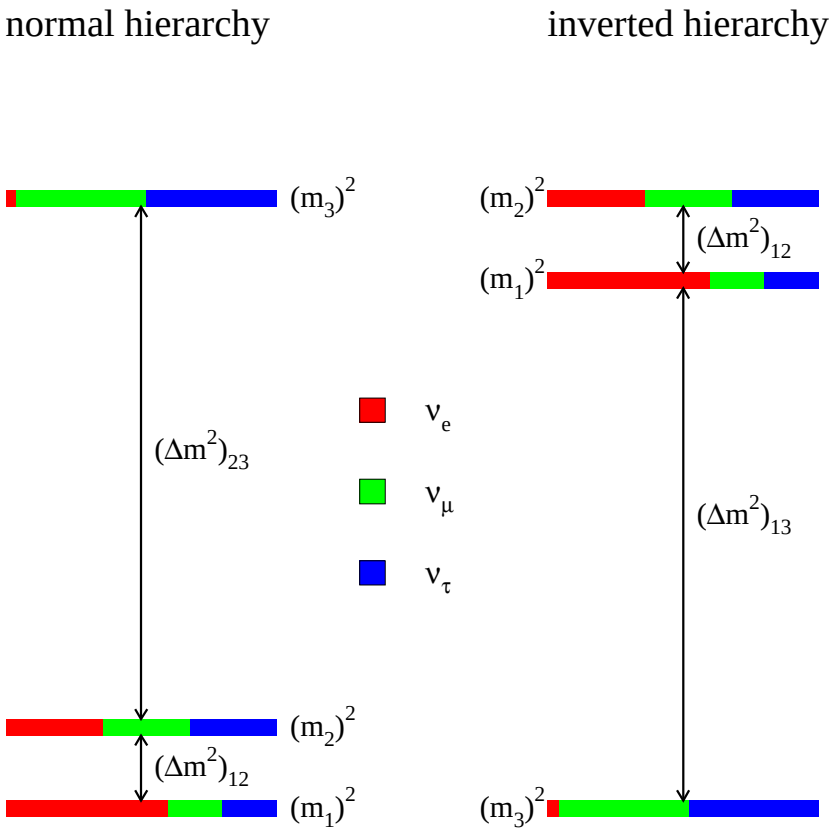

Figure 2.8: Mass hierarchies and neutrino mixing for $\sin^2\theta_{12} = 0.30$, $\sin^2\theta_{23} = 0.50$ and $\sin^2\theta_{13} \leq 0.047$.

The fraction of each distinct flavor $|\nu_\alpha\rangle$ contained in each mass eigenstate $|\nu_i\rangle$ can be easily determined by $|U_{\alpha i}|^2$. As neutrino oscillations only depend on the squared-mass splittings, measurements of oscillation probabilities do not give information on the absolute masses. Neither the mass of the lightest neutrino is known, nor the pattern in which masses of the three neutrinos are arranged. Although it has been established from solar neutrino matter effects that $m_2^2 > m_1^2$, experiments are unable to determine the sign of Δm_{13}^2 leading to two possible mass hierarchies shown in Figure 2.8. The inverted scheme is characterized by a $\Delta m_{13}^2 < 0$ whereas for normal hierarchy $m_1^2 < m_2^2 < m_3^2$.

If there are only three neutrino mass eigenstates they obviously satisfy

$$\Delta m_{32}^2 + \Delta m_{13}^2 + \Delta m_{21}^2 = 0.$$

Δm_{23}^2 and Δm_{12}^2 have been found to be of a different order of magnitude, hence Δm_{13}^2 should be of the same order as the larger Δm_{23}^2. Results from LSND indicate that this is not the case. If all measurements are correct, at least a fourth neutrino mass eigenstate must exist. This would lead to at least one more neutrino type. A fourth neutrino species could be explained by sterile neutrinos, as explained in Section 2.5.3. However, LSND results have not yet been confirmed by other experiments.

2.5.1 Mass Limits from Kinematics of Weak Decays

Kinematics of weak decays can be reconstructed by observing the charged decay products. Through measurements of the process $\pi \rightarrow \mu + \nu_\mu$ at PSI[25] [45] and the investigation of 5 prong τ-decays at LEP [46], upper limits of $m_{\nu_\mu} < 190\,\mathrm{keV}$ and $m_{\nu_\tau} < 18.2\,\mathrm{MeV}$ were found.

The beta decay of tritium provides a method of measuring absolute $|\nu_e\rangle$ mass $m_\beta(\nu_e) = \sum_i |U_{ei}|^2 \cdot m_i$. If neutrinos have mass, the maximum energy of a emitted electron must be lower than that in the case of a massless neutrino. Tritium has a half life of $t_{1/2} = 12.3\,\mathrm{y}$, the decay has an endpoint energy of $E_0 = 18.6\,\mathrm{keV}$. Various experiments have observed the β spectrum using magnetic or electrostatic spectrometers.

Mainz and Troitsk

The current best limits for the ν_e mass come from the β-decay experiments in Mainz and Troitsk. They both used integrating β-electron spectrometers providing high luminosity and low background. The Mainz experiment found an upper limit of [47]

$$m_\beta(\nu_e) < 2.3\,\mathrm{eV},$$

the Troitsk result is [48]

$$m_\beta(\nu_e) < 2.05\,\mathrm{eV}.$$

KATRIN

KATRIN[26], which is currently under construction will use a windowless gaseous tritium source allowing the measurement of the endpoint region of the tritium β decay with a minimum of systematic uncertainties from the source. The key component of the new experiment is a large electrostatic spectrometer with a diameter of 10 m and a length of 22 m which was recently delivered to the Karlsruhe experimental site. It has a foreseen energy resolution of $\Delta E < 600\,\mathrm{eV}$ for 18.6 keV electrons [48]. This will provide a sensitivity to neutrino masses down to 0.2 eV.

2.5.2 Astrophysical Methods

Relic neutrinos from the Big Bang with a density of about 112 neutrinos per flavor and cm^3 and neutrino bursts from supernovae are other sources offering methods for the determination of neutrino masses.

Cosmic microwave background radiation and large scale structure

Neutrinos left over from the Big Bang are predicted to exceed the number of left over baryons by 9 orders of magnitude. These relic neutrinos could influence the cosmos in form of *neutrino hot dark matter*. Constraints on the hot dark matter content can be set by observations of the structure in the universe at different scales and the angular

[25] PSI - Paul Scherrer Institut near Zürich
[26] KATRIN - KArlsruhe TRItium Neutrino Experiment

distributions of fluctuations of the cosmic microwave background radiation. The matter distribution in the universe can be determined by observations of the Lyman-α forest, galaxy abundances and galaxy redshift surveys.

Recent data from WMAP[27] alone indicate a limit on the sum over neutrino masses of [49]

$$\sum_i m_{\nu_i} < 2.11\,\text{eV}.$$

Combining their results with SDSS[28] or 2dFGRS[29] yields even better limits of 0.91 eV and 0.87 eV respectively.

Neutrino time-of-flight

Another technique for direct determination of neutrino masses can be achieved through time-of-flight measurements over astrophysical distances. Massive neutrinos from supernova explosions, mainly $\bar{\nu}_e$, ν_μ and ν_τ, experience a time delay compared to massless particle over a large distance which will be measurable even for tiny masses. Considering the limit on the ν_e mass from Section 2.5.1, a time delay could be measured from the arrival of $\bar{\nu}_e$ relative to the ν_μ and ν_τ events. $\bar{\nu}_e$ events can also be used to calibrate the neutrino luminosity of the supernova [50],[51].

2.5.3 Dirac versus Majorana Neutrinos - Sterile Neutrinos

Neutrinos are the only fundamental leptons with no electrical charge. Majorana suggested in 1937 that neutrinos could have mass terms in such a way that they would be their own antiparticles [52]. This leads to a violation of the conservation of lepton number. Such neutrinos are called Majorana neutrinos.

If neutrino mass eigenstates are different from their antiparticle, they are called Dirac particles. The lepton number distinguishes Dirac neutrinos from antineutrinos.

A neutrino with non-vanishing mass always travels slower than the speed of light, hence its helicity depends on the viewers reference system and can be changed by a simple Lorentz boost. Therefore, both right and left-handed neutrinos must exist in this case.

Right-handed neutrinos and left-handed antineutrinos do not participate in weak interactions and can therefore not be observed at all. These neutrinos can be described in terms of singlets to the weak isospin. Because of their non-coupling to the weak force, they are called *sterile* neutrinos. There is no evidence yet for sterile neutrinos.

See-saw mechanism

The see-saw mechanism is based on the assumption that the total lepton number L is violated on a large scale by a right-handed Majorana mass term. Both Majorana and Dirac mass terms are present, half of neutrinos thus being light as current measurements indicate, the other half being heavy Majorana particles with masses possibly as large as the GUT scale [8].

[27] WMAP - Wilkinson Microwave Anisotropy Probe
[28] SDSS - Sloan Digital Sky Survey
[29] 2dF Galaxy Redshift Survey

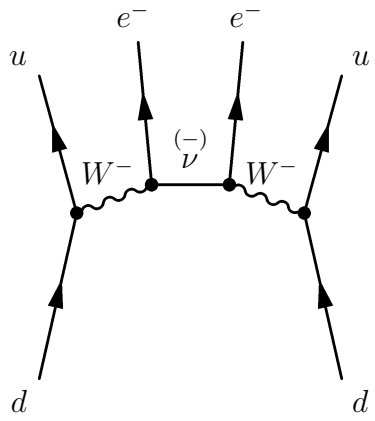

Figure 2.9: Neutrinoless double beta decay: A d quark in each neutron is changed to a u quark producing a proton.

2.5.4 Neutrinoless Double Beta Decay

Usually, in double β decays two neutrinos are emitted. Should neutrinos indeed be Majorana particles, neutrinoless double beta decay ($0\nu\beta\beta$) could occur as a standard model process of second order as shown in Figure 2.9. Conventional beta decay could then be suppressed by the small phase space associated with four particles in the final state compared to two for the neutrinoless decay. The search for $0\nu\beta\beta$ is a very sensitive method of determining neutrino masses. The detection of $0\nu\beta\beta$ would also show that neutrinos are Majorana particles and hence that lepton number is not conserved.

The the $0\nu\beta\beta$ half-life can be calculated as shown in [53]:

$$\begin{aligned}[T^{0\nu}_{1/2}]^{-1} &= G_{0\nu}(\Delta E, Z) \left| M^{GT}_{0\nu} - \frac{g_V^2}{g_A^2} M^F_{0\nu} \right|^2 \langle m_{\beta\beta} \rangle^2 \\ &\equiv G_{0\nu}(\Delta E, Z) \, |M_{0\nu}|^2 \, \langle m_{\beta\beta} \rangle^2 .\end{aligned}$$

$G_{0\nu}(\Delta E, Z)$ comes from the phase-space integral depending on the nuclear charge Z and can be calculated reliably, g_A and g_V are the weak axial-vector and vector coupling constants, and the M are nuclear matrix elements of Gamow-Teller-like and Fermi-like two-body operators which can, with crucial uncertainty, be calculated. The goodness of the calculations can then be tested for conventional $2\nu\beta\beta$ decays. However, an uncertainty of a factor between 3 and 5 still remains. Sensitivity to the neutrino mass comes through the factor

$$\langle m_{\beta\beta} \rangle = \left| \sum_i m_j U^2_{ei} \right|$$

in general containing complex CP phases.

A claim for the observation of neutrinoless double beta decay of ^{76}Ge came in 2002 from part of the collaboration of the Heidelberg-Moscow experiment operating in the Gran Sasso Laboratory [54]. $0\nu\beta\beta$ decay of ^{76}Ge releases an energy of $Q = 2039\,\mathrm{keV}$. The energy spectrum taken by the five Ge detectors shows seven peaks in the region between 2000 and 2100 keV of which one was attributed to $0\nu\beta\beta$. There has been a controversial discussion on the results and a re analysis was published in 2004 [55] indicating a $0\nu\beta\beta$

half-life of ^{76}Ge of $T^{0\nu}_{1/2} = (0.35-2.03)\times10^{25}$ y with a best value of 1.19×10^{25} y translating to an effective Majorana neutrino mass $m_{ee}/h = (0.29 - 0.60)\,\mathrm{eV}$ with a best value of $m_{ee}/h = 0.44\,\mathrm{eV}$. h is a normalization parameter reflecting uncertainties of the nuclear matrix elements varying from 0.6 to 2.8. These results have not been confirmed by other experiments

CUORICINO[30] is a cryogenic experiment located at Gran Sasso on the search for $0\nu\beta\beta$ decay of ^{130}Te at a temperature of $T = 8\,\mathrm{mK}$. The Q-value for the reaction is $Q = 2528.8 \pm 1.3\,\mathrm{keV}$ and the increase in temperature by the release of this energy can be recorded by the experiment. No signal in the region of $0\nu\beta\beta$ has been found, a lower bound for the half time of $T^{0\nu}_{1/2} \geq 1.8 \times 10^{24}$ y leads to an effective Majorana mass of $|\langle m_{\beta\beta}\rangle| \leq (0.2 - 1.1)\,\mathrm{eV}$ [56].

[30]Italian for small CUORE - Cryogenic Underground Observatory for Rare Events

Chapter 3

The OPERA Experiment

The OPERA[1] experiment is part of the CNGS project designed to search for ν_τ appearance in a ν_μ beam. OPERA is a long baseline experiment located in the LNGS[2] underground laboratory at the Gran Sasso massif in Italy. The CNGS facility at CERN provides an intense ν_μ beam with a very small contamination of other neutrino flavors in the direction of the Gran Sasso laboratory at a distance of 732 km. The OPERA detector consists of a 1.8 kton lead target interlaced with photo emulsions to record neutrino events. A series of electronic detectors provides information on the time and place of an event, as well as the momentum of charged secondary particles.

This chapter is divided into three parts. At first, the physics motivation for the OPERA experiment is given in Section 3.1. Neutrino beams and especially the CNGS beam are then described in Section 3.2. Finally, Section 3.3 comprises a description of the OPERA detector with an emphasis on the precision tracker.

3.1 Physics Motivation

The disappearance of atmospheric ν_μ has been well established. Data from different experiments disfavor the possibility of $\nu_\mu \leftrightarrow \nu_e$ oscillations. The interpretation of the observed ν_μ disappearance in terms of $\nu_\mu \leftrightarrow \nu_{\text{sterile}}$ is also disfavored with respect to $\nu_\mu \leftrightarrow \nu_\tau$ oscillations. Though the disappearance of atmospheric ν_μ has been shown in numerous experiments (see Section 2.4.2), the direct appearance of a different neutrino type could not yet be observed. The CNGS long baseline accelerator ν_μ beam can be used to probe the atmospheric neutrino deficit and confirm the preferred $\nu_\mu \leftrightarrow \nu_\tau$ oscillations.

Considering the fact that Δm^2_{21} is small and ignoring possible CP violation and matter effects, the probabilities for appearance in accelerator oscillation experiments are following

[1] Oscillation Project with Emulsion tRacking Apparatus
[2] LNGS - Laboratori Nazionali del Gran Sasso

from 2.1:

$$P_{\nu_\mu \to \nu_\tau} = \sin^2 2\theta_{23} \cos^4 \theta_{13} \sin^2 \left(\Delta m^2_{32} \frac{L}{4E} \right)$$
$$P_{\nu_\mu \to \nu_e} = \sin^2 2\theta_{13} \sin^2 \theta_{12} \sin^2 \left(\Delta m^2_{32} \frac{L}{4E} \right)$$
$$P_{\nu_e \to \nu_\mu} = \sin^2 2\theta_{13} \sin^2 \theta_{12} \sin^2 \left(\Delta m^2_{32} \frac{L}{4E} \right)$$
$$P_{\nu_e \to \nu_\tau} = \sin^2 2\theta_{13} \cos^2 \theta_{12} \sin^2 \left(\Delta m^2_{32} \frac{L}{4E} \right)$$

In the case of a small θ_{13}, as indicated by CHOOZ and Palo Verde, $\nu_\mu \to \nu_\tau$-oscillation has a dominating appearance probability. Furthermore results from Super-Kamiokande, Soudan2 and MACRO indicate maximum mixing for atmospheric neutrinos and hence $\sin^2(2\theta_{23}) \simeq 1$, leaving P depending only on mass eigenstates $|\nu_2\rangle$ and $|\nu_3\rangle$. It can then be treated in the two flavor model described in Section 2.3.3:

$$P_{\nu_\mu \to \nu_\tau} = \sin^2 \left(\frac{1.27 \Delta m^2_{32} L}{E_\nu} \right).$$

From the results of Super-Kamiokande, Δm^2_{32} has been pinned down to approximately $2.4 \times 10^{-3}\,\mathrm{eV}$ as shown in Section 2.4.2. The oscillation probabilities for a ν_μ-beam with an energy of 17 GeV for different mass splittings in the region allowed by atmospheric data are shown in Figure 3.1. The detector setup in the Gran Sasso underground laboratory ensures a very low background, thus the observation of even a few ν_τ events will be a significant indication for $\nu_\mu \to \nu_\tau$ oscillations.

However, due to the very good electron identification, OPERA is also sensitive to $\nu_\mu \leftrightarrow \nu_e$ oscillations. Assuming $\Delta m^2_{32} = 2.5 \times 10^{-3}\,\mathrm{eV}^2$, OPERA has potential to observe ν_e if θ_{13} is close to the CHOOZ limit of $\sin^2 2\theta_{13} < 0.14$ [37]. In case of no ν_e observation, OPERA will be able to set a limit of $\sin^2 2\theta_{13} < 0.06$ at a 90% CL [57], [58].

3.2 The CNGS Beam

Neutrino beams are mainly produced by shooting high energy protons on a target. When these protons collide with the atomic nuclei in the target, a secondary beam of mostly pions and kaons is produced, which can be guided through a system of magnetic horns to a certain direction. Eventually, the pions and kaons will decay producing in most cases a muon and its corresponding neutrino. The high energy of the secondary mesons and therefore the high energy of the center of mass causes the decay products to also fly in the same direction. A beam dump then stops most of the particles except for the muons and neutrinos. By sending the beam inside the Earth, most muons will also be absorbed within one kilometer [59] and only the neutrinos will travel on.

3.2.1 CNGS

The CERN Neutrinos to Gran Sasso (CNGS) are produced as explained in the previous section. For the proton beam all existing proton accelerators at CERN are involved. At

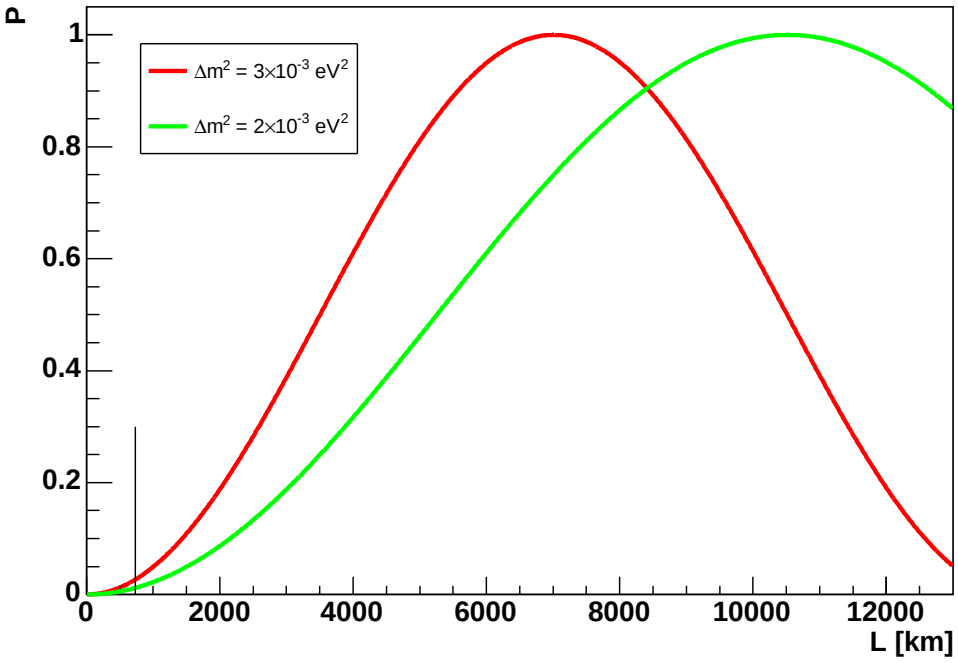

Figure 3.1: Oscillation probability for a 17 GeV neutrino beam for different Δm^2. The black line represents the position of the OPERA detector.

first, the Linac accelerates protons to an energy of 50 MeV. They are then injected to the Booster, which boosts the energy to 1.5 GeV and are then transferred to the PS where they reach an energy of 14 GeV before they are transferred to the Super Proton Synchrotron (SPS). In the SPS the protons reach their final energy of 400 GeV. They are then extracted by a system of kicker magnets into an 800 meter long beam transfer line towards the target. The extraction occurs in 10.5 μs short pulses with a designed intensity of 2.4×10^{13} pot[3] per pulse. At the end of this beam line, the protons are traveling in the direction of Gran Sasso, shortly before hitting a helium cooled graphite target [60]. The secondary particles produced in the collision are most importantly K^+ and π^+ which are focused using two magnetic horns into a 992 m long evacuated decay tunnel. These mesons decay predominantly via the decay modes

$$K^+ \rightarrow \mu^+ + \nu_\mu$$
$$K^+ \rightarrow \pi^+ + \pi^0$$
$$\pi^+ \rightarrow \mu^+ + \nu_\mu$$

thus producing an intense ν_μ-beam. By observing the muons in two detectors behind the proton dump, it is possible to monitor the intensity, direction and profile of the neutrino beam. The basic layout of CNGS is shown in Figure 3.2. With a slope of 5.6% or roughly 3.5°, the decay tunnel points directly to the Gran Sasso tunnel laboratory at a distance of 732 km. At a mean beam energy of $E = 17$ GeV, the contamination of $\bar{\nu}_\mu$ is 2.4%,

[3]pot - protons on target

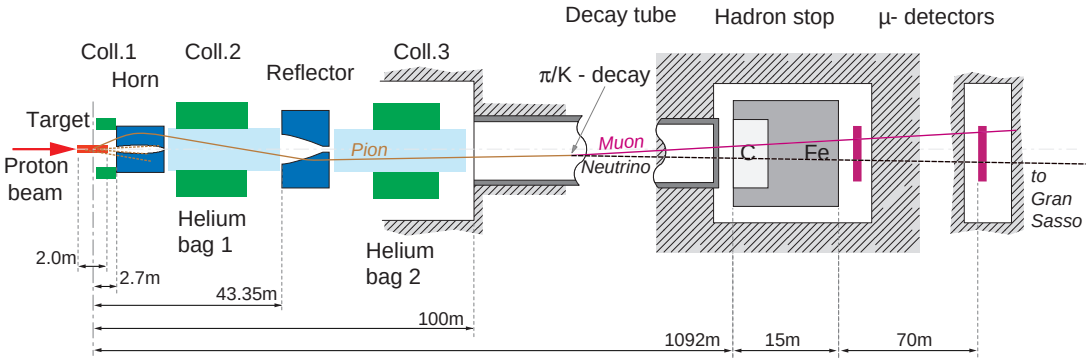

Figure 3.2: Layout of the CNGS beamline with an example of the $p(N) \rightarrow \pi^+(X) \rightarrow \mu^+\nu_\mu$ production process.

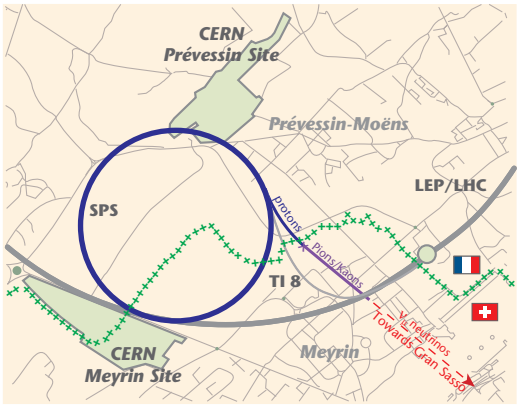

Figure 3.3: Map of the CNGS setup in the CERN surrounding

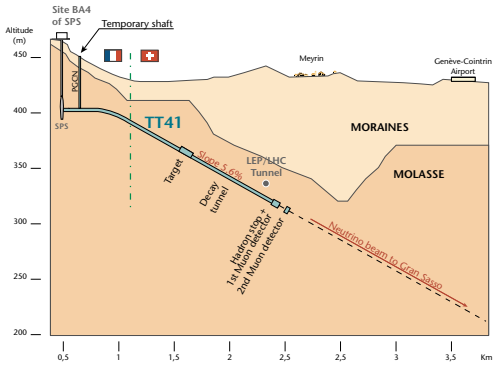

Figure 3.4: Depth profile of the CNGS setup.

0.89% for ν_e and 0.06% for $\bar{\nu}_e$. The number of ν_τ is negligible. The foreseen intensity for the CNGS beam is 4.5×10^{19} pot/y. Figure 3.3 shows the location of the CNGS setup, the beam's trajectory can be seen in Figure 3.5. From Equation 3.1 it follows that the oscillation probability at full mixing is $P = \sin^2\left(\frac{1.27\Delta m^2 L}{E_\nu}\right)$, implying smaller oscillation probabilities for larger beam energies for a given L. On the other hand, the beam energy must be large enough to produce the heavy τ-lepton ($m_\tau = 1777\,\text{MeV}$) in the detector.

3.3 The OPERA Detector

In this section an overview of the OPERA experiment is given. At first, the detector with all its major components will be described. After that, a more detailed description of the Precision Tracker (PT) which is mainly constructed and assembled by the University of Hamburg will be given. At the end of this chapter the data acquisition is described.

The OPERA detector is a hybrid detector consisting of two identical super-modules each consisting of a 900 ton lead target combined with a scintillator target tracker and

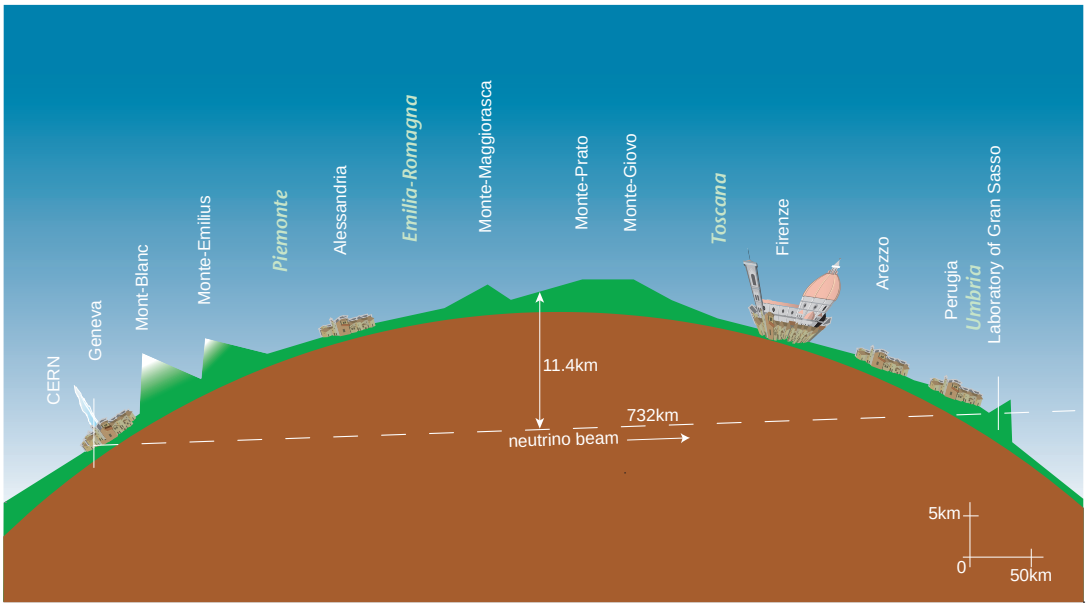

Figure 3.5: CNGS neutrino beam trajectory from CERN to Gran Sasso.

an electronic muon spectrometer. The electronic detector components of the muon spectrometer are located behind the target blocks. They each consist of a magnet and a series of RPCs[4], XPCs[5] and PT[6] drift-tubes. A schematic overview of the detector is shown in Figure 3.6.

Detection of ν_τ-appearance is done via the τ produced in the CC reaction

$$\nu_\tau + N \rightarrow \tau^- + X.$$

The τ lepton has a lifetime of only $\tau_\tau = (290.60 \pm 1.0) \times 10^{-15}$ s or $c\tau = 87.11\,\mu$m and will decay further. The most common decays are either one prong (electron, muon or hadron) or three-prong decays with the possibility of further neutrals:

$$\begin{aligned}
\tau^- &\rightarrow \mu^- \bar{\nu}_\mu \nu_\tau && 17.36\,\%\,\text{BR} \\
\tau^- &\rightarrow e^- \bar{\nu}_e \nu_\tau && 17.84\,\%\,\text{BR} \\
\tau^- &\rightarrow h^- \nu_\tau (n\pi^0) && 48.67\,\%\text{BR} \\
\tau^- &\rightarrow \pi^-\pi^+\pi^- \nu_\tau (n\pi^0) && 14.57\,\%\text{BR}.
\end{aligned}$$

3.3.1 τ-Detection

In the OPERA experiment, τ-detection is done in a massive lead/emulsion target through the ECC[7] technique. In each super-module more than 100 000 ECC modules - called bricks - are placed, each consisting of a stack of 56 layers of lead of a thickness of 1 mm, interleaved with 44 μm thick emulsion layers on both sides of a 205 μm thick plastic base.

[4]RPC - Resistive Plate Chamber
[5]XPC - Crossed resistive plate chambers
[6]PT - Precision Tracker
[7]ECC - Emulsion Cloud Chamber

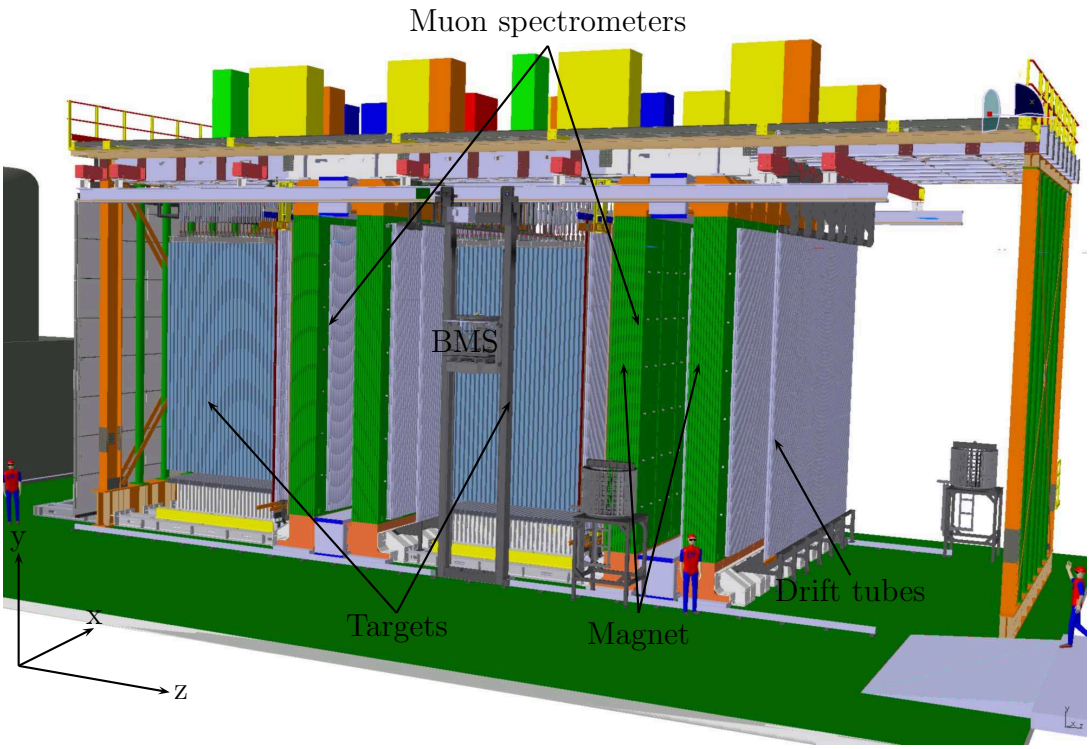

Figure 3.6: Schematic layout of the OPERA detector. The detector consists of two identical super modules. In the picture, super module I is to the left and super module II is to the right. The CNGS neutrino beam hits the detector from the left side. BMS stands for Brick Manipulating System.

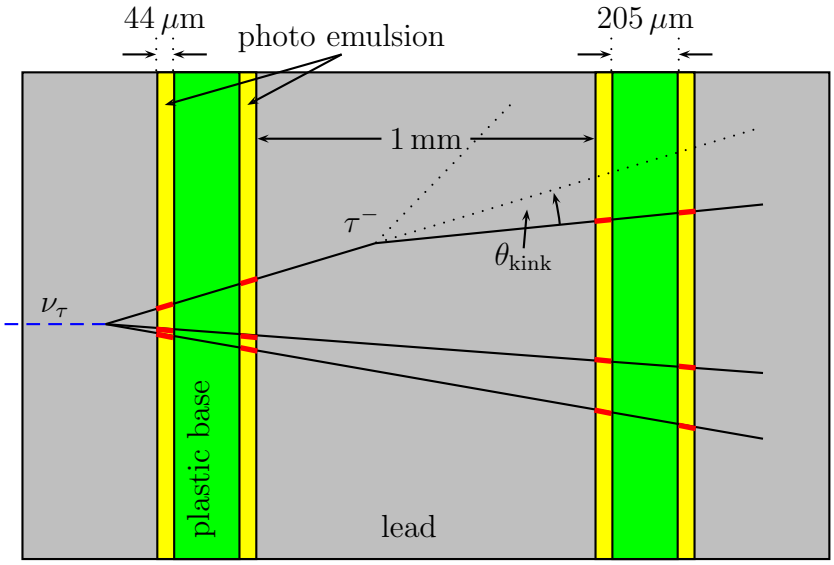

Figure 3.7: Schematic design of a brick including a typical τ decay topology.

The schematic layout of a brick can be seen in Figure 3.7. An ECC brick is finalized on its downstream face by two additional emulsion layers, the so called *changeable sheet* (CS). The ECC technique has lead to the first observation of ν_τ interactions by the DONUT experiment. The bricks are assembled by the BAM[8] also located at the Gran Sasso laboratory. It consists of robots for the automatic packing of the bricks and produces at a rate of two bricks per minute. The bricks have a size of $12.7 \times 10.2 \times 7.5\,\mathrm{cm}^3$ and are arranged in 31 walls per super-module each wall consisting of 64 rows with 52 bricks each. The target covers an area of approximately $7 \times 7\,\mathrm{m}^2$.

The photo emulsion gel has been developed in cooperation of Nagoya University and Fuji Photo Film Co. Ltd. in Japan. The so called "OPERA film" uses sensitive substances that are the same as for photographic films, i.e. micro-crystals of AgBr [61]. The film is produced in Japan and then transported to Gran Sasso, so a lot of background radiation will be recorded before its use. Therefore, a so called refreshing process was implemented in the gel. By adding 5-methylbenzotriazole into the emulsion, the fading properties of the film can be significantly increased. Recorded tracks are erased from the film with time which reduces background but also makes a close to event development necessary. For tracks in the bricks, a spatial resolution of $\Delta x = 1\,\mu\mathrm{m}$ and an angular resolution of $\Delta\theta = 2\,\mathrm{mrad}$ is achieved [58].

Behind every brick wall, crossed polystyrene scintillator strips are placed acting as the target tracker. They are used to detect secondary particles from neutrino interactions and thus determining the bricks to be removed for analysis. Each strip is 6.86 m long and has a cross section of $26.3 \times 10.6\,\mathrm{mm}^2$. They are read out by 1000 photo-multiplier tubes. Once an interaction has been triggered, the brick it took place in can be removed for analysis. This is done by the BMS[9], a fully automatic device to transfer the bricks from the interior of the detector to the outside and vice versa. To insert a brick in a given row, a push arm is used. To remove a brick, a vacuum sucker is utilized. Two

[8]BAM - Brick Assembly Machine
[9]BMS - Brick Manipulator System

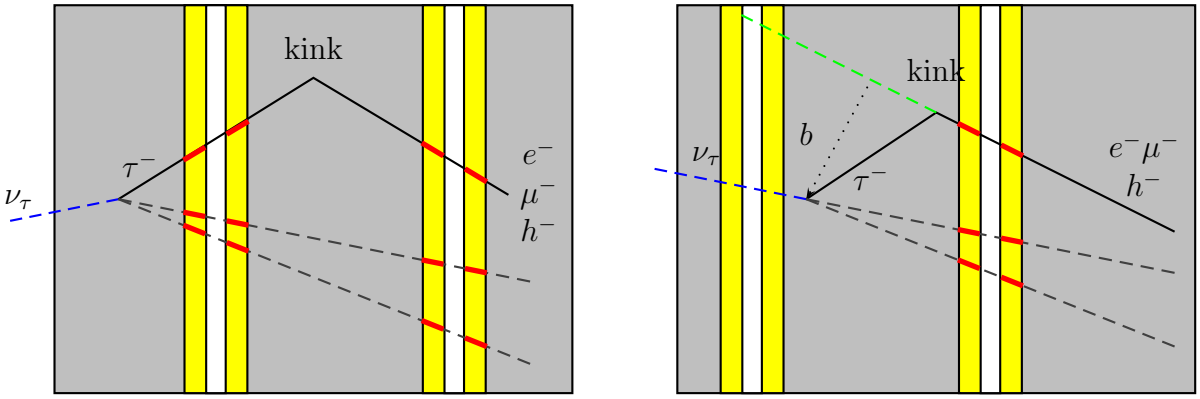

Figure 3.8: Long and short decay of a tau lepton in a brick. For a short decay, only the impact parameter b can be reconstructed.

carousels, one on each side of the detector, provide the possibility of brick storage. If the examination of the changeable sheet does not reveal any interaction, the brick will be returned into the detector, otherwise it will be processed further without replacement in the detector so the target mass will decrease during the run of the detector. After the analysis of the changeable sheet, bricks with neutrino events are brought to the LNGS external laboratory and exposed for several hours to cosmic ray muons for film alignment and then disassembled and developed [62].

With the OPERA detector setup, approximately 30 neutrino interactions per day are expected. Therefore, almost 2000 emulsion sheets or roughly 6000 cm^2 of emulsion must be scanned every day in order to detect the vertex and analyze the event. Due to the refreshing capability of the emulsion and in order to get a close to real time analysis, a fast scanning mechanism is needed which is provided by the *European Scanning System* (ESS) [63]. The ESS is equipped with a high resolution high speed camera and produces a 3 dimensional reconstruction of tracks and vertices. It reaches a speed of 20 cm^2/h and achieves track efficiencies of 95% in the [0,600] mrad range. About 20 ESSs have been installed in European laboratories, five more have been installed at LNGS for the examination of changeable sheets.

Figure 3.8 shows the principles of long and short decays. τ events in the bricks are classified in the following way: in a long decay the produced τ passes through the photo-emulsion before decaying while in short decays it decays within the lead layer it was created in. In the first case, reconstruction of the kink is obvious. The track of the tau as well as of its decay product can be reconstructed and therefore also the kink angle θ_{kink} can be determined. For the latter case, one can only determine the impact parameter, the reconstruction of θ_{kink} is not possible.

3.3.2 The Muon Spectrometer

While the ECC technique is capable of reconstructing the vertex of the neutrino interactions as well as tracks of secondary charged particles, mostly neither information on their momentum and energy can be obtained, nor can the type of particle be determined.

The muon spectrometers are needed for the identification of muons and the determi-

nation of their momentum and sign of charge so that a study of the muonic τ-channel can be performed. Also a suppression of background from the decay of charmed particles which have the same decay topology can be achieved.

Electrons from the electronic decay channel of the τ-lepton will loose their energy mainly through bremsstrahlung. Starting with an energy of E_0 the energy E_e of an electron after the distance x is given by

$$E_e(x) = E_0 \cdot e^{-\frac{x}{x_0}}$$

with the radiation length x_0 depending on the material the electron is traversing through. Lead has a radiation length of 0.56 cm, and hence a lot of energy is released when an electron traverses the lead resulting in secondary particles which can be observed as particle showers. Analysis of these particle showers produced through bremsstrahlung provides information on the energy of the primary electron.

Hadrons produced through the hadronic decay channel of the τ-lepton also produce particle showers. These hadronic showers occur due to the energy loss from ionization of the traversed material. The hadrons energy is given by

$$E_h(x) = E_0 \left(1 - \frac{dE}{dx}x\right)$$

where the energy loss per distance traveled is given by the Bethe-Bloch formula

$$-\frac{dE}{dx} = Kz^2\frac{Z}{A}\frac{1}{\beta^2}\left[\frac{1}{2}\ln\left(\frac{2m_e\beta^2\gamma^2T_{\max}}{I}\right) - \beta^2 - \frac{\delta(\beta\gamma)}{2}\right] \tag{3.1}$$

with $K = 4\pi N_A r_e^2 m_e$, ze the charge of the incident particle, Z and A the atomic number and mass of the absorber respectively, m_e the electron mass, β the particle's velocity in units of the speed of light, γ the relativistic gamma factor, $T_{\max} = \frac{2m_e\beta^2\gamma^2}{1+2\gamma m_e/M+(m_e/M)^2}$ the maximum kinetic energy which can be imparted to a free electron in a single collision by a particle of mass M, I is the mean excitation potential of the target, N_A Avogadro's constant and $\delta(\beta\gamma)$ a density effect correction to ionization energy loss [8]. Hence the specific energy loss depends mainly on the particles Energy and the properties of the traversed medium. Figure 3.9 shows $-\frac{dE}{dx}$ distributions for different particles and mediums. For a given medium like lead both the particle and its momentum can be identified by their specific energy loss.

Unlike electrons and hadrons, high energy muons from the muonic decay channel pass the detector without significant energy loss. Their momentum is measured in the precision tracker by the bending of their tracks in the magnet.

Each of the two muon spectrometers consists of a dipole magnet with vertical field lines of opposite directions in the two magnet walls. Between the arms of each magnet, two approximately 8 m long drift tube walls are located to measure the bending of muon tracks. Two further drift tube walls are located on either side of the magnet. The iron plates of the magnets' arms are interlaced with RPC planes for track reconstruction inside the yoke. They can also perform a range measurement of stopping particles as well as a calorimetric analysis of hadrons [64].

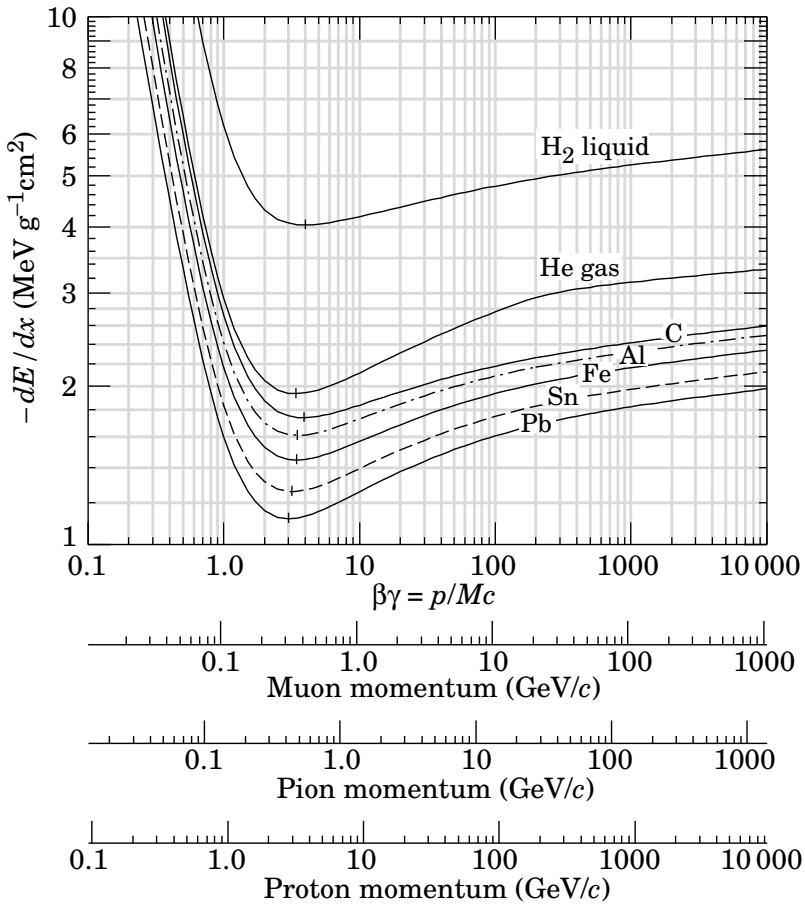

Figure 3.9: Mean energy loss in different mediums for protons, pions and muons.

Magnet

The central part of each muon spectrometer is the dipole iron magnet. It is made of tow iron arms with a total weight of 900 tons and a size of $8.75 \times 8.2\,\mathrm{m}^2$. A magnet arm consists of a total of 12 iron plates. Between the 5 cm iron layers there is a space of 2 cm for the RPCs. A current of $I = 1200\,\mathrm{A}$ in top and bottom copper coils induces the magnetic field of measured 1.52 Tesla [62].

RPCs

The RPCs are used for track reconstruction inside the magnet walls. The energy deposition of hadronic showers produced through multiple scattering in the iron can also be measured. Also, the RPC planes serve as a trigger for the precision tracker described in Chapter 3.3.3.

A RPC consists of 2 mm thick high resistive ($\rho > 5 \times 10^{11}\,\Omega\,\mathrm{cm}$) Bakelite electrodes. The sensitive element is a 2 mm thick gas layer under a uniform steady electric field of 8 kV generated by the parallel electrode plates [65]. Upon the crossing of a charged particle, an electric discharge is initiated providing large amplitude signals of about 100 mV which

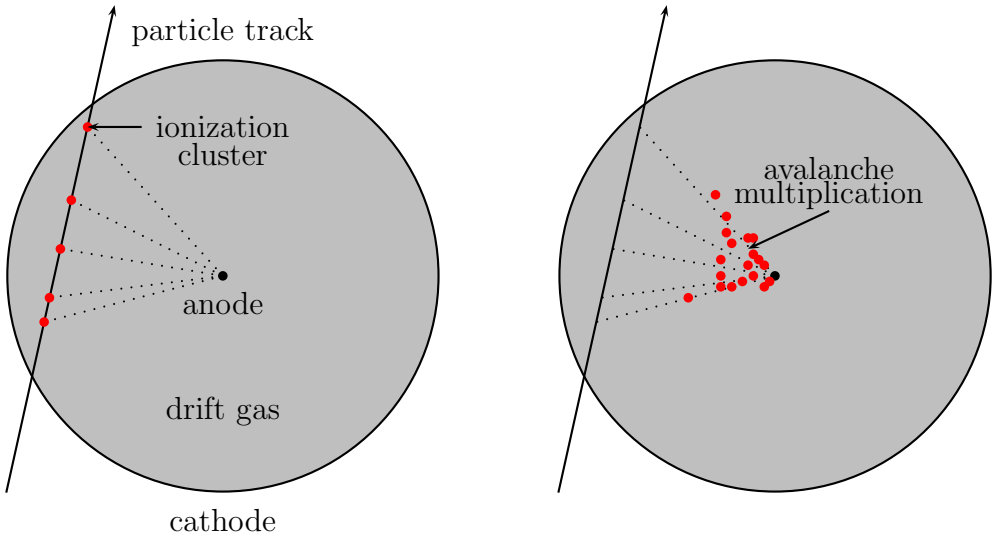

Figure 3.10: A drift tube with a particle track. A charged particle leaves ionization clusters along its trajectory. These charges will be collected at the electrodes. If a strong electric field is applied between the electrodes, avalanche multiplication will occur. The red dots show electrons from the ionization pairs. The drifting electrons leave a tail of positive charged ions which are slowly drifting to the cathode and not shown here.

are read out via copper electrodes placed on both sides of the RPC at equal distances of 30 mm. Twisted pair cables connect the electrodes to the read out electronics on top of the magnet. 21 RPCs with a cross section of $2.9 \times 1.1\,\mathrm{m}^2$ are arranged in 7 rows and 3 columns per wall. There is a total of 22 RPC planes in each super-module. RPCs are operated with a gas mixture of argon, tetrafluoroethane and isobutane at a 75.4/20/4 mixing ratio with a small addition of SF_6 (0.6%) [66]. Two layers of glass RPCs in front of the first target are used as a veto to detect muons originating from the rock, the neighboring Borexino experiment, or cosmic muons in beam direction.

Two additional glass RPC planes with inclined strips at an angle of 42.6° are located in front of the magnet. These so called XPCs are used to solve ambiguities in the track spatial-reconstruction.

3.3.3 The Hamburg Precision Tracker

The precision tracker is used for measuring the muon track coordinates in the horizontal plane. It can also determine the muon's sign of charge and momentum. This section gives an overview over the drift tube technique used by the precision tracker and describes their implementation for the OPERA experiment.

Drift tubes

Drift chambers use the ionization of gases by charged particles to detect and reconstruct particle tracks. While traveling through the gas, charged particles loose energy by ionization and atomic excitation. The specific energy loss is given by the Bethe-Bloch equation (see Equation 3.1). Also, bremsstrahlung has to be considered. Applying an electric field

to the gas, the ionization pairs will start drifting to the anode and cathode according to their charge. The lighter electron will travel much faster to the anode than the heavier positive charged ions towards the cathode. The energy loss of the electrons will be counterparted by the acceleration in the electric field. Arranging the field with a centered anode and a surrounding cathode as shown in Figure 3.10 results in an electric field

$$E(r) = \frac{U}{\ln(r_c/r_a)} \cdot \frac{1}{r}$$

where r_c and r_a are the radii of the cathode and anode wire respectively. U denotes the applied voltage. This field is weak on the outside getting exponentially stronger towards the center. This radial symmetry is realized in drift tubes. A wire in the center is connected to a high voltage acting as the anode while the tube itself functions as the cathode. Electrons from ionization clusters will be attracted by the anode in the center. While traveling through the gas they will excite and ionize more atoms and molecules thus more and more free electrons will drift towards the anode. This avalanche multiplication results in an electric signal which can be measured [67].

To determine the position of a track within a tube, the measurement of drift times is necessary. Next to the time of a signal on an anode wire an external trigger has to provide a time signal of the passing primary particle. The time difference between the undelayed trigger and the drift tube signal is the drift time. For a more detailed look at the trigger layout and drift time determination see Section 3.3.4. The position of the track can then be determined by the drift time distance relation. This relation has to be obtained by calibration measurements. Comparing the drift times with the drift time distance relation allows to reconstruct only the distance of a track from the center of a tube. Hence measurements from different tubes are required to reconstruct a particle track.

The Precision Tracker

The (Hamburg) Precision Tracker ((H)PT) consists of aluminum drift tubes, arranged in six walls à four layers per super module. Each wall is build of 4×12 tube modules with either 15 (HPT 1 and 6 in SM1 and HPT 1 in SM 2) or 17 (all others) modules per wall adding up to a total of 198 modules or 9504 drift tubes. Each tube has an outer diameter of 38 mm, a wall thickness of 0.85 mm and is 7.9 m long (7.75 m inside the magnet). In the center of each tube, a gold-plated tungsten wire of 45 μm diameter is strung. A mixture of Ar and CO_2 in the ratio 80/20 is used as drift gas at a pressure of 1005 mbar (absolute). Each module is 50 cm wide, each layer is shifted with respect to the adjacent one, thus guaranteeing high track reconstruction efficiency. This staggering has been optimized by Monte Carlo simulations using the expected angular distribution of the muon tracks. For a track reconstruction in two consecutive planes at least four hits are required.

With this experimental setup, the precision tracker can measure muon track coordinates in the horizontal plane. When a muon passes the spectrometer, it is deflected by each of the magnet walls forming an S-shape curve as shown in Figure 3.11. Due to the anti-parallel magnetic fields of the magnet, each deflection will be by the same angle $\frac{\theta}{2}$. The total deflection angle θ is defined as the sum of the amount of each reflection. θ can

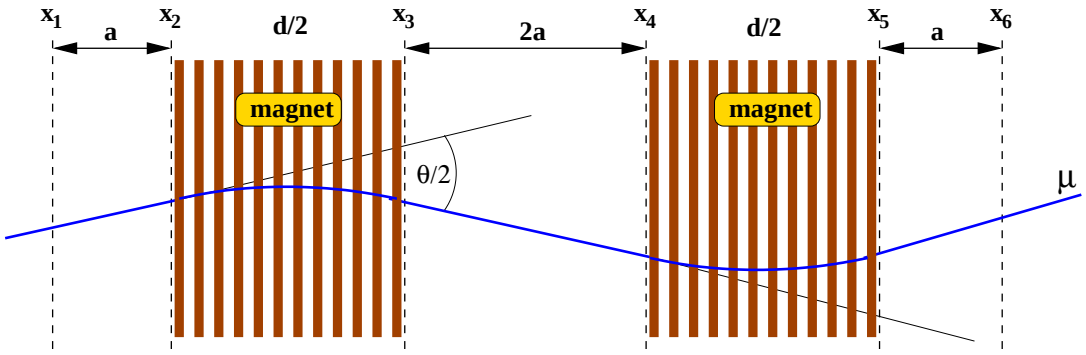

Figure 3.11: Deflection of muons in the OPERA muon spectrometer. The dashed lines represent the positions of the precision tracker walls.

be determined from the precise measurements of the muons track, its momentum can then be found using the following relation:

$$\theta = \frac{eBd}{p}$$

valid for small angles θ, where d is the gage of the magnet arms, B the magnetic field and e the elementary charge.

Each module is equipped with four high voltage distribution (HV) boards each connected to a row of twelve tubes. A high voltage of $U = 2350\,\mathrm{V}$ is connected to each HV board and thus applied to all anode wires. An amplifier and discriminator (*preamp*) board is connected to each HV board. It carries an amplifier for event signals as well as a discriminator and circuits for threshold setting, temperature monitoring and test pulse generation [68]. The preamp boards are connected to the read out electronics on top of the detector. The OSUB[10] board provides the interface for temperature, threshold and test pulse settings, TDC[11] boards are used for determining drift times in the drift tubes.

3.3.4 PT Data Taking

When a muon passes the detector, it most likely interacts with any of the spectrometers - XPC, RPC and PT as well as the target tracker. The precision tracker by itself is only able to determine the (x, z)-coordinates. Information on the y-coordinate has to be obtained from other parts.

A signal on an anode wire is amplified by the preamp boards on top of each module and sent to the TDC boards where the time measurement of t_{TDC} starts. To determine the drift time, a stop signal is needed. This is provided by the OTB[12]. For each pair of drift tubes in front of, inside and behind the magnet, a trigger station is set up using two OTBs which provide a variety of trigger schemes. The default scheme is a majority coincidence of at least three planes of RPCs and XPCs as shown in Figure 3.12. After a delay, which can be varied between $t_{\mathrm{delay}} = 1.6\,\mu\mathrm{s}$ and $2.2\,\mu\mathrm{s}$ it reaches the TDC and serves

[10] OSUB - OPERA SUpport Board
[11] TDC - Time to Digital Converter
[12] OTB - OPERA Trigger Board

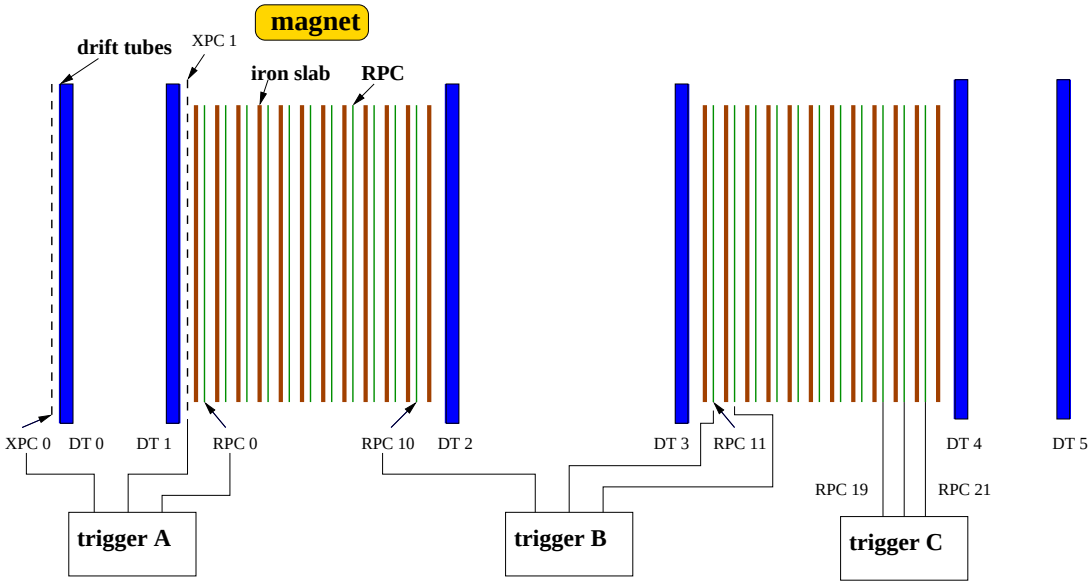

Figure 3.12: Trigger scheme of one super module.

sub-detector	sensor ids
Target Tracker	0-991
RPCs	992-1013; 1018–1039
XPCs	1014-1017; 1040-1043
PT	1052-1160

Table 3.1: Sensor ids for the different sub-detectors. A detailed overview of the PT TDC mapping can be found in appendix B.

as a stop signal. Assuming the trigger signal was produced in the same instance when the electron shower started in the drift tube, the drift time can be determined through $t_{\text{drift}} = t_{\text{delay}} - t_{\text{TDC}}$. Signal delays due to different cable lengths have to be accounted for. This is done through test pulse measurements. Test pulses can be generated on the OSUBs. The results from these measurement will then be used in the data analysis for correction. First test pulse measurements showed an accuracy of 500 ps. The TDC has a dynamic range of 3200 ns and uses a 12 bit interface to store the data. Therefore the measured value is transformed into a time measurement by a factor of $\frac{3200}{2^{12}} = \frac{25}{32}$. Besides the drift times, a signal width is also recorded by the TDC. The raw-data is written to a database or can be dumped to an ASCII-File.

Data analysis starts with the extraction of data from the database. For a certain event range two files are extracted, one containing header information and the second one containing the actual data. Information from different sub-detectors are all written to the same file but can be distinguished by the sensor id (see appendix B). Each TDC is connected to two drift tube modules so that there are $2 \times 48 = 96$ incoming channels per TDC. The channel number is also recorded and can be assigned to a specific tube, so that the knowledge of the sensor id and channel id gives the exact location in the precision tracker [68].

A synchronization between events in the OPERA detector and beam spill times will

Δm^2_{23} [10^{-3} eV^2]	1.9	2.4	3.0	Background
1.8 kton fiducial	6.6 (10)	10.5 (15.8)	16.4 (24.6)	0.7 (1.1)
+ improvements	8.0 (12.1)	12.8 (19.2)	19.9 (29.9)	1.0 (1.5)
+BG reduction	8.0 (12.1)	12.8 (19.2)	19.9 (29.9)	0.8 (1.2)

Table 3.2: The expected number of τ-events. The numbers in brackets are for a CNGS upgrade by a factor 1.5 in intensity. Improvements can be achieved through improved brick finding and 3 prong decay analysis [58].

be done through GPS[13]. This reduces background from cosmic muons or environmental radioactivity significantly. The local GPS system also distributes a general 10 ns time signal to synchronize internal clocks on the TDCs mezzanines in order to provide accurate time stamps for each event.

3.3.5 Performance

Expected events

In a five year run about 31000 ν_μ CC and NC reactions are expected to take place in the OPERA detector. The detection efficiency has been studied in Monte Carlo simulations. For all decay channels an overall τ detection efficiency of 9.1 % has been determined. From this, an expected number of detected events can be derived, depending on the squared mass splitting Δm^2_{23}. The number of detected τ events can be increased by an improvement in the brick identification and an upgrade of the CNGS beam. The estimated number of events for different square mass splitting are shown in Table 3.2.

Background

Because of the small event rate, the OPERA experiment is extremely sensitive to possible background with a signal similar to that of a τ-lepton in the detector. Possible background sources are mainly ν_τ prompt background from the beam, background from π^0 and prompt electrons, background from muon scattering or hadron reinteractions. All these sources have been studied and it has been found, that their contribution is of the order of $10^{-6} \times N_{CC}$ or smaller for each background source. The decay of charmed particles contributes with a slightly higher rate of $1.65 \times 10^{-5} \times N_{\mathrm{CC}}$ [64].

Besides creation of a τ-lepton, there also exists the possibility of the production of charmed mesons like $D^\pm$ mesons. Mass and lifetime of these mesons are comparable to those of the τ-lepton and their decays can only be distinguished by detecting the muon produced e.g. in the reaction

$$\nu_\mu + N \rightarrow D^\pm + \mu^\mp + X.$$

[13]GPS - Global positioning System

Chapter 4

The Software Framework OpRelease

4.1 OpRelease

For simulation and analysis of data taken with the OPERA detector, the software framework OpRelease is being developed. It provides a complete geometry of all the detector components as well as the major surrounding objects mainly the rock and the neighboring experiment Borexino. The software includes programs for event generation from both beam and cosmic neutrinos which can be used in a Monte Carlo (MC) detector simulation. Both data from real and simulated events can be stored in the same data format which can be then processed for further analysis such as track and particle reconstruction.

4.1.1 Data Types and Format

The OPERA file format is based on the ROOT framework. The data structure is managed by the TreeManager defined in the sub-package OpRData of OpRelease. The TreeManager can create and read root files of the OPERA format. A short introduction on how to work with the TreeManager is given in Appendix A.1.

The data is divided into two groups: data and resistant data, the first being used by programs actively changing data whereas the latter is used for accessing data e.g. for analysis. For both groups the data structure is the same, with the only difference in the name of the objects. For any "Data" object a corresponding resistant "RData" object exists. The following explanations are for resistant data.

The TreeManager holds different objects. In RRunHeader, information about the run is stored. This is usually the same for all events. REvtHeader holds general information for each event, such as the event Number, the time of the event or information on whether the event had been on time with a beam spill at CNGS.

Besides these general objects, lists for each sub-detector are stored for each event. The most important lists for this thesis are summarized in Table 4.1. Each List contains a number of entries depending on the kind of sub-detector. For real data these entries are defined as *digits* whereas for simulated events *hits* are created. For each occurrence in a sub-detector for a given event, a digit/hit is added. More lists for Monte Carlo data exist, they can be filled with data for each secondary particle produced in a neutrino reaction. Table 4.2 gives an overview of the contents of a RSDTDigit, which is the digit used for storage of the precision tracker data. The corresponding hit has a similar structure

List in TreeManager	Content	Data
MCParticleList	RParticle	MC secondary particles
TSCINHitList	TSCINHit	Simulated Target Tracker
SRPCHitList	SRPCHit	Simulated RPC
SDTHitList	SDTHit	Simulated PT
XPCHitList	XPCHit	Simulated XPC
TSCINDigitList	RTSCINDigit	Real Target Tracker
SRPCDigitList	RSRPCDigit	Real RPC
SDTDigitList	RSDTDigit	Real PT
XPCDigitList	RXPCDigit	Real XPC

Table 4.1: Important lists managed by the TreeManager

parameter	content
X()	x-position of the tube
Z()	z-position of the tube
SM()	number of Super Module [1-2]
Plane()	number of plane [1-6]
Layer()	number of layer [1-4]
Tube()	number of tube [1-180/204]
DriftTime()	drift time
Time()	time stamp
SignalWidth()	signal width

Table 4.2: contents of a RSDTDigit or SDTHit

but holds additional information which do not necessarily have to be measurable by the detector component. Data that has already been used for analysis is stored in *used* lists. The name of these lists is just an extended version of the original list, always following the same scheme: a SDTDigitList e.g. would become a SDTDigitUsedList. Used lists only exist for resistant data.

4.1.2 OPERA Geometry

The geometry of the detector and its surroundings is handled by the sub-package OpGeom. It has been developed on the basis of ROOT's TGeoManager and can hence be easily accessed within the analysis framework. Within this geometry, different volumes are defined. OpRelease operates in different modes containing different volumes. The surrounding volumes of the detector are defined as tubes, with WRLD being the top volume with a length of 400 m and a diameter of 200 m. The actual detector with all its components is implemented into a big box called OPDY. The FULL mode contains all volumes while in OPERA mode only elements included in OPDY are considered. The package OpDisplay supplies a fully 3d detector visualization within the ROOT framework.

4.2 Monte Carlo Simulation

4.2.1 Event Generation

Events can be generated by OpNegn. Based on incoming neutrinos from FLUKA simulations, OpNegn is capable to simulate NC and CC reactions as well as quasi elastic scattering with nuclei. A list of secondary particles is created and written to both ASCII and root file. Particles are identified by pdg particle codes [8].

4.2.2 Detector Simulation

The sub-package OpSim reprocesses the events generated by OpNegn. The implementation of ROOTVMC allows to choose among Geant3, Geant4 or FLUKA as the Monte Carlo simulation tool. OpSim creates primary vertices inside the detector geometry. Also the tracks of the secondary particles through the different sub-detectors are created and the corresponding hits are filled.

The sub-package OpDigit is then capable of creating the digits for the different detector components. It takes the ideal MC hits and adds detector typical uncertainties. The MC data is transformed into detector signals. After digitization, the lists of all sub-detectors are filled just like after a real event.

4.3 Data Analysis for the OPERA Experiment

Real data taken from the experiment can be converted to the OPERA format by the package OpRealIO. The software processes ASCII files extracted from the DAQ database and fills the digits for each sub-detector.

Data for the muon spectrometer from both real and simulated events can be processed by OpRec. OpRec reconstructs the tracks of both stopping and through going muons and determines their momentum.

To reduce computing times, the data files can be preprocessed with a cut macro developed in the frame of this thesis. Based on the users definitions, the macro is able to discard complete events and erase single digits/hits from an event.

For quick analysis, several root macros exist to read out the data. Basic characteristics of first events in the commissioning phase have been studied and are presented in Chapter 5. Events can be visualized with an event display macro, which loads all digits from file and creates a two dimensional projection in both the horizontal and vertical plane of the tracks.

Chapter 5

First $\nu_\mu \rightarrow \mu^- + X$ Events

During the last months, the commissioning of both the CNGS beam and the OPERA experiment has started. In August 2006 a first run period with CNGS neutrinos was successfully performed [62]. Because of missing pre-amplifier boards for the precision tracker, only a few modules were fully functioning during this run. In a second run period in late October and early November 2006 all six planes of the precision tracker for SM 1 were included. It was initially planned to take data with the beam running but due to problems at CNGS only cosmic data could be obtained. In late November 2006, a special run for the PT was conducted, again taking cosmic data.

In this chapter, the conversion of the ASCII data provided from the data acquisition (DAQ) to the OPERA root format is shortly described. Data from all runs conducted as yet has been converted, an analysis of selected PT characteristics has been done with cosmic data from the second run and is presented.

5.1 Data Analysis

As mentioned before, data from the precision trackers is collected in a central database together with the measurements from the target tracker and R(X)PCs. From this database, ASCII files can be extracted. For a certain event range, two files are extracted: a header file and a corresponding data file. The header file contains eight columns, containing for each event in order an event number, a cycle number, an id for the sub-detector, the number of sub-detectors which recorded data for the event, the number of TDCs which recorded data, the number of hits and two time stamps.

The data file has at least one entry for each event in the header file. For each TDC involved one line is added. Each line has at least six columns, the first column is filled with the event number corresponding to the header file. It is followed by the TDC sensor number in the second column. It is followed by a time stamp and then the number of hits for that TDC. For each hit, two more columns are added, one with the TDC channel number and the other on with the measured value. For the precision tracker, this number has to be decoded. In order to have the same data scheme of only one value per TDC channel for all detector components, both the the measured drift time and the signal width are encoded in the same number. The signal width is divided into four values: 0, 1, 2 and 3 for no, small, medium and large width respectively.

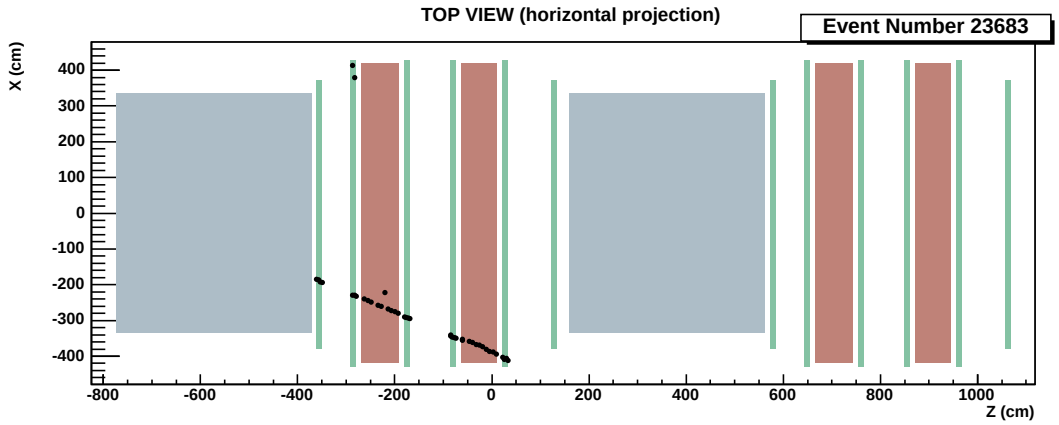

Figure 5.1: Event display showing a track through the RPCs and five PT planes of SM1. The target tracker was not in operation during data taking.

The number is just added as an extra digit to the drift time, so that it can be recovered as data value modulo 10 whereas the drift time is the data value div 10.

A conversion from TDC and channel numbers to plane, layer, module and tube number has been written within this diploma thesis. The exact TDC and channel mapping is described in Appendix B. Together with information from the OpGeom package exact track coordinates of each event in the xz-plane can be reconstructed. A conversion to the official OPERA root format is done in the OpRealIO package. Development on a track reconstruction algorithm within the OPERA software for the precision tracker is currently done in the frame of the PhD thesis of Björn Wonsak.

After the conversion to root files, single events can be easily accessed for further processing. This is done via the TreeManager as described in Appendix A.1. For some applications it is useful to define cuts on the data prior to analyzing. For example, for reconstruction it is useful to exclude events with only two ore three precision tracker hits. This can be done either directly when converting the ASCII data to root - which is depreciated - or by the reconstruction program itself. To simplify things, a macro to modify the root files itself has been written within this thesis preventing the reconversion of the data and allowing the reconstruction program to be used for different cut models without being changed. This cutting tool provides the possibility to either remove whole events from the data which is useful when considering criteria such as number of hits. It is also possible to exclude single hits from an event, which is e.g. done for noisy modules.

5.2 A First Look at Data from Run Period 2

In this thesis, some characteristics of the PT modules are analyzed. The data is taken from run period 2. For the data readout, a primary cut for at least seven PT hits per event[1] has been made leaving a total of 7149 events in the PT.

[1]No cuts are performed during data readout anymore. A tool to apply cuts to the read out root files has been developed in the frame of this thesis which can now be used.

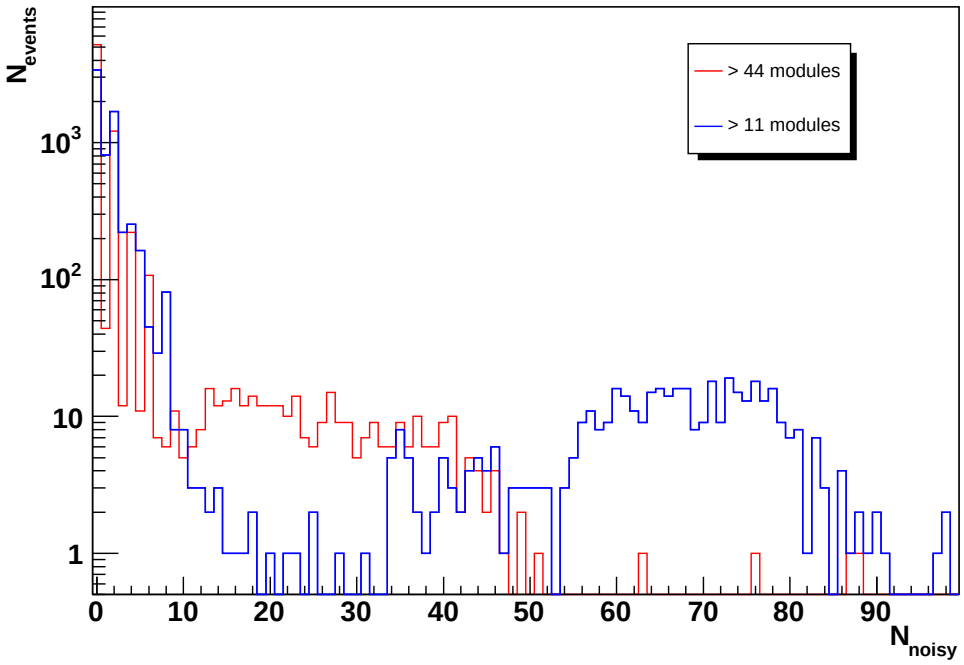

Figure 5.2: Number of noisy modules for all events for different cut criteria

5.2.1 Modules

For each module the number of hits per event has been investigated. The resulting distributions for all 98 modules are presented in Appendix C. A strong peak at the maximum value of 48 can be seen for many modules. This can be explained by a wrong setup of the module's thresholds. The same effect can be seen in Figure 5.3. The figure shows the hits for the single tubes of HPT 3. It can clearly be seen that tubes 145 through 169 for all four layers show an exceedingly high number of hits. These tubes correspond to the 13th and 14th module which are connected to the same OSUB and TDC. Table C.1 summarizes those tubes, that have more than 44 hits in more than 10% of the time. To reduce noisy channels, all modules exceeding 44 hits per event have been excluded from the data in a cut. Also, the total number of hits per event was limited to 47, leaving 5675 events. The effect can be clearly seen in Figure 5.3, showing data of the same PT plane after the cuts have been applied. For both cut and uncut data a clear plateau is notable. However, besides the elimination of the clear peak from modules 13 and 14 through the cut, the level of the plateau is also lowered from an average of about 450 hits to approximately 20 hits. This means that all modules are noisy from time to time with the same probability. For all events the number of modules where more than a specified number of tubes have fired has been analyzed. An average of 1.81 modules has been found out to have more than 44 hits per event. This number goes up to 5.07 when setting the limit to 11 tubes. The corresponding distributions are shown in Figure 5.2. For the criterium of at least twelve hits for a module to be considered noisy there are 3393 events with no noisy module at all while for the $>$ 44 hit criterium this number increases to 5182.

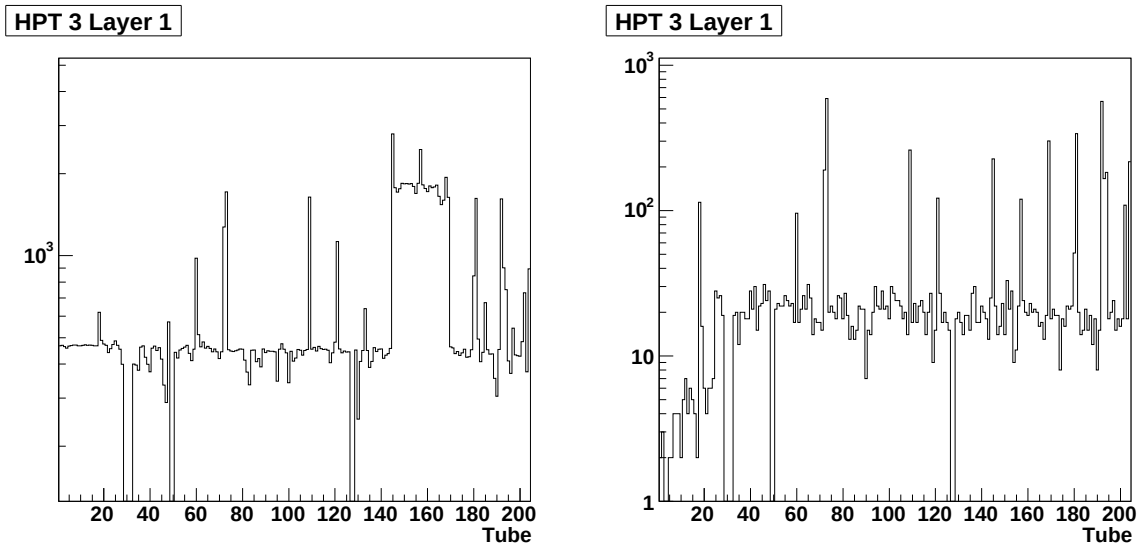

Figure 5.3: Left: Hits per tube for HPT 3 layer 1 without cuts. Right: The same after cuts were applied.

5.2.2 Tubes

The data is very consistent for almost all tubes and all layers. After the cuts are applied, there are only a few noisy tubes remaining. The small number of hits in the example in Figure 5.3 for the first 24 tubes or two modules can possibly be explained with some works on the electronics that were still going on during data taking. Some TDCs have been exchanged during the run leading to inconsistencies in the data. Reducing the maximal allowed number of hits per module to 20 leads to an increase in the number of all events. Because of the more strict cut, more complete modules are excluded from the data, reducing the total number of hits per event and therefore more events fall below the limit of 44.

Figures 5.4 and 5.5 show the number of hits per tube integrated over all events for all planes and layers from the cut data. The number of hits is about equal for all tubes within one plane. However there are some tubes that do not show any hits at all. Table 5.1 summarizes these tubes which seemed not to be functioning during the second run. This tubes have been examined, their functionality could be restored by exchanging broken L3 amplifier chips.

5.2.3 Events

The distribution of the number of hits per event is shown in Figure 5.6. The distribution has a maximum at 17. For a straight track this maximum would be expected to be close to 24, that is one hit per layer. For this data set, cosmic muons have been measured which, due to the geometry of the precision tracker, mostly do not traverse through all planes, hence a smaller number is expected.

Figure 5.7 shows the number of hits in the different planes. It can clearly be seen that the number of hits in HPT 1 and 6 is significantly smaller than in the other planes.

Plane	Layer	Tubes
1	1	58, 67, 85, 86, 87, 88
1	2	37, 38, 39, 40, 50, 55, 70, 72
1	3	57, 58, 62, 63, 64, 65, 66
1	4	54, 72
2	1	49, 57, 73, 84, 86, 87, 88, 90, 93, 94, 96, 161, 188, 193, 198, 200, 201
2	2	52, 79, 80, 82, 83, 84, 86, 88, 89, 90, 91, 92, 93, 94, 95, 96, 157, 193, 194, 196, 197, 198, 199, 204
2	3	13, 49, 50, 51, 52, 74, 76, 77, 78, 79, 80, 82, 83, 84, 86, 88, 89, 90, 91, 92, 93, 95, 195, 196, 197, 198, 200, 202, 203, 204
2	4	73, 76, 79, 80, 82, 86, 88, 89, 90, 93, 95, 161, 194, 196, 198, 200, 204
3	1	3, 4, 29, 30, 31, 32, 49, 50, 127, 128
3	2	46
3	3	1, 154
3	4	2
4	4	153, 154, 155, 156
5	1	147

Table 5.1: Tubes with no hits at all - after cut

This can be explained by the trigger setup. For data taking a four out of seven majority trigger[2] was used. At the time of the run, only the seven RPC planes were in operation as a trigger, the two XPC planes were missing. From a look at the trigger geometry in Figure 3.12 it is obvious, that more cosmic events are detected in the central planes. Also, both HPT 1 and 6 consist of only 15 modules whereas the other planes are made of 17. Therefore a further reduction of the total amount of hits is expected. The number of hits per event has also been analyzed for each plane separately. The results are shown in Figure 5.8. Except for HPT 2, they all have a maximum at four, which would be expected for a straight track with one firing tube per layer.

Figure 5.9 shows the drift time spectrum of the analyzed data. The spectrum has its maximum at approximately $-140\,\text{ns}$. The negative drift times are easily explained by the method of time measurement described in Section 3.3.4. The TDC does not measure the drift times directly, only the time between the event's signal and a delayed stop signal provided by the trigger is measured. The analysis has been done without exact knowledge of the trigger delay. This can be varied between $1.6\,\mu\text{s}$ and $2.2\,\mu\text{s}$, and has been set to $2\,\mu\text{s}$ for the analysis. The data indicates a real delay of $1.86\,\mu\text{s}$ for the used Paoloni Janutta trigger.

[2]Due to a defect of the trigger board, the trigger was provided by a set of NIM electronics. This trigger was then named Paoloni Janutta trigger.

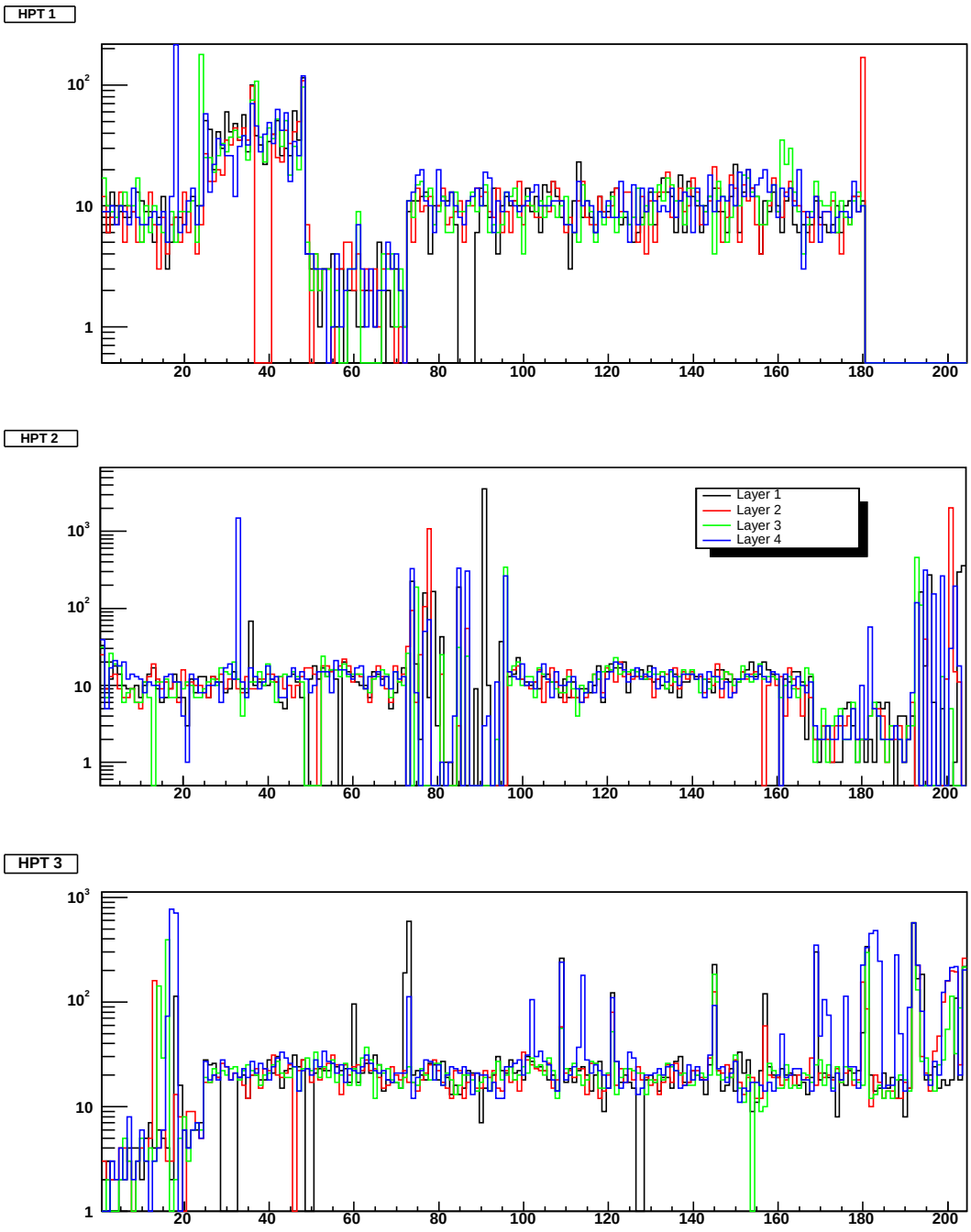

Figure 5.4: Hits per tube for all layers in HPT 1, 2 and 3.

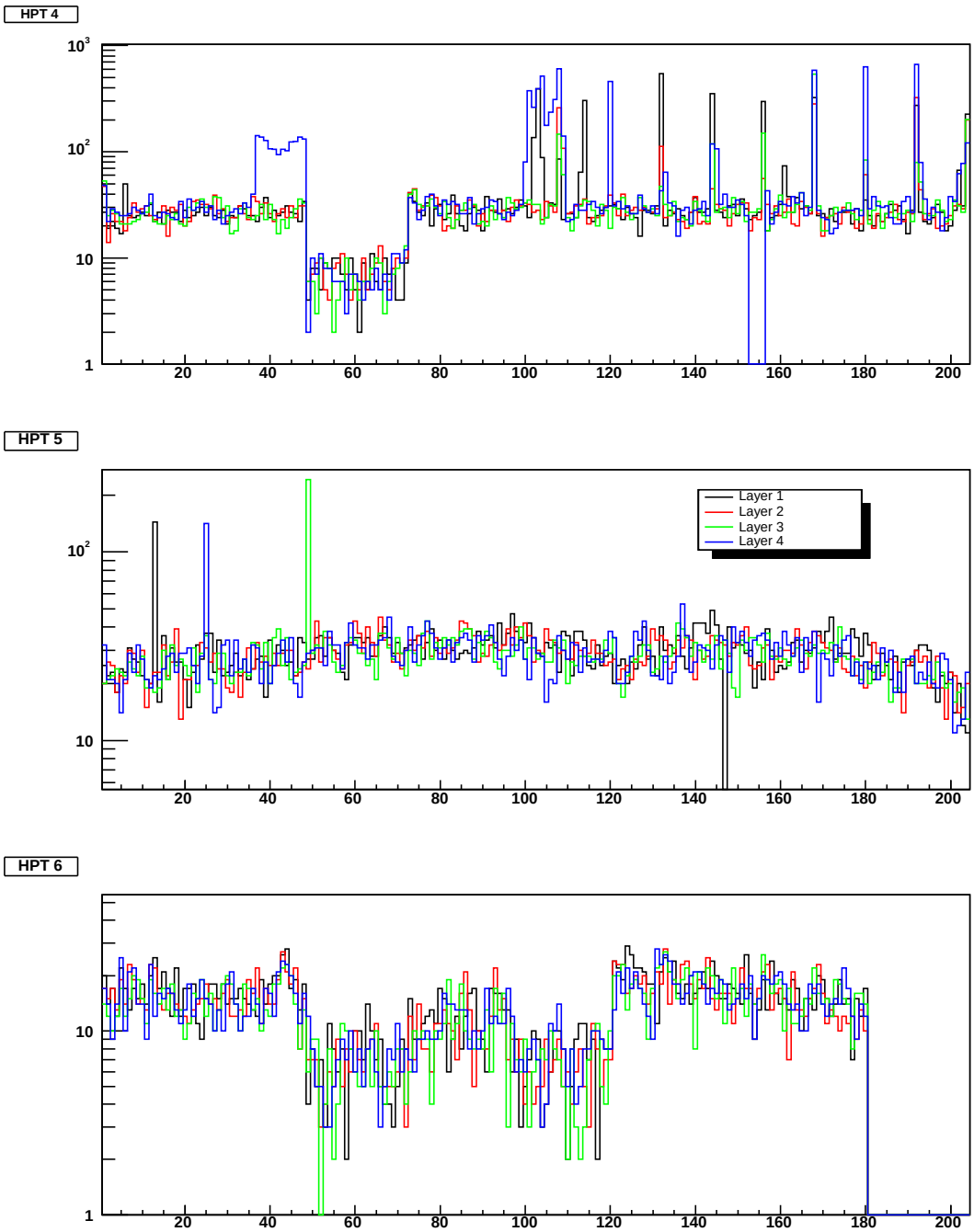

Figure 5.5: Hits per tube for all layers in HPT 4, 5 and 6.

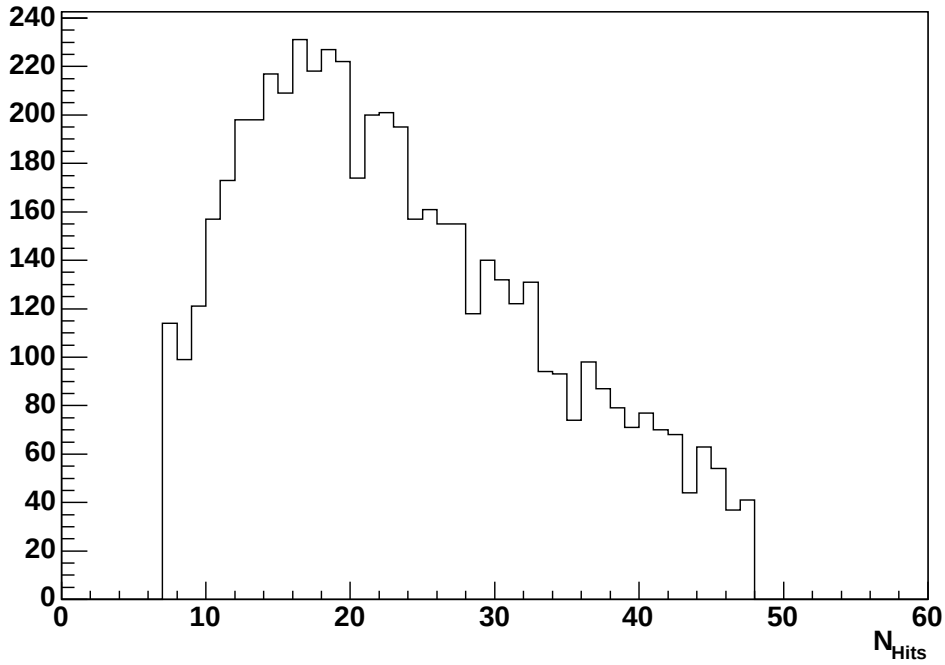

Figure 5.6: Hits per event for cut data.

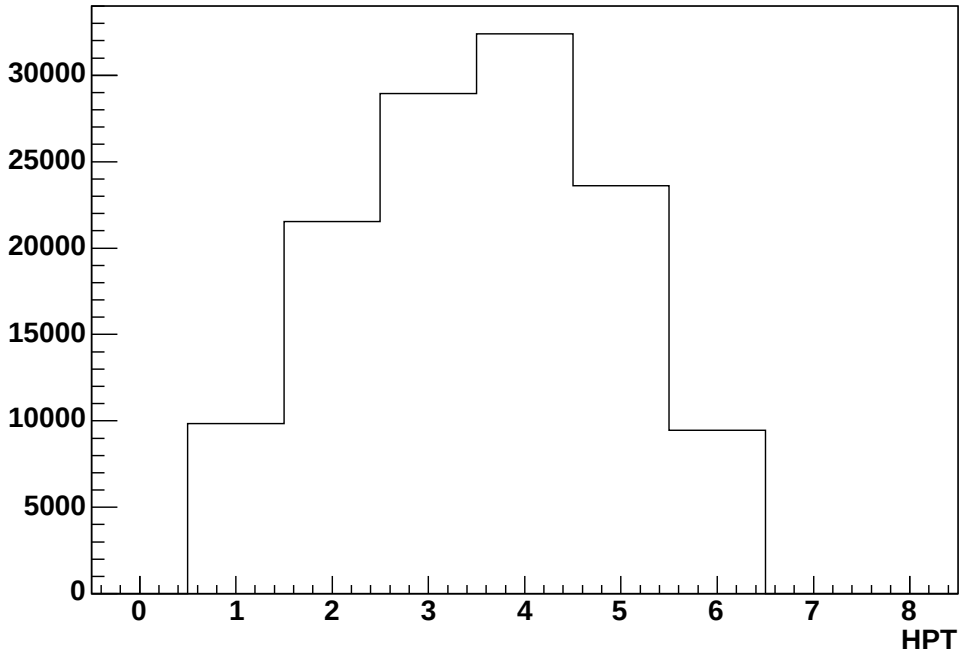

Figure 5.7: Total number of hits per plane for all events after cuts were applied.

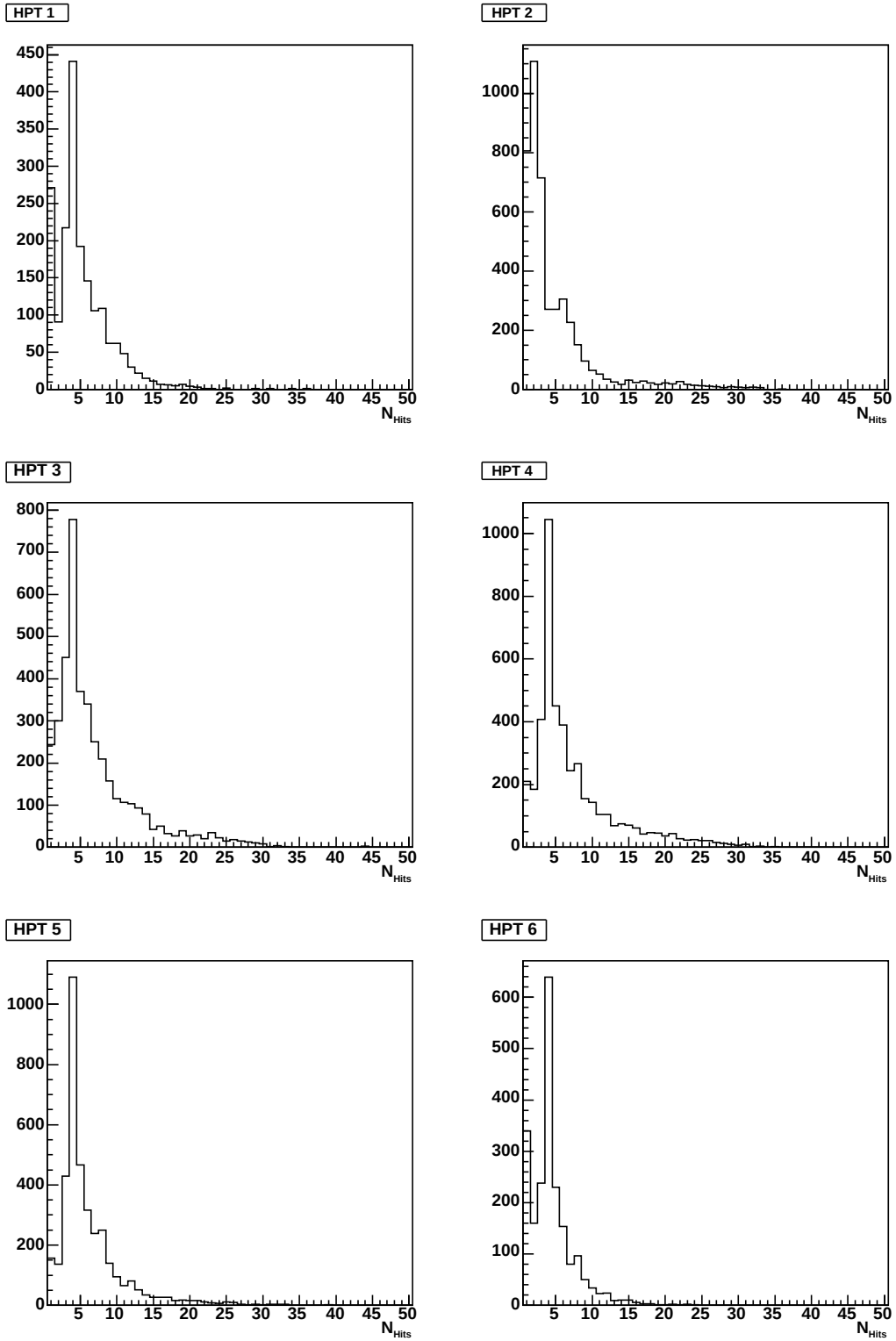

Figure 5.8: Hits per event for all planes.

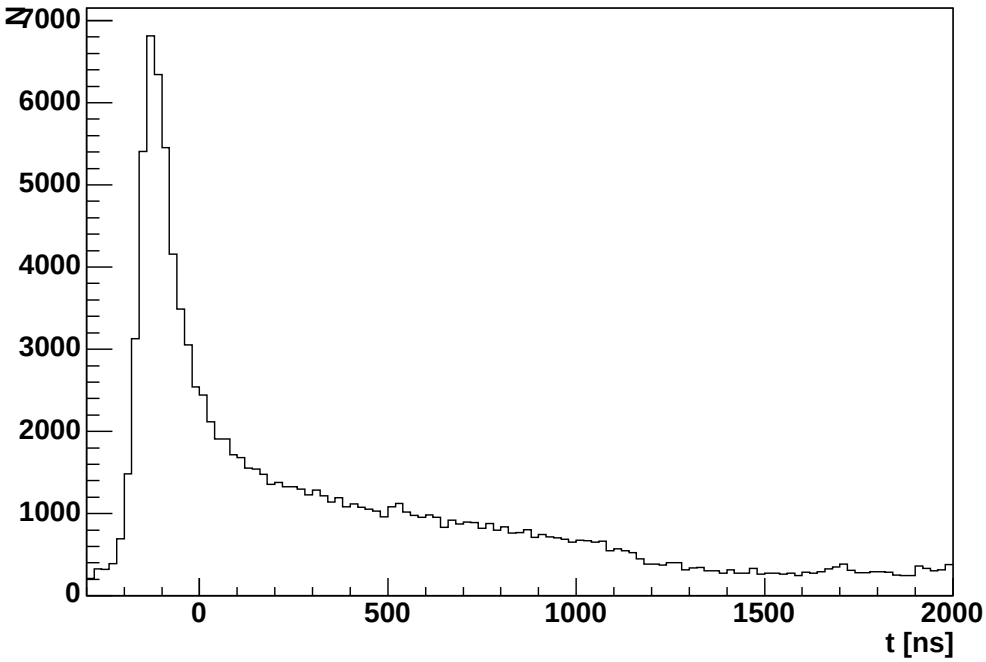

Figure 5.9: Drift time spectrum for real events.

Chapter 6

Beam Localization

In this chapter the possibility of locating the position of the beam axis with respect to the OPERA detector with the precision tracker is studied. At first, general properties of a perfectly focused neutrino beam are derived. Different models for the simulation of the CNGS neutrino energy spectra at different locations towards the beam axis are then presented as well as four methods for generating corresponding CC energy spectra based on the existing event generation package in the OPERA software. Finally, the effects of these different spectra on the precision tracker and its ability to reconstruct them are tested.

6.1 Beam Kinematics

As described in Chapter 3.2, beam neutrinos are mainly generated through the decay of kaons and pions. This decay of a meson with mass m_M into a muon with mass m_μ can be described as a two-body decay in the rest frame of the meson. The center-of-mass energy E_ν^* of the neutrino is then given by

$$E_\nu^* = \frac{m_M^2 - m_\mu^2}{2m_M}. \tag{6.1}$$

In its rest frame, the decay products of the meson are distributed isotropically:

$$\frac{dN_\nu}{d\cos\theta_\nu^*} \equiv \xi = \text{const.}$$

The angle θ_ν of the out-going neutrino in the laboratory frame can be determined through a Lorentz boost. All produced neutrinos will be emitted close to the beam axis, as shown in Figure 6.1. The angle θ_ν in the laboratory frame is given by:

$$\cos\theta_\nu = \frac{\cos\theta_\nu^* + \beta}{1 + \beta\cos\theta_\nu^*} \tag{6.2}$$

with $\beta = \frac{p_M}{E_M}$, p_M and E_M are the meson's momentum and energy respectively. Thus the angular distribution of the out-coming neutrinos is given by:

$$\frac{dN_\nu}{d\cos\theta_\nu} = \frac{dN_\nu}{d\cos\theta_\nu^*} \cdot \frac{d\cos\theta_\nu^*}{d\cos\theta_\nu} = \xi \cdot \frac{d}{d\cos\theta_\nu}\frac{\cos\theta_\nu - \beta}{1 - \beta\cos\theta_\nu} = \xi \cdot \frac{1-\beta^2}{(1-\beta\cos\theta_\nu)^2}. \tag{6.3}$$

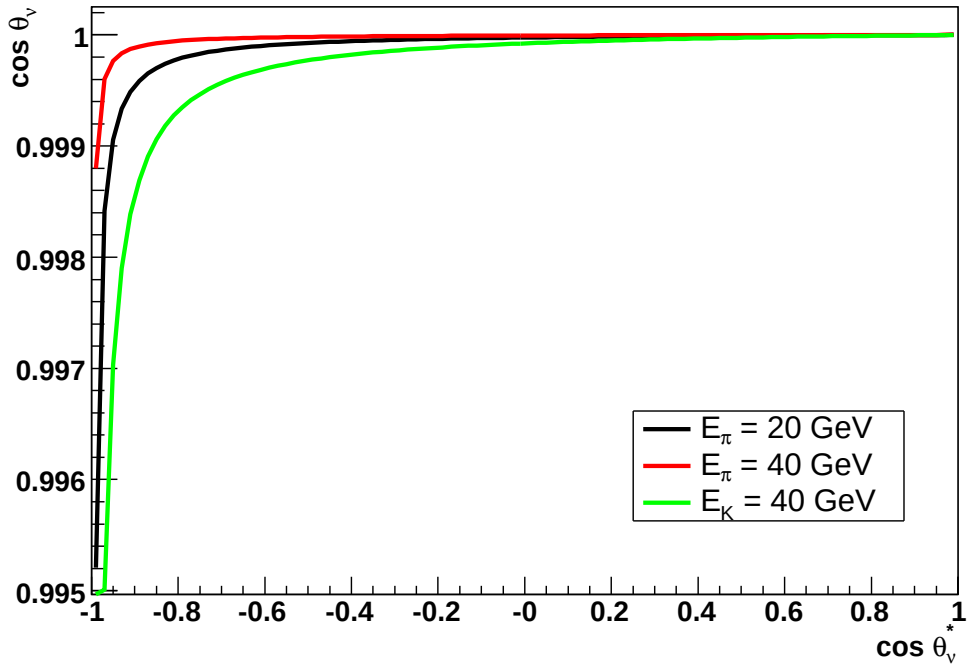

Figure 6.1: Lorentz boost effect on neutrinos from different mesons.

The angular distributions for neutrinos originating from different decays with a given energy are shown in Figure 6.2. To obtain the neutrino's energy in the laboratory frame, one also has to perform a Lorentz boost:

$$E_\nu = \frac{E_M}{m_M} E_\nu^*(1 + \beta \cos\theta_\nu^*).$$

Combining Equations 6.1 and 6.2 one gets

$$E_\nu(\theta_\nu) = \frac{m_M^2 - m_\mu^2}{2(E_M - p_M \cos\theta_\nu)}. \tag{6.4}$$

The neutrino energy thus depends on the angle to the beam axis as shown in Figure 6.3, Figure 6.4 shows the correlation between the parent's and the neutrino's energy for different angles expressed through the correspondent radius of arrival $R = 732\,\mathrm{km} \cdot \tan\theta_\nu$ at Gran Sasso. For neutrinos generated along the beam axis, their energy is approximately proportional to the parent's energy. Neutrinos being emitted off axis have lower energies than those in the center

6.1.1 Off axis beam properties

As seen above, beam neutrinos form a strong forward peak around the beam axis. Nevertheless, most neutrinos are not emitted directly to the center, a fairly large amount will propagate at an angle θ_ν to the beam axis. From the kinematic considerations above, the following beam characteristics suitable for distinguishing different locations from the beam axis can be derived:

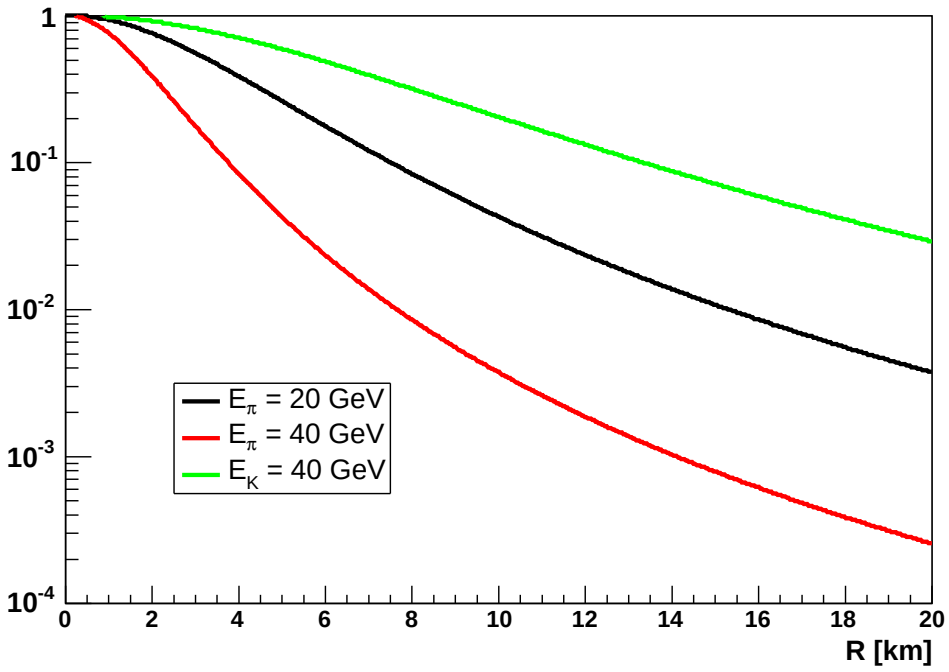

Figure 6.2: Relative distribution of neutrinos from different parent particles for different radii of arrival at Gran Sasso.

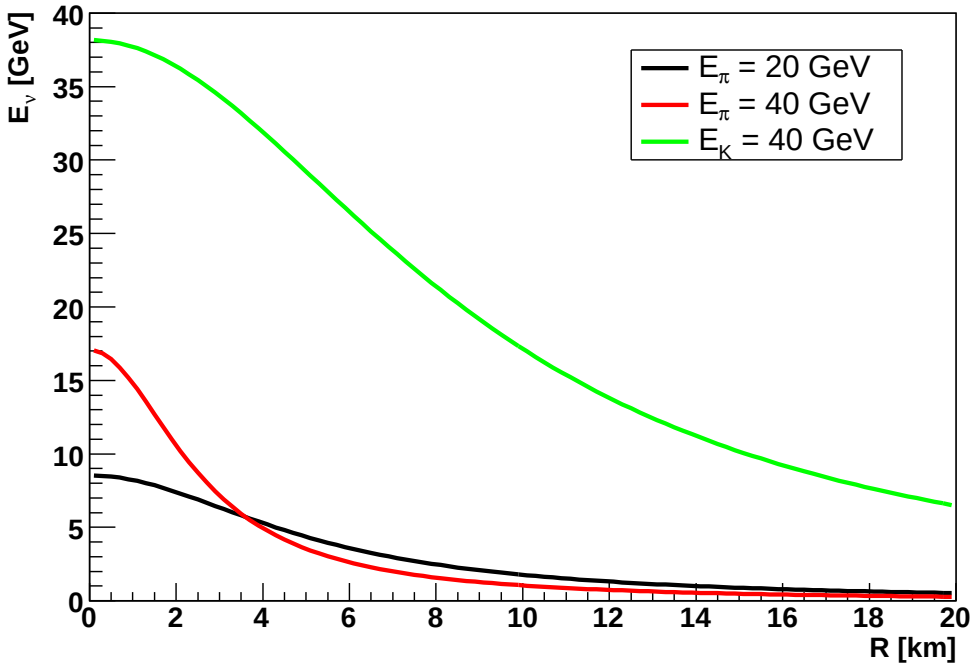

Figure 6.3: Neutrino energy depending on $\cos\theta_\nu$, here expressed in distance R from beam axis at Gran Sasso.

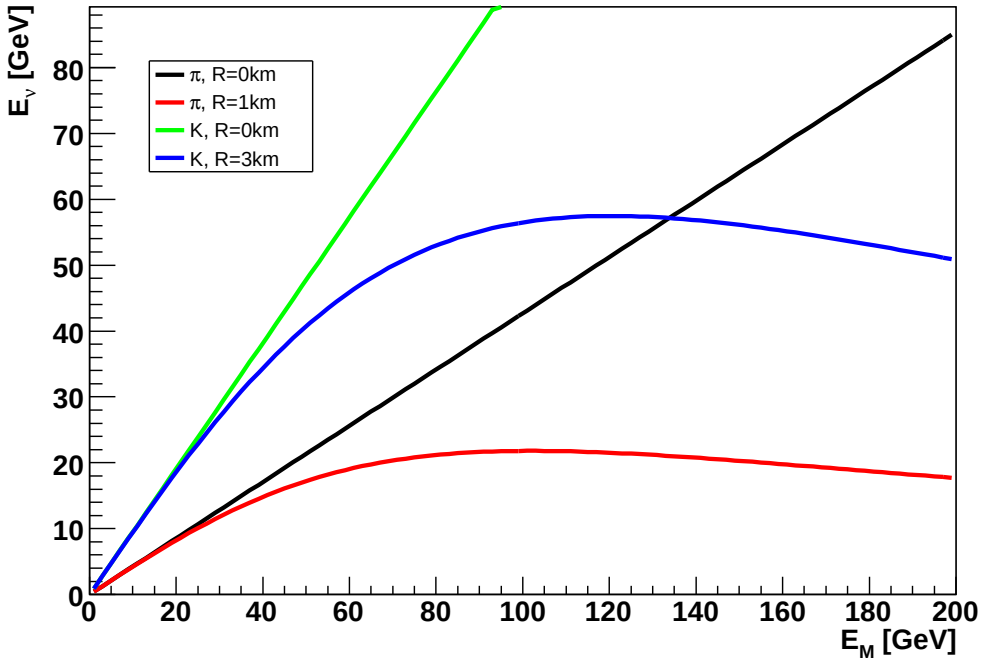

Figure 6.4: Neutrino energy as a function of the energy of the parent for different angles/radii at Gran Sasso.

- The neutrino flux decreases significantly for off axis neutrinos.
- The neutrino energy also decreases significantly for off axis neutrinos.
- While the neutrino energy is proportional to the parent meson's energy for on axis neutrinos, its energy cannot exceed a maximum value $E_\nu^{\max}$ when being emitted off axis.

The last point follows from Equation 6.4. The function has a maximum for $\cos\theta_\nu \neq 0$ at $E_M^{\max}$. The maximum can be determined as follows, using $p_M = \sqrt{E_M^2 - m_M^2}$:

$$\frac{dE_\nu}{dE_M}(E_M^{\max}) = -\frac{m_M^2 - m_\mu^2}{2} \frac{1 - \frac{E_M^{\max}}{\sqrt{(E_M^{\max})^2 - m_M^2}} \cos\theta_\nu}{\left(E_M^{\max} - \sqrt{(E_M^{\max})^2 - m_M^2}\cos\theta_\nu\right)^2} = 0.$$

The expression is zero for

$$\frac{E_M^{\max}}{\sqrt{(E_M^{\max})^2 - m_M^2}} \cos\theta_\nu = 1.$$

From this follows that

$$E_M^{\max} = \frac{m_M}{\sin\theta_\nu}.$$

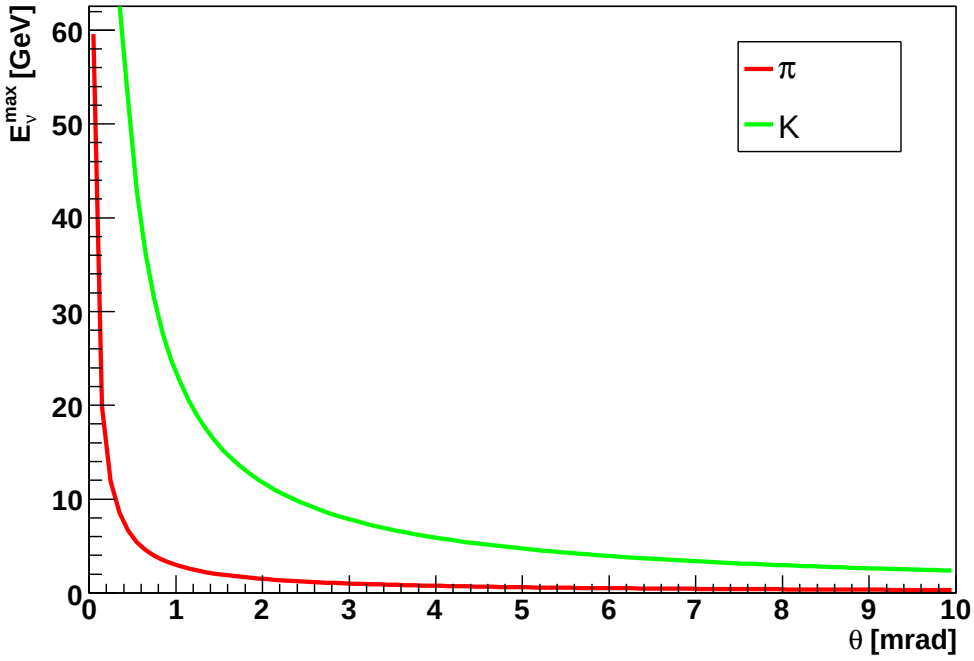

Figure 6.5: Maximum neutrino energy $E_\nu^{\max}$ for neutrinos depending on their angle θ to the beam axis. $E_\nu^{\max}$ is independent of the parent's energy.

This allows to calculate the maximum neutrino energy for a given θ and thus for a certain off axis position R:

$$E_\nu^{\max}(\theta) = \frac{m_M^2 - m_\mu^2}{2\left(\frac{m_M}{\sin\theta} - \sqrt{\frac{m_M^2}{\sin^2\theta} - m_M^2}\cos\theta\right)} = \frac{m_M^2 - m_\mu^2}{2m_M \sin\theta}.$$

The maximum neutrino energy for neutrinos originating from both pions and kaons is shown in Figure 6.5. While the first two characteristics still require some knowledge about the energy spectrum of the decaying mesons, the third property provides a method of identifying the off axis location from the neutrino energy distribution independent of further details of the parents. The only requirement for the mesons is to reach $E_M^{\max}$.

6.2 Generating Off Axis Beam Data based on Op-Negn

In this section different possibilities to modify the CC energy spectrum generated by the OPERA software are shown. First, a "general" method for modification is described. In the "far"-method, a shift of the beam axis of a few hundreds of meters is done, whereas in the "near"-method the axis is shifted only within 400 m of the center. Finally, an alternative method for the far scenario is tested in the "extended" method.

6.2.1 "General" Method

The neutrino generation package included in the OPERA software is capable of generating neutrino interactions on axis. The package OpNegn generates a list of secondary particles from either NC or CC interactions or quasi elastic scattering of a given neutrino type with nuclei. As input, OpNegn uses neutrinos with an energy spectrum based on FLUKA simulations. OpNegn provides information on the energy $E_\nu^{\mathrm{CC/NC/qel}}$ of the reacting neutrino, but not on its history. Also, only interacting neutrinos are generated so that no information on the initial arriving neutrino flux is given. The E_ν^{CC} spectrum for 50 000 OpNegn ν_μ events is shown in Figure 6.6. CC interactions are the dominating process at Gran Sasso so the following studies have been done with this CC set of data.

To obtain a list of secondary particles from off axis interactions at a certain position R from the beam center, the neutrino E_ν^{CC} spectra for both on axis and at a corresponding angle θ_ν have to be known. The list of interactions for different θ_ν can then be obtained from the original spectrum as follows:

- For each energy E_ν^{CC} a relative distribution $P(E_\nu, \theta_\nu) = \frac{N^{\mathrm{CC}}(E_\nu(\theta_\nu))}{N^{\mathrm{CC}}(E_\nu(0))}$ has to be determined. $N^{\mathrm{CC}}(E_\nu(\theta_\nu))$ is the number of CC reacting neutrinos in a certain energy range for a fixed value of pot.

- The resulting distribution has to be normalized to the content $N_{\max}$ of the maximal bin to obtain a probability distribution. This eventually leads to a reduction in the simulated off axis beam flux but is necessary to prevent probabilities to exceed 1. The normalization factor (which is the content of the maximum bin) has to be recorded for future corrections.

- For each OpNegn event the energy E_ν of the incoming neutrinos has to be determined from the data. An event will be added to the modified neutrino spectrum for a fixed value of θ_ν with the probability $\frac{P(E_\nu)}{N_{\max}}$.

As mentioned above, this method depends on the knowledge of the neutrino CC fluxes for both on axis and the off axis location of which only the first is provided by OpNegn.

An analytical attempt to shift the E_ν^{CC} spectrum without knowledge of the incoming neutrino flux proved to be unsuccessful: As shown in Section 6.1, the energy of a beam neutrino depends on the parent's mass, energy and the angle to the beam axis. A first attempt was to calculate the energy of the decaying parent for each CC reacting neutrino under the assumption of $\theta_\nu = 0$ and then recalculate the neutrino's energy for a different angle. This fails mainly for two reasons:

- There is no information on the parent's identity and therefore the mesons energy cannot be calculated accurately.

- The cross section for neutrino CC interactions is energy dependent. An event from the OpNegn data occurs with another cross section when the neutrino is emitted at another angle and thus with another energy.

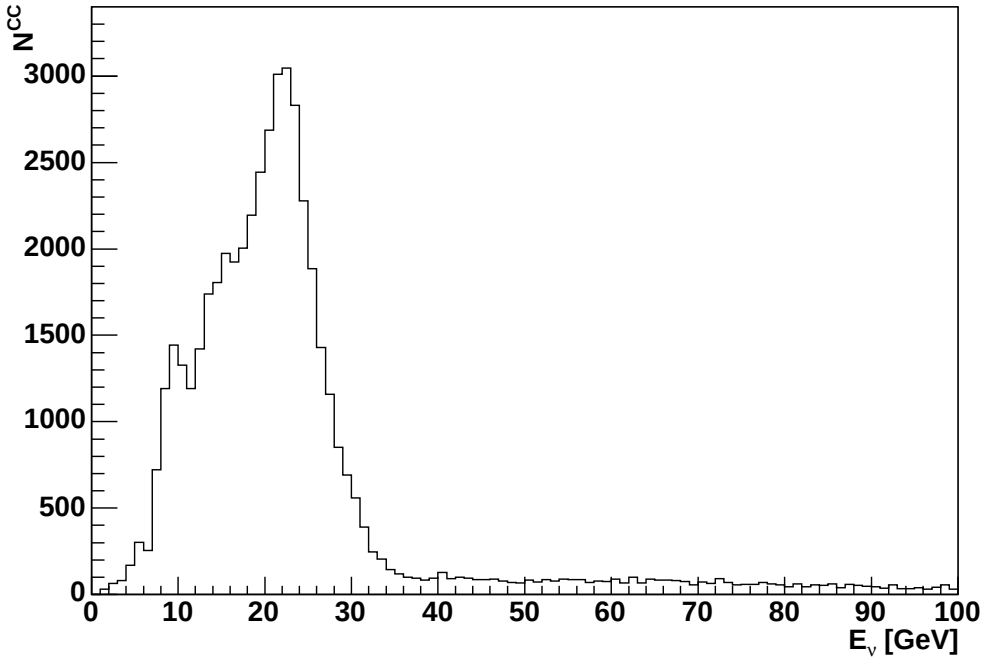

Figure 6.6: Energy spectrum of neutrinos generating a CC reaction. A total of 50 000 events was analyzed. The data was created with the OpNegn simulation tool.

6.3 FLUKA Simulations

As mentioned before, OpNegn uses data from FLUKA simulations as a basis. For further attempts to gain off axis CC energy spectra, n-tuples of simulated CNGS neutrino fluxes provided by the Milano section of the INFN [69] have been used. The original FLUKA data provides a range of information for each neutrino, including among others the energy and radius of arrival at Gran Sasso as well as the identity of the decaying parent, its energy and direction. The ν_μ flux at Gran Sasso is shown in Figure 6.7. The red and green histograms distinguish between the neutrino producing parent particles. The neutrinos are mainly produced by pions. Only for higher energies, production from kaons dominates. With the FLUKA information on both the parents id and the total flux, analytical determination of the CC energy spectrum for off axis locations based on the OpNegn data now becomes more feasible.

6.3.1 "Far" Method

- A probability distribution for a neutrino with energy E_ν to come from a pion has been derived from FLUKA data and is shown in Figure 6.8. The probability was determined as $P = \frac{N_\pi}{N_\pi + N_K}$. One can clearly see the dominating process of pion decays for smaller energies.

- For each generated event from OpNegn it is decided according to this distribution, whether the parent was a pion or kaon. The corresponding energy E_M for the

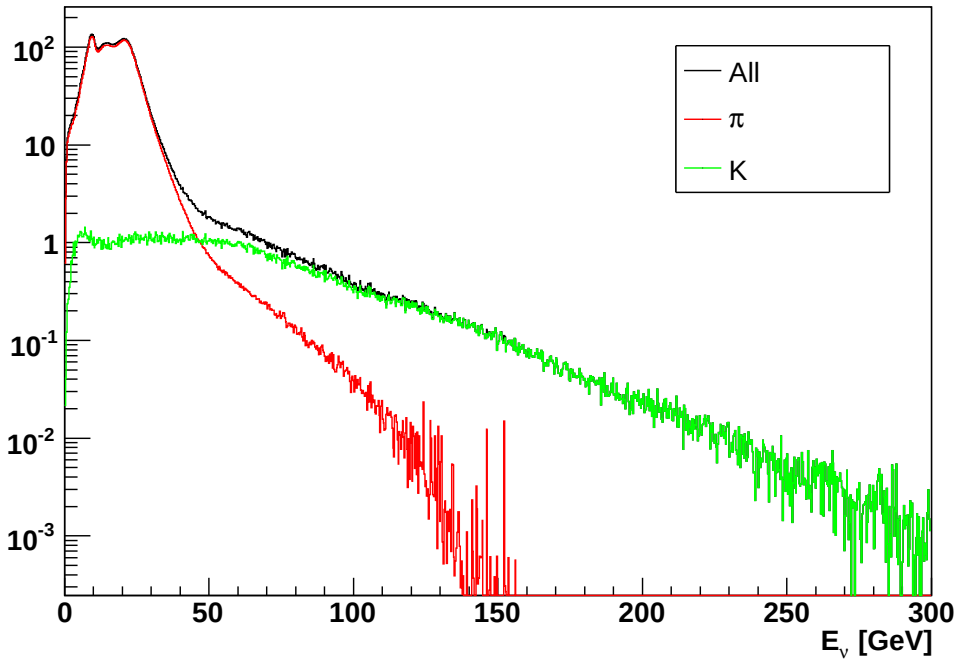

Figure 6.7: Neutrino energy spectrum taken from FLUKA simulations.

decaying meson is calculated. E_M can be derived from Equation 6.4 assuming $\theta_\nu = 0$:

$$E_M = \frac{m_M^2 - m_\mu^2}{4E_\nu} + \frac{m_M^2 E_\nu}{m_M^2 - m_\mu^2}.$$

- The neutrino energy E'_ν is then recalculated for a different angle θ_ν.
- In order to consider the energy dependence of the ν_μ CC cross section, the event has to be weighted by the factor $\frac{N^{\mathrm{FLUKA}}(E_\nu)}{N^{\mathrm{CC}}(E_\nu)} \cdot \frac{N^{\mathrm{CC}}(E'_\nu)}{N^{\mathrm{FLUKA}}(E'_\nu)}$.
- To account for the decreasing flux for off axis neutrinos described in Equation 6.3 a factor of $\frac{(1-\beta)^2}{(1-\beta\cos\theta_\nu)^2}$ has to be added when calculating absolute fluxes.
- When determining absolute fluxes, one more weight has to be considered. For simplicity a round detector is assumed. For locations at larger distances d from the beam center, a detector with diameter r covers a smaller part of the area of the annulus $A = \pi((d-r)^2 - (d+r)^2)$. This can be included through a factor $\frac{r}{4d}$ for $d \geq r$ and $\left(\frac{r}{r+d}\right)^2$ for $d < r$.

The CC energy spectrum shown in Figure 6.6 has been modified by this method. The resulting spectra for different off axis locations are shown in Figure 6.10. Figure 6.9 shows a comparison between the different off axis spectra to the one on axis. One can clearly recognize the cut off energy described in Section 6.1.1. Also, the described decrease in flux can be noticed. The total number of events comparing to 50 000 events in the center are shown in Table 6.1.

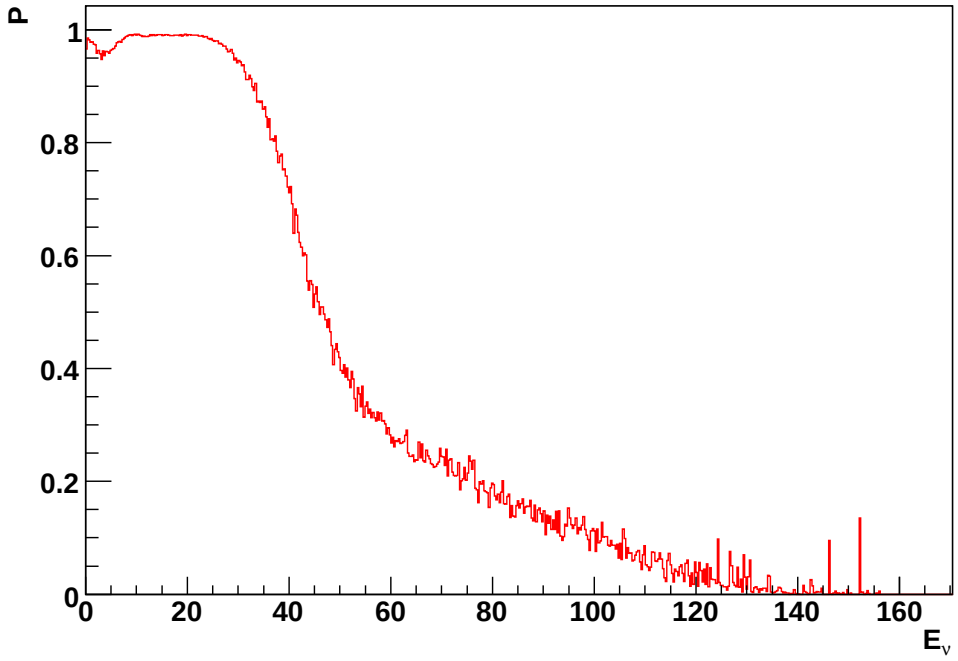

Figure 6.8: Probability for an on axis neutrino with energy E_ν to come from a decay of a pion.

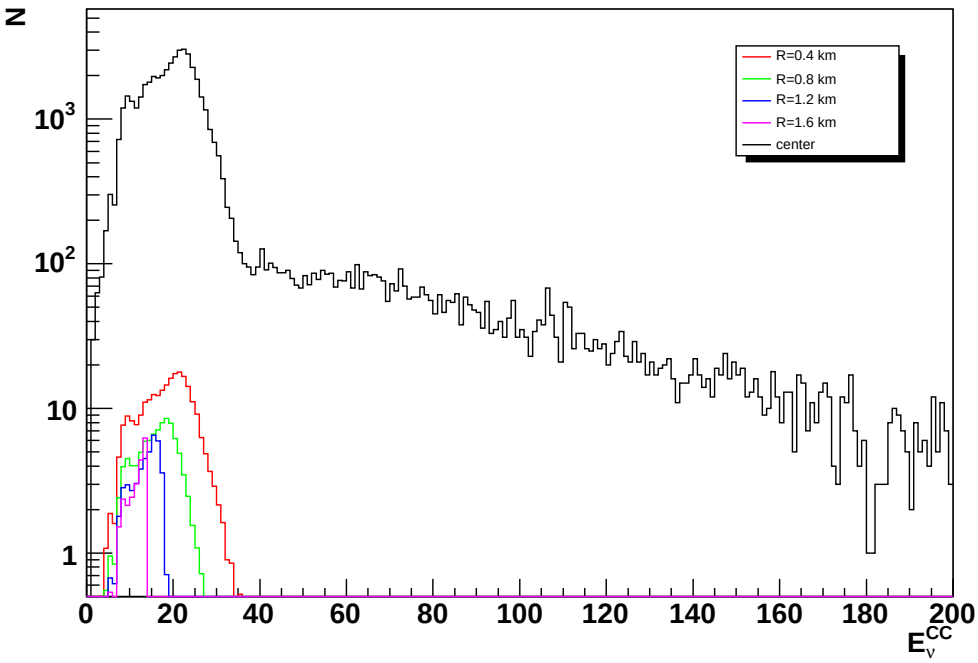

Figure 6.9: Overview of the transformed CC energy spectra.

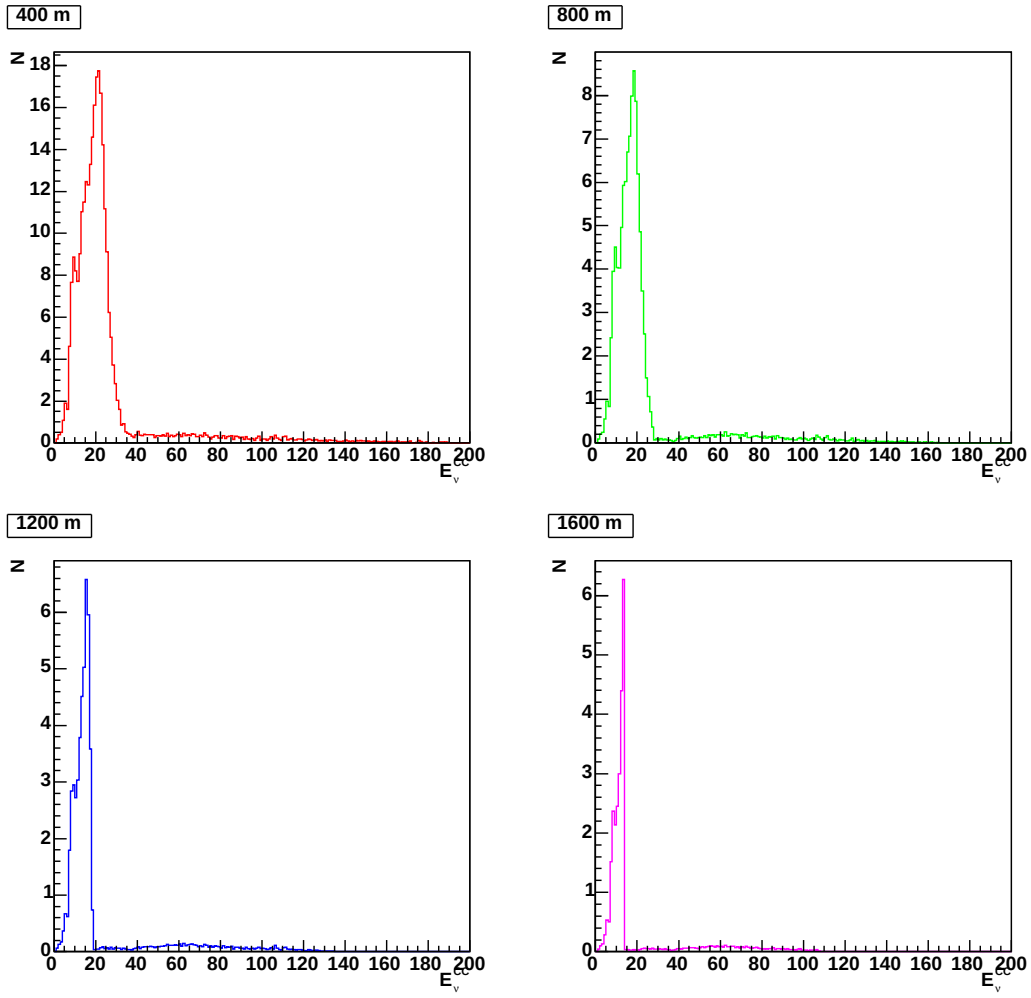

Figure 6.10: Transformed CC energy spectra.

Distance d	Number of events
400 m	284
800 m	111
1200 m	53
1600 m	29

Table 6.1: Number of events for "far" scenarios compared to 50 000 events in the center.

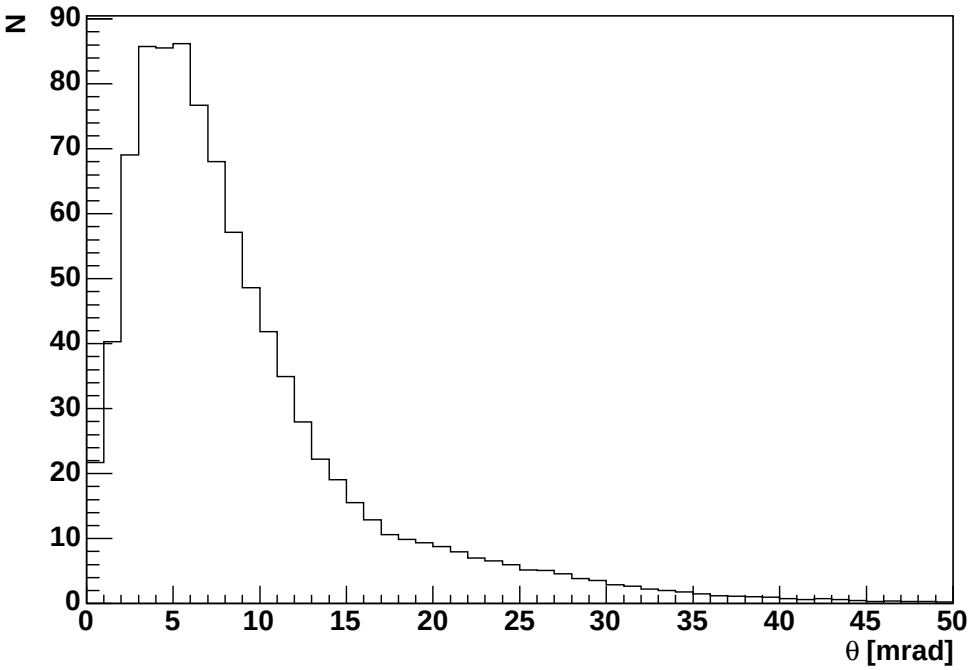

Figure 6.11: Angle θ of the parent mesons to the beam line.

6.3.2 An Attempt to Extend the Simulated FLUKA Beam Spectrum

The method described in the previous chapter has one decisive uncertainty: It is assumed that the primary beam of all parents is perfectly focused. Analyzing FLUKA simulations shows that this is not the case. The FLUKA data provides information on the direction of the decaying meson and thus the angle to the nominal beam line can be derived, as is shown in Figure 6.11. The CNGS beam is a Wide Band Beam (WBB) meaning that no selection on the momentum of the decaying mesons is done. The two magnetic horns are designed to focus 35 GeV and 50 GeV secondary particles [70]. The other mesons emerge at a small angle towards the beam axis. This of course leads to a change of the idealized energy spectrum. The effect can clearly be seen in Figure 6.12 where the neutrino energy versus the parent energy is shown for FLUKA simulations. For most neutrinos, the theoretical on axis energy is reached. There is, however, still a large amount of neutrinos with a lower energy, meaning that the neutrino has emerged at some angle $\theta_\nu \neq 0$ towards the direction of the meson.

Figure 6.13 shows the number of neutrinos depending on the radius of arrival at Gran Sasso which is also provided in the FLUKA data. The number increases for higher radii. This can be easily explained - for a larger radius R the surface element $dA = 2\pi R dR$ also increases. There is a sudden cut off at 400 m because the simulation only provides data within this radius.

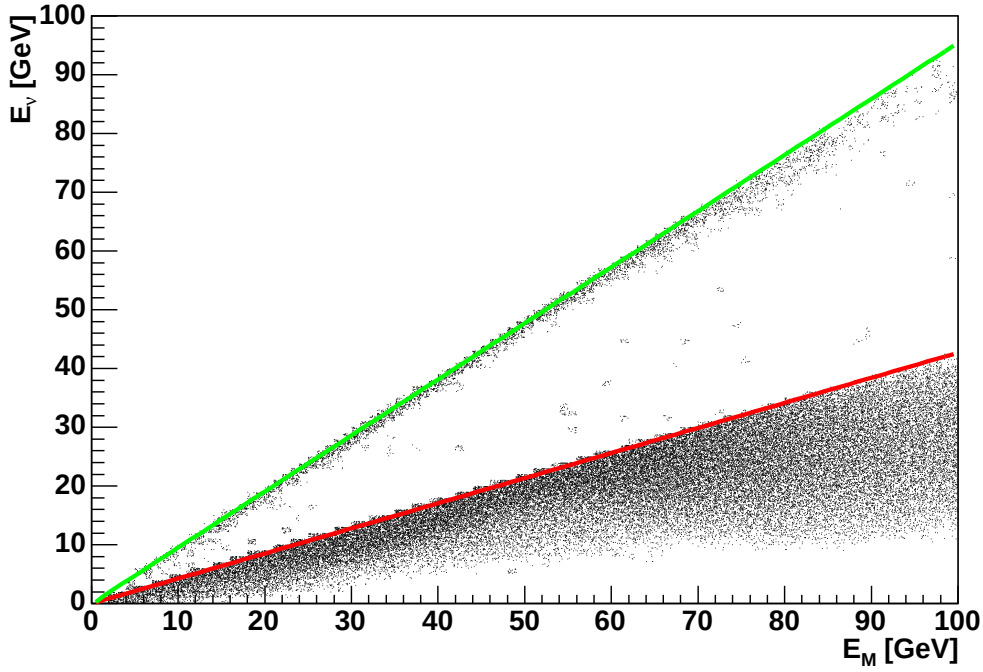

Figure 6.12: Neutrino energy at Gran Sasso vs. the parent energy from FLUKA simulations. The red and green line show the theoretical value for perfect focusing for pions and kaons respectively. The number of entries is plotted logarithmically.

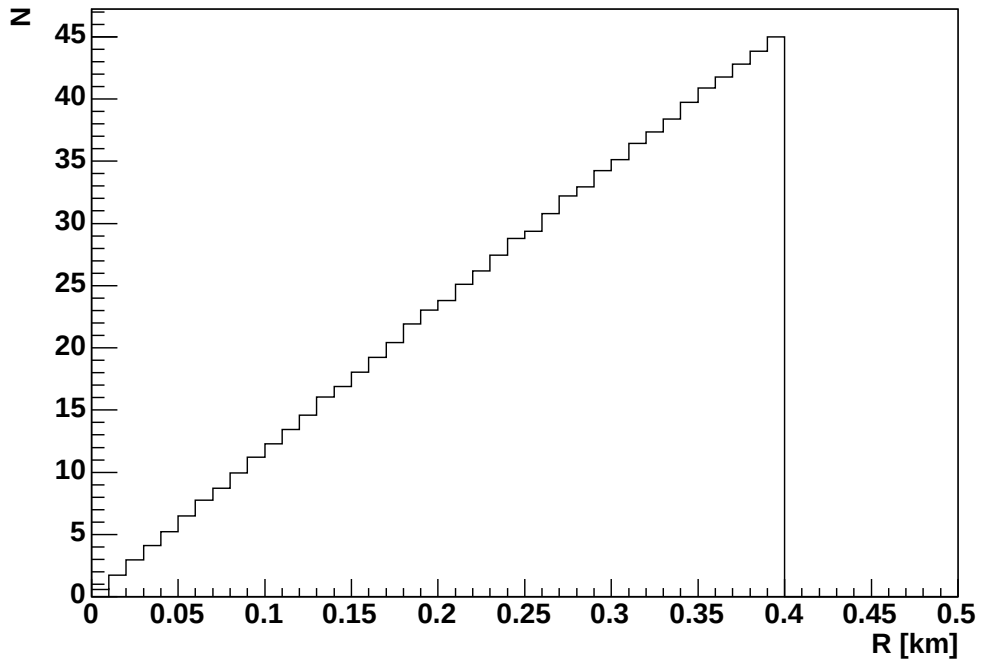

Figure 6.13: Distribution of radii of arrival at Gran Sasso for neutrinos from FLUKA simulations.

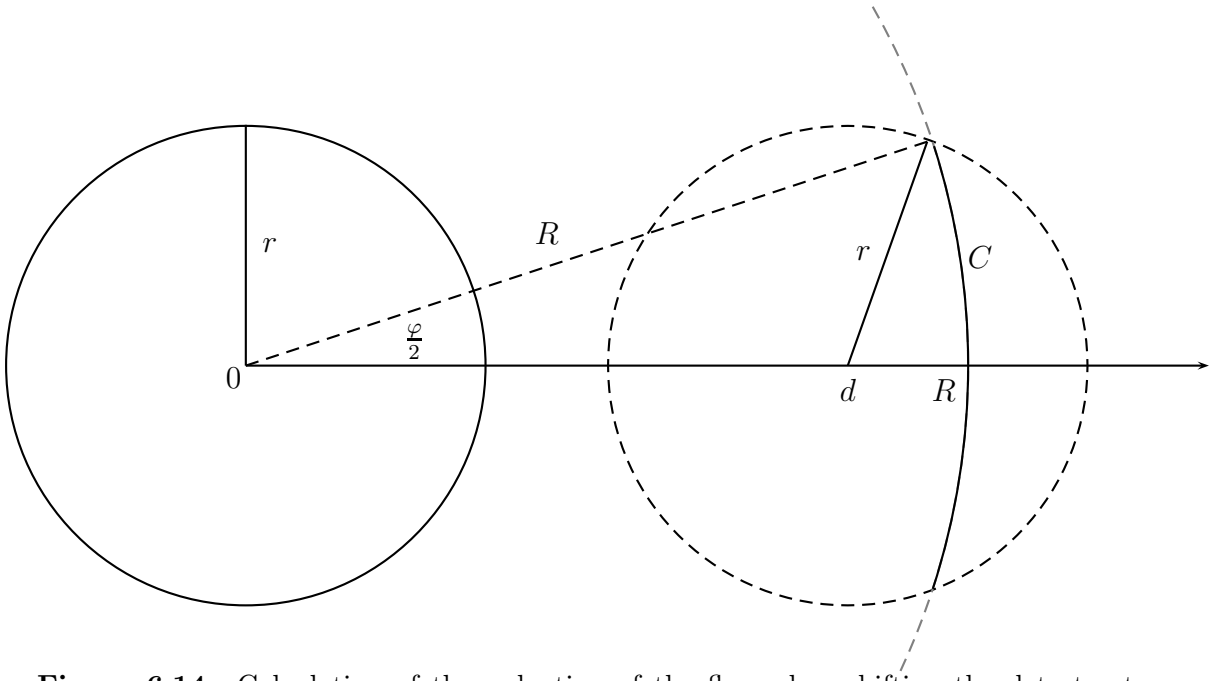

Figure 6.14: Calculation of the reduction of the flux when shifting the detector to a distance d from the beam center.

6.3.3 Beam Spectra close to Axis, the "Near" Method

Figure 6.15 shows the fluxes for different locations within the beam. The energy spectrum is approximately equal for different radii. The first histogram shows the flux for the center, all neutrinos arriving within a radius $R < r = 50\,\mathrm{m}$ are recorded. The other spectra shown are those at distances $d = 100\,\mathrm{m}$ $d = 200\,\mathrm{m}$ and $d = 300\,\mathrm{m}$ from the center. A correction for the surface element had been done: to obtain comparable data, only neutrinos going through the same area $A = \pi r^2$ as the reference beam in the center were chosen. For this, each neutrino arriving at a radius R where $d - r < R < d + r$ was biased. The weight was determined similar to the correction described in the "far" method, but in a more precise way, as shown in Figure 6.14. For a neutrino arriving at radius R the probability P to lie within A is $\frac{C \cdot dR}{2\pi R \cdot dR} = \frac{\varphi(R,d)}{2\pi}$. The angle φ can be determined through $r^2 = d^2 + R^2 - 2Rd\cos\frac{\varphi}{2}$. This leads to:

$$P(R,d) = \frac{C \cdot dR}{2\pi R \cdot dR} = \frac{1}{\pi}\cos^{-1}\left(\frac{r^2 - R^2 - d^2}{-2Rd}\right).$$

For each CC energy spectrum outside the center, a correlation $P'(E_\nu) = \frac{N(\theta)}{N(0)}$ to the beam on axis has been made and is shown in the left histograms in Figure 6.16. For small energies, this distribution is almost equal to 1. For larger energies, clear fluctuations can be noticed which can be explained by the small number of events in this energy range. These correlations provide a probability distribution $P'(E_\nu)$ for transforming the OpNegn E_ν^{CC} spectrum into an off axis spectrum. For each energy E_ν the value of the off axis CC

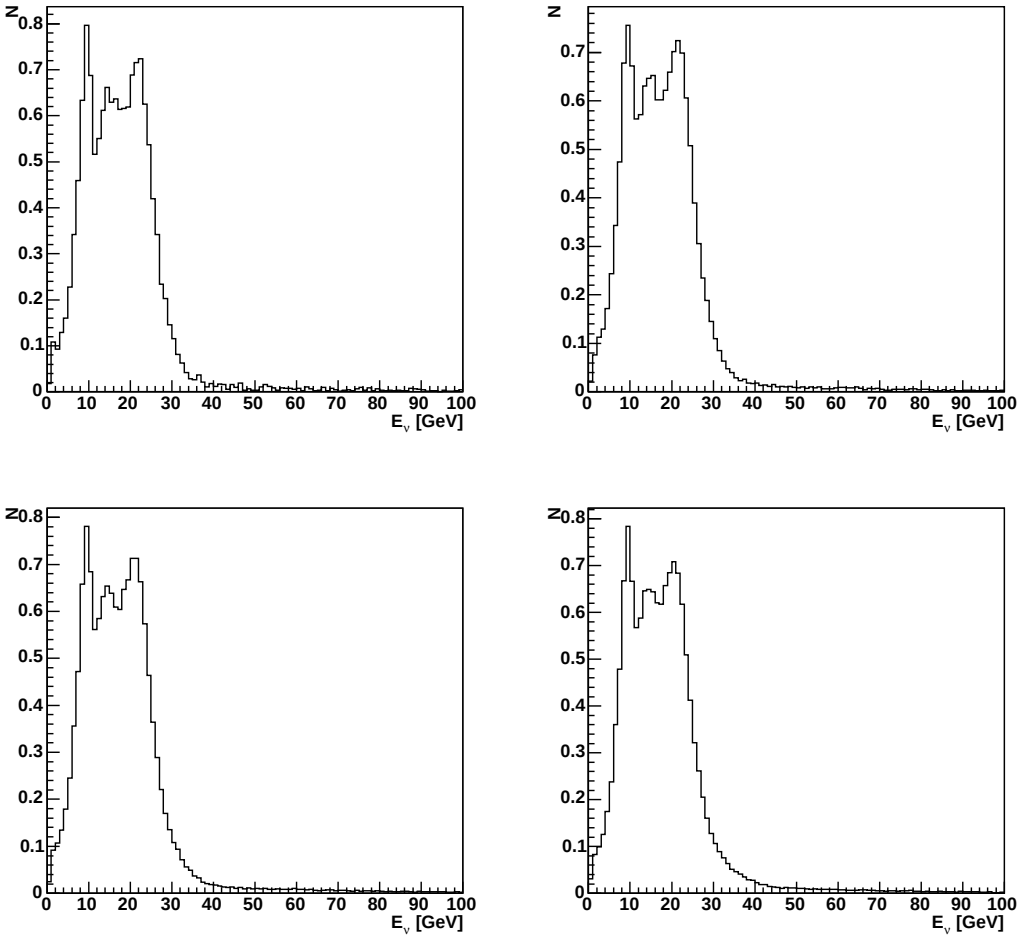

Figure 6.15: Neutrino fluxes for different locations within the nominal beam determined as described in the "near"-method. N is given in arbitrary units. The first histogram corresponds to the beam in the center. The flux was analyzed for a circle with a diameter of 100 m. The other histograms show comparable fluxes for distances of d = 100, 200 and 300 m respectively. The fluxes have been corrected by the method described in the text. No significant change of flux is found for different locations within the nominal 800 m diameter of the beam.

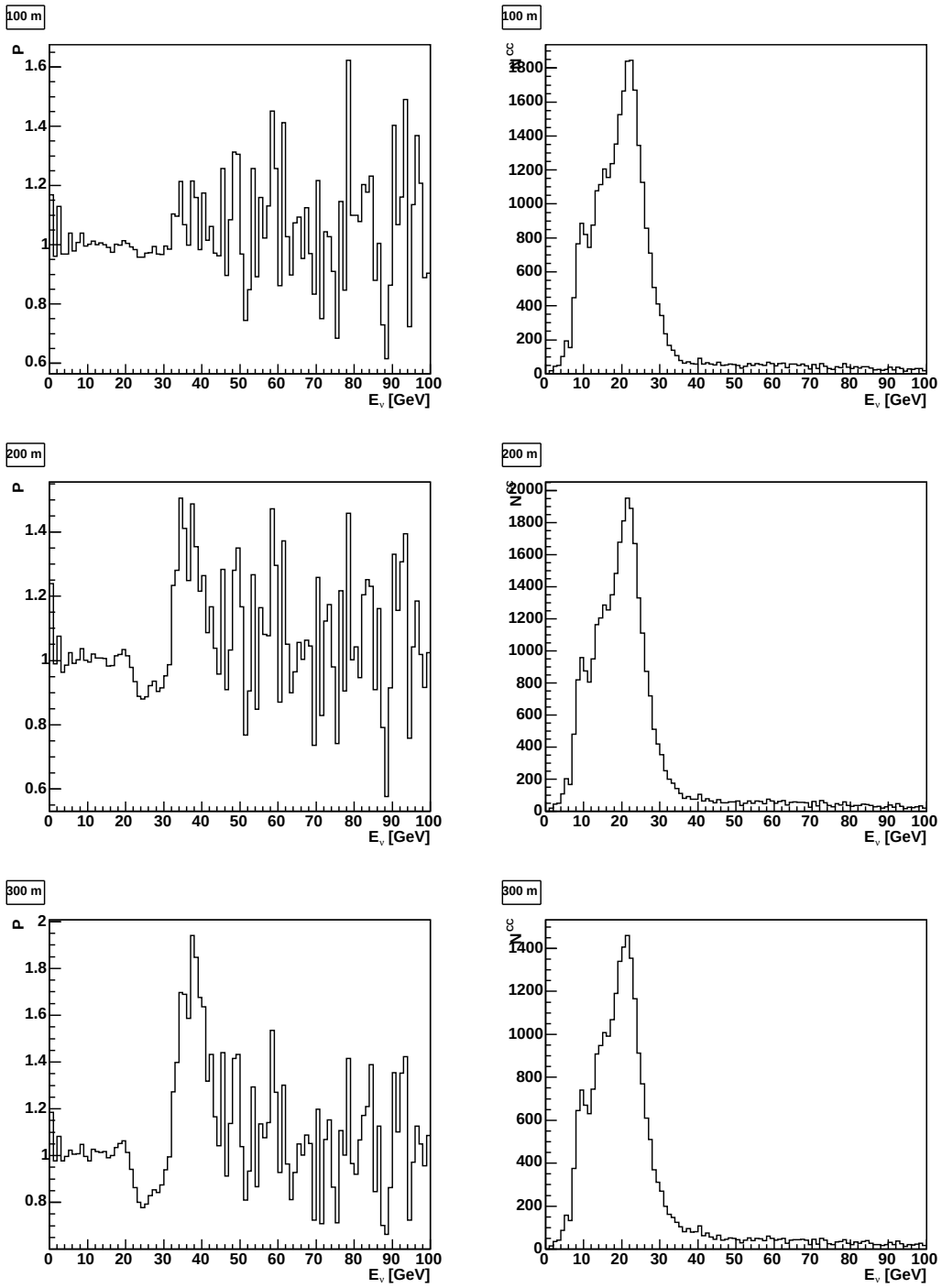

Figure 6.16: Left: probability histograms for different radii within the beam determined with the "near"-method. Right: Resulting modified CC energy spectra off the beam axis.

spectrum can be derived from the one in the center as:

$$N^{\mathrm{CC}}(\theta) = \frac{N(\theta)}{N(0)} \cdot N^{\mathrm{CC}}(0).$$

So determining $\frac{N(\theta)}{N(0)}$ provides a relative distribution of the kind required in the "general" method. In order for probabilities not to exceed 1, a correction factor has to be applied, for which the most simple choice is the content of the maximum bin. Correction factors are summarized in Table 6.2. Similar to the methods used above, each OpNegn event is now examined for the neutrino's energy E_ν^{CC} but also for its radius of arrival R. It is then added to the transformed spectrum with the probability $P'(E_\nu) \cdot P(R, d)$. The transformed energy distributions within the beam are shown on the right side in Figure 6.16.

6.3.4 Shifting the Beam - the "Extended" Method

The existing FLUKA simulations supply neutrinos arriving at Gran Sasso within a radius of 400 m from the beam center. To study the effects of beam pointing errors exceeding 400 m, the spectrum outside this range has to be known. The "far"-method provides one possibility to obtain this data but has the flaw of assuming *perfect* focusing. In order to prevent new complex simulations, an attempt to modify the existing data for an off beam scenario has been made within this thesis and is here introduced.

Assuming once more perfect focusing, one can try to determine the radius dependent spectrum in yet another way. From Equation 6.4 follows that

$$\cos\theta_\nu = \frac{1}{\beta} - \frac{m_M^2 - m_\mu^2}{2E_\nu E_M \beta}.$$

Knowing both the energy of the neutrino and the properties of the parent meson, one can determine the angle θ_ν and thus the radius of arrival R at Gran Sasso. These radii exceed the 400 m of the FLUKA simulations by far, as shown in Figure 6.17. Similar to the "near"-method, all events within $d - r < R < d + r$ have been added to a modified spectrum, again weighted according to the methods described above. The resulting spectra are shown in 6.18 for different distances d. They vary significantly from each other and would provide a fairly good method to determine the detector location in the beam. Unfortunately life is not that simple. As mentioned above, good focusing of the secondary mesons with the magnetic horns is only achieved for a certain energy range and thus the spectra only relate to the direction towards the decay parents' axis. Otherwise the data would also contradict the radius of arrival distribution mentioned earlier.

Extending the FLUKA data

The angle θ_M between the beam line and the direction of the decaying meson corresponds to a distance $a = 732\,\mathrm{km} \cdot \tan\theta_M$ at Gran Sasso. Knowing both θ_M and the energy of the decaying meson, on can calculate the relative probability for the neutrino to be emitted to arrive at a given Radius R' at Gran Sasso.

To derive the neutrino flux outside the beam center, the following attempt has been made:

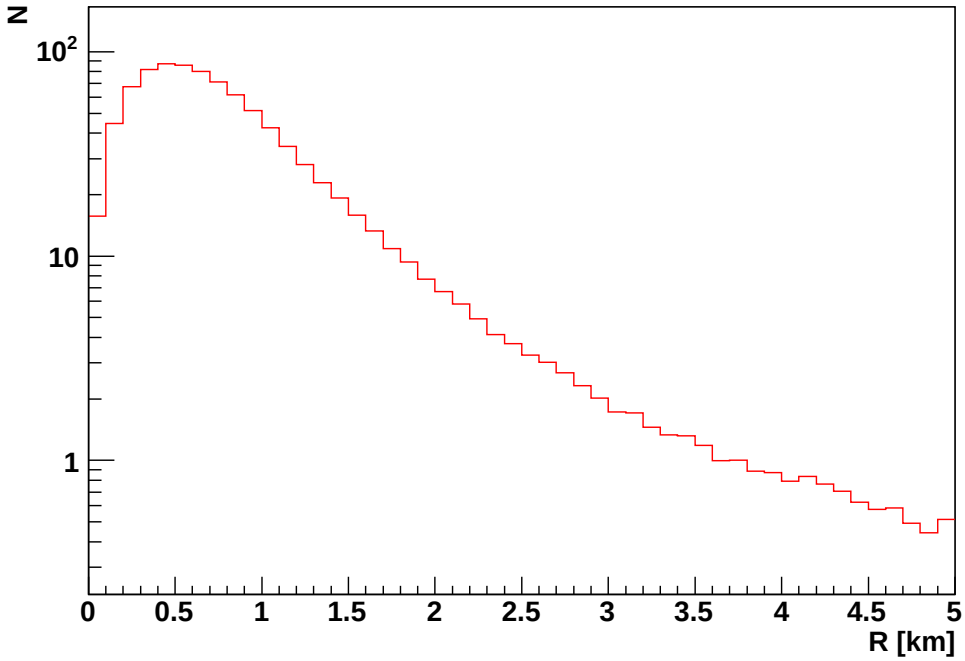

Figure 6.17: Angles between direction of the decaying mesons and the emitted neutrinos.

- Each neutrino originally arriving at any $R < r$ (where r is the diameter of the FLUKA simulated beam at Gran Sasso) will be shifted to R'.
- For each event, the angle θ_M between the decaying meson's trajectory and the beam line was determined from FLUKA data.
- There are different possible angles θ'_ν for the neutrino to arrive at a radius R' at Gran Sasso depending on the angle φ. According to Figure 6.19, the neutrino energy $E'_{\nu,i}$ was calculated for N different values of φ_i. The value of b'_i is given through $b'_i = \sqrt{a^2 + R'^2 - 2aR\cos\varphi_i}$, whereas $a = 732\,\mathrm{km} \cdot \tan\theta_M$. The neutrino energy can then be calculated with Equation 6.4 and $\cos\theta'_\nu = \cos\left(\tan^{-1}\left(\frac{b'}{732\,\mathrm{km}}\right)\right)$.
- Following from Equation 6.3, the probability for a neutrino to be emitted at an angle θ'_ν varies. For each value $E'_\nu(\varphi_i)$ a relative weight P to the original FLUKA event is therefore calculated. Using Equation 6.3 and then 6.4 one gets:

$$P = \frac{(1-\beta\cos\theta_\nu)^2}{(1-\beta\cos\theta'_\nu)^2} = \left(\frac{E'_\nu(\varphi_i)}{E_\nu}\right)^2.$$

- Finally, each energy value $E'_\nu(\varphi_i)$ is added to the modified neutrino spectrum with a weight $\frac{P}{N}$.

Beam spectra for different distances d of the detector from the beam center have been created as described above. To gain comparable data to the reference spectrum, a radius of $r = 400\,\mathrm{m}$ has been chosen. For this, each original event has been recalculated for a

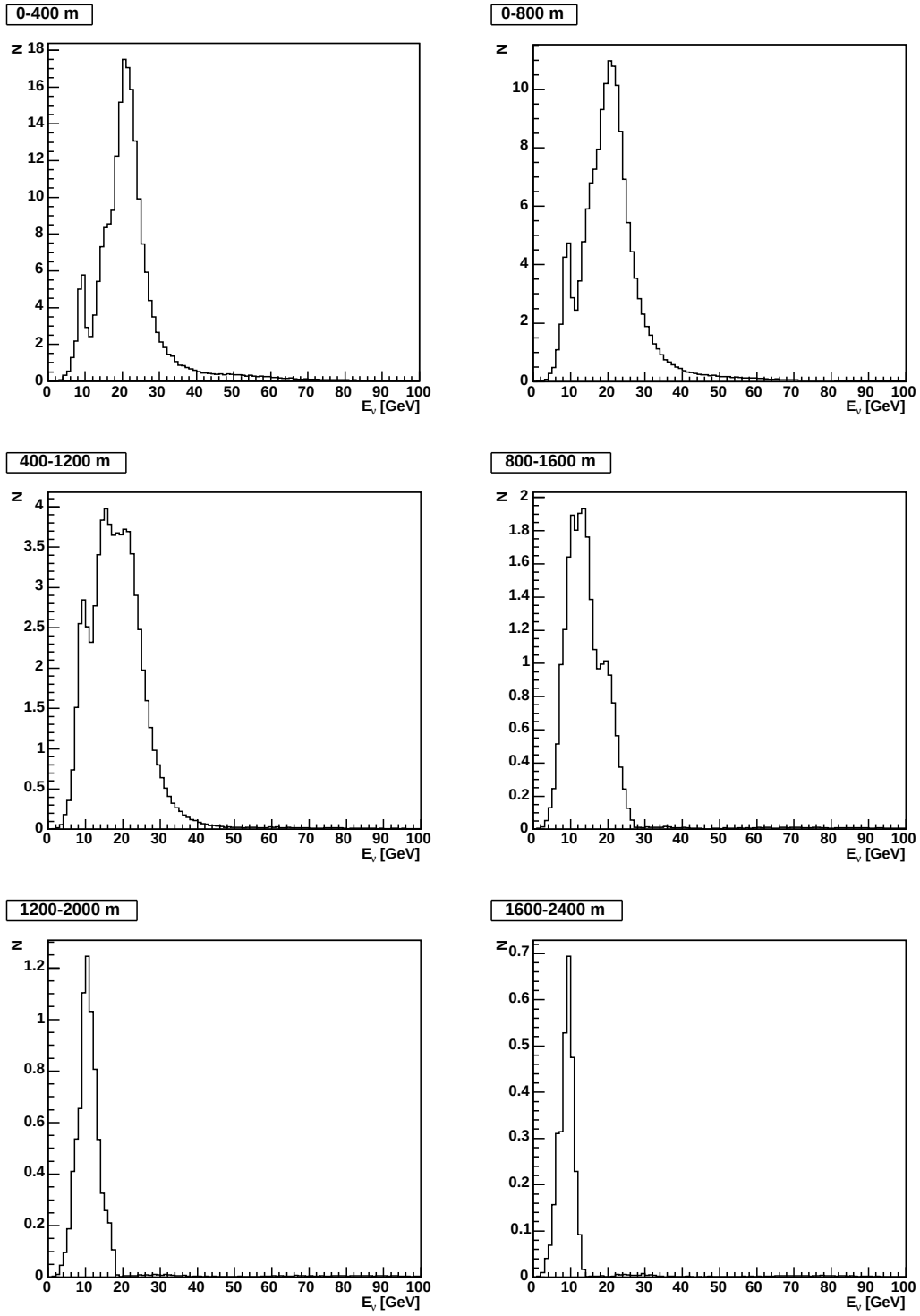

Figure 6.18: Neutrino fluxes for perfect focusing.

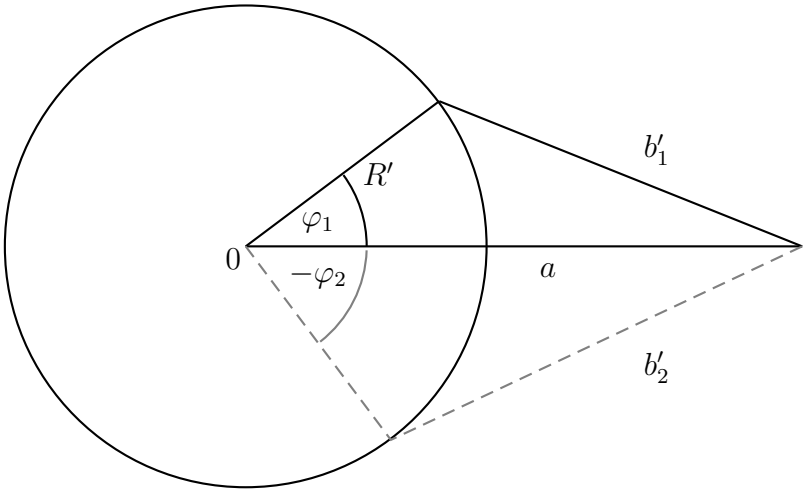

Figure 6.19: Method for moving the beam. The distance a of the parent meson axis to the beam axis can be determined from the FLUKA data. The emitted neutrino originally arrived at a radius R at Gran Sasso (not in this picture). To move the beam, the neutrino has to arrive at a shifted position R'. This happens, when the neutrino is emitted with an angle θ'_ν towards the parents axis. This angle θ'_ν corresponds to b'. Knowing b' and E_M, the energy E_ν can be calculated.

random value R' within $d \pm 400\,\mathrm{m}$. The results proved not to be very promising. The spectra for different R' are shown in Figure 6.20.

To quantify the goodness of the "far" versus the "extended" method, a χ^2 test of hypothesis has been done comparing the original data from the FLUKA simulation taken for $d = 400\,\mathrm{m}$ as described in the "near" method with the modified spectra for the same location. To gain comparable data, all spectra have been normalized first. Dividing the spectra into N bins, the χ^2 is given by:

$$\chi^2 = \sum_{i=1}^{N} \frac{(n_i - \nu_i)^2}{\nu_i}$$

where n_i is the content of the i^{th} bin of the reconstructed data and ν_i is the content for the original data. As expected, it turns out that the "far" method having a $\chi^2 = 0.000448678$ is by far better than the "extended" method with a $\chi^2 = 0.238433$.

6.4 Data Sensibility to the Detector Location in the Beam

Although no satisfying method to transfer the CC energy spectrum for off axis detector locations has been found, the detector sensibility to the changes of the beam profile described in both the "near" and the "far" method have been tested. Data from the "near" method has the advantage that it originates directly from the assumed correct FLUKA simulations and therefore provides a rather reliable method of simulating small

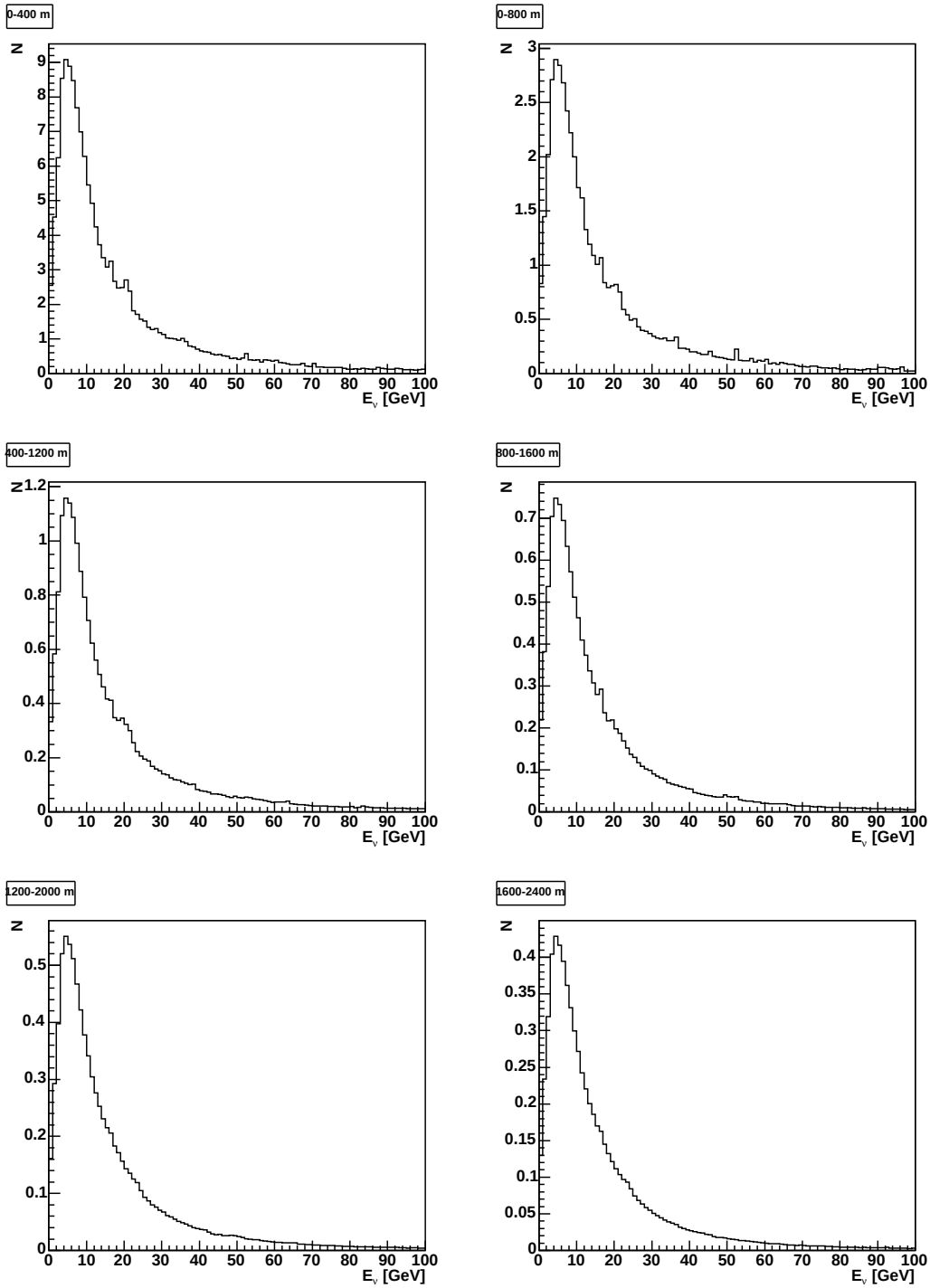

Figure 6.20: Neutrino spectra from extended FLUKA data.

d	N_{events}	correction
far, 400 m	25860	1.91517
far, 800 m	27718	1.80599
far, 1200 m	15967	3.10489
far, 1600 m	8067	6.24407
near, 100 m	29704	1.62261
near, 200 m	31506	1.5055
near, 300 m	23909	1.94013

Table 6.2: Number of events and corrections for the data samples generated for different off axis scenarios.

pointing inaccuracies. Simulations for detector locations at 100 m, 200 m and 300 m off axis at Gran Sasso have been made.

The "far" method neglects the fact that the parent mesons are not focused perfectly. For off axis locations relatively far from the center, these effects are assumed to cancel out for the further calculations. In the idealization of perfect focusing, a high flux is reached in the center of the beam which decreases significantly for off axis locations. As seen in the "near" method, the parents are by far not as perfectly focused, the beam is spread so that there is hardly any discrepancy in the flux for the center compared to a location at $d = 400$ m. Computing the flux with the "far" method, a reduction of the order 10^{-3} in both flux and the CC energy spectrum is observed. This contradicts the almost constant flux from the "near" method. It is therefore assumed that the "far" method merely describes the profile of the beam for large distances from the axis, no statement on the absolute flux can be made. To study the effects of this change in the CC energy spectrum, simulations with the "far" method for 400 m, 800 m, 1200 m and 1600 m have been made in this thesis.

6.4.1 Simulations of Off Axis CC Events

For all scenarios described above, simulations have been made using both FULL and OPERA geometry meaning that the whole detector with all surroundings is considered in the first case whereas only vertices in the detector are simulated in the latter. For the event generation, a set of 50 000 CC events has been taken. The CC energy spectra have been modified according to the methods described above. The resulting number of events and the correction factors are summarized in Table 6.2.

The generated CC energy spectra have been analyzed. Due to lepton number conservation, a muon is always created in a ν_μ CC process. The muon energy spectra for the different scenarios are shown in Figure 6.21. Table 6.4 shows the mean energy of the incoming muons. It has been tested whether these provide a way of determining the detector's displacement from the beam axis. For the muon spectra generated with the near method, no significant difference in neither flux nor the beam profile is noticed. The mean energy of the muons is equal for all location within 400 m of the beam center as summarized in Table 6.4.

Due to the described flaws of the "far" method, no comparison of fluxes could be made. However, the beam profile changes significantly for locations relatively far from

	$E_\nu < 30\,\mathrm{GeV}$	$E_\nu < 100\,\mathrm{GeV}$	$E_\nu < 400\,\mathrm{GeV}$
ν_μ	496	580	604
ν_e	2.26	5.02	5.44
$\bar{\nu}_\mu$	6.5	14.0	15.1
$\bar{\nu}_e$	0.13	0.33	0.38

Table 6.3: CC rate on isoscalar target per kton for 10^{19} pot on axis.

d	$\bar{E}_\mu$ [GeV]	N_{muons} F	$\bar{E}_\mu^{\mathrm{rec}}$ [GeV] F	N_{muons} O	$\bar{E}_\mu^{\mathrm{rec}}$ [GeV] O
far, 400 m	12.65	597	18.04	587	15.68
far, 800 m	11.89	534	14.72	545	14.82
far, 1200 m	11.09	511	13.04	523	12.74
far, 1600 m	10.40	484	11.45	525	12.41
near, 100 m	12.42	566	18.02	556	17.46
near, 200 m	12.42	617	17.98	569	17.55
near, 300 m	12.47	647	17.50	609	17.93

Table 6.4: Mean energy of muons generated in CC reactions - generated and reconstructed values and number of reconstructed muon momenta in the PT for both (F)ULL and (O)PERA geometry modes.

the beam center and so does the muon spectrum as can be seen in Figure 6.21. Also, the mean energy of the muons decreases for locations far from the center. For an on axis location, the mean energy of muons generated in a CC reaction is 12.4 GeV, for a detector location of 1600m from the axis, this goes down to 10.4 GeV. All mean energies for the studied scenarios can also be found in Table 6.4.

To study the effects of the differences in the muon spectrum, 2000 events from each generated data set have been simulated and digitized. The number of events had to be limited due to software problems in the simulation, data samples exceeding this range would cause the program to crash. A number of 2000 CC events in the bricks on axis corresponds to approximately 2.3×10^{19} pot which is close to the foreseen CNGS intensity of half a year. For off axis locations a larger number of protons on target is required to obtain such a number of events. This has to be considered in the analysis. For the simulation in FULL geometry mode including muons produced in the rock and Borexino, a decrease in the corresponding number of protons has to be accounted for when investigating absolute fluxes.

6.5 Results

Figure 6.22 shows two reconstructed spectra, one for a location simulated with the "near" method and one for the "far" scenario. Spectra for all simulated off axis locations can be found in Appendix D, next to a comparison with the initially generated spectra. Muon momenta could be reconstructed by the PT in about one third out of the 2000 generated events. Table 6.4 summarizes the number of reconstructed muons. The reconstructed spectra vary significantly from the generated muon spectra. This can partly be explained by geometrical effects. As described in Section 3.3.3, at least two track elements at two

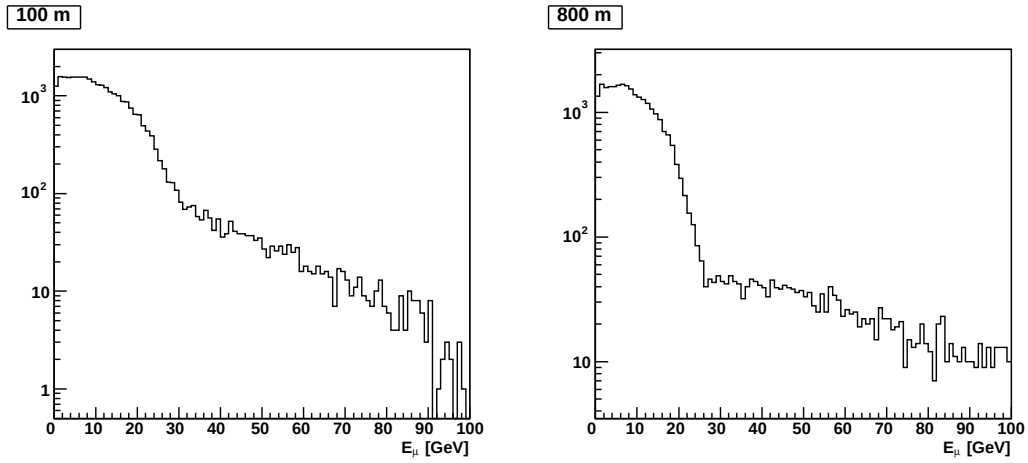

Figure 6.21: Generated muon spectra for one "near" and one "far" location.

stations	N_{hits}
1	644
2	642
3	776
1&2	635
2&3	784
1&2&3	589

Table 6.5: Occurrence of more than six hits per station in the reconstructed data. 587 momenta could be reconstructed.

sides of the magnet are required to determine the muons momentum via the deflection angle θ. Track elements have been found for almost all events by the reconstruction software. In many cases these were not sufficient for a reconstruction of the angle. An investigation of the number of hits for the different PT plane pairs or *stations* in front of, in between and behind the magnet showed indeed, that for only about one third of the events a sufficient number of hits could be found. The results are summarized in Table 6.5 exemplary for the 400 m far method reconstruction. A sufficient amount of hits is missing especially for low energy muons.

Missing detected low energy muons lead to a mean energy that is slightly higher than that of the generated muons. However, a decrease in the mean energy can be found in the reconstructed data. Hence, determination of a distance of the detector to the beam center is possible for large distances although high statistics are needed in order to obtain reliable information on the distance.

Due to the unsuccessful reconstruction of the CC muon energy spectrum, the determination of the muon cut off energy was not possible. However, the data indicates that this method might indeed be used for far locations when a satisfying identification of all muon energies is possible.

For the "near" method, the absolute flux could also be used to investigate the location of the detector towards the beam. For this the correction factors from the generation had to be considered. The corrected number of generated CC events always corresponds to

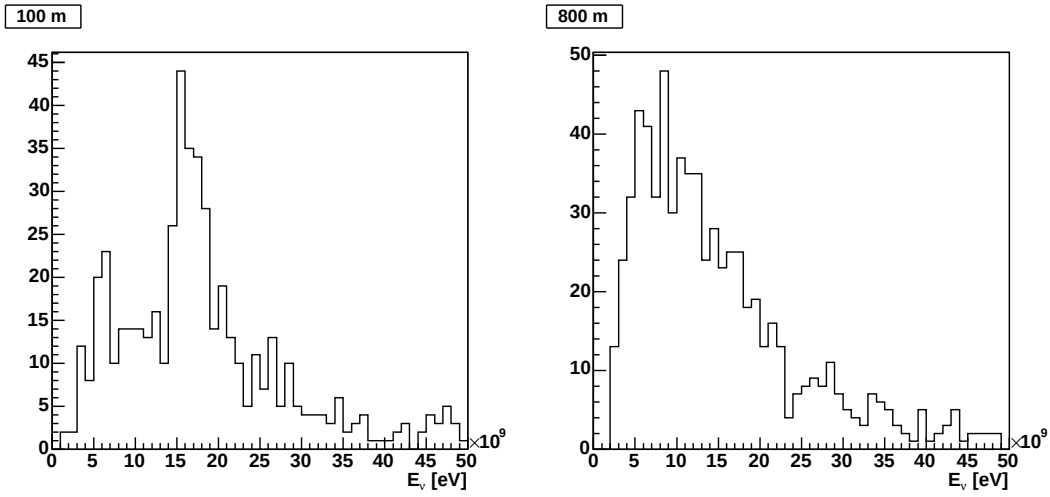

Figure 6.22: Reconstructed muon spectra for one "near" and one "far" location.

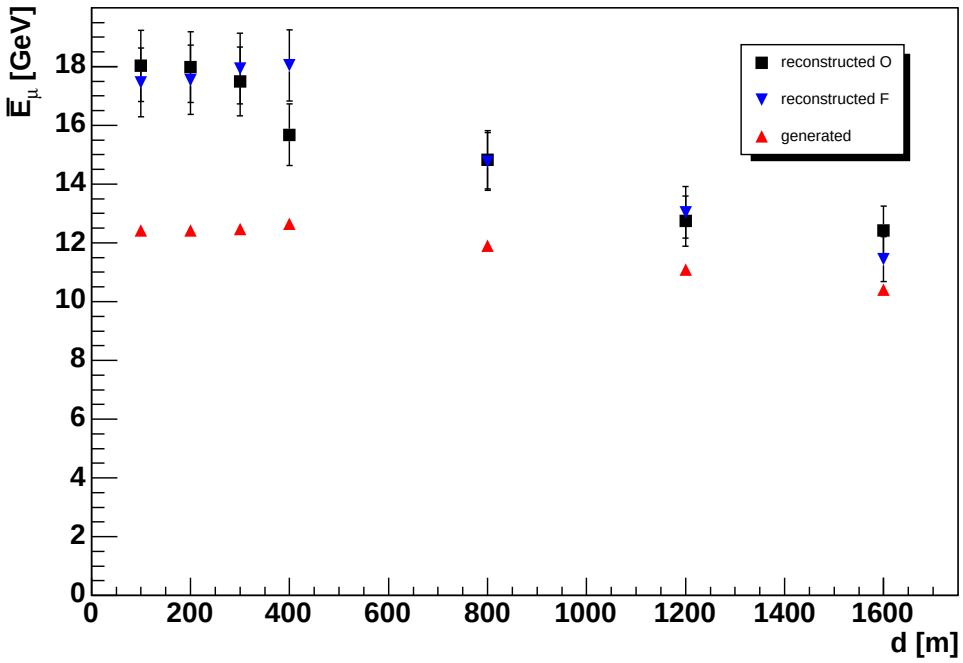

Figure 6.23: Generated and reconstructed mean energy of muons for FULL and OPERA geometry. Errors are multiplied by 10.

d	$N_{\text{generated,corrected}}$	$N_{\text{simulated}}$	N_{rec}	$N_{\text{rec,corrected}}$
100 m	48198	2000	556	535
200 m	47432	2000	569	539
300 m	46386	2000	609	528

Table 6.6: Reconstructed number of CC muon momenta detected by the precision tracker for different detector locations. The corrected numbers correspond to 2.3×10^{19} pot.

the same number of pot. However, for the simulation always 2000 CC events were taken hence corresponding to different values of pot. A normalization to the same value of pot has therefore been done. Again, a value of 2.3×10^{19} pot and thus 2000 corresponding on-axis events was chosen. The results are summarized in Table 6.6. Although the corrected number of generated events decreases slightly for larger distances from the beam axis, no significant difference in the reconstructed number of CC muons could be observed.

Chapter 7

Summary and Outlook

The OPERA detector started commissioning in late 2006. The precision tracker has been validated to be operational during the second run period in early November 2006. Data from cosmic muons has been taken during two runs and all components proved to be operational. A conversion of the PT raw data to the OpRelease file format has been implemented, providing the possibility of a quick access to data for analysis and reconstruction of events within the geometry of the OPERA detector.

Real data acquisition has successfully been tested for the precision tracker during all run periods performed so far. Successfully reconstructed tracks from cosmic muons show that the PT works as intended to. A first analysis of cosmic data from the second run period showed the functionality of all installed modules. Some noisy modules were found which could be explained by false threshold settings. Also some blind tubes have been identified which have been examined at Gran Sasso. The problem was caused by broken L3 amplifiers which have been replaced. Tracks from cosmic muons have to be analyzed and will be used for an overall alignment of all PT planes.

Determination of the detector's displacement with respect to the beam axis proved to be rather difficult. Significant changes in the beam profile only occur for large distances. Due to the small variance in the focusing of the beam, the flux is almost equal for locations close to the beam axis. CNGS claims to reach a geodesic alignment of 0.05 mrad [71]. This corresponds to a maximum distance of 36.6 m from the nominal beam axis at Gran Sasso. No effect of a pointing inaccuracy in this range could be found. In fact, no significant change in both flux and beam profile could be found for detector locations within a radius of 400 m from the beam axis. The studies done in this thesis provide good accuracy for the determination of flux and beam profile for distances in this range. For distances exceeding 400 m, only the beam profile could be studied. Here, a significant change in the beam profile and hence a dependence of the mean energy of muons produced in CC reactions could be observed in both the simulated and reconstructed data for different detector locations.

The results might be improved through a reconstruction of the muon energy spectrum with all sub-detectors. Especially the energy determination of low energy muons has to be improved. This would allow a better comparison of the mean muon energies to the ones predicted from the Monte Carlo simulations. Also, for great distances a determination of the detector location from the distinct cut off energies caused by neutrinos from different parent particles would be possible.

Further results might be obtained from the reconstruction of the incoming CC energy spectrum or even the incoming neutrino energy spectrum. The detector location could then also be determined through both the shape of the spectrum as well as the distinct cut off energies. Reconstruction of the neutrino spectra, however, requires high statistics and is as yet still preliminary.

Appendix A

Tools for Working with OpRelease

A.1 Accessing OPERA Data

Data stored in the OPERA file format can be conveniently accessed in the root framework. It has to be assured, that all the required environment variables of OpRelease are set correctly. This is in particular $OPRDATAROOT.

Before opening the OPERA file in within the root framework, the library for the OPERA format has to be loaded:

```
gSystem->Load("libOpRData.so")
```

Now the file can be opened as usual:

```
TFile operafile("<filename.root>")
```

Reading data

If the file contains a tree in the OPERA format, it can be given to the TreeManager. Depending on the content of the file, OPERA trees are e.g. named "TreeReal" for real data, "TreeMC" for Monte Carlo Data or "TreeMCD" for digitized Monte Carlo Data. The name of the tree has to be known.

```
TTree *theTree = (TTree*)(gROOT->FindObject("TreeReal"))
```

reads a tree with real data from file which can now be accessed as theTree.

```
TreeManager *treeManager = TreeManager::giveThis(theTree,"read")
```

initiates a TreeManager called treeManager to handle the tree. Data from the tree can now be accessed in different ways. In either way the lists for the sub-detectors (see Table 4.1) to be read out have to be initialized. This can either be done for a special event:

```
TList *SDTDigitList = treeManager->SDTDigitList(<eventnumber>)
```

or just generally:

```
TList *SDTDigitList = treeManager->SDTDigitList()
```

In the latter case the event number can than be specified separately:

```
treeManager->getEntry(<eventnumber>)
```

The single digits in a list can now be accessed as follows:

```
RSDTDigit *rSDTDigit = (RSDTDigit*)(SDTDigitList->At(<hitnumbe>))
```

It is now possible to access the data of a single hit, e.g.:

```
rSDTDigit->Tube()
```

for the tube number. For a list of the content of a digit see Table 4.2. Before reading another event, the TreeManager has to be cleared:

```
treeManager->clear()
```

Writing data

If data is to be written into an OPERA root file, the file has to be opened in write mode. A new tree has to be created

```
TTree *newTree = new TTree("TreeReal","OPERA Real Data")
```

and given to the TreeManager which has to be opened in write mode:

```
TreeManager *treeManager = TreeManager::giveThis(newTree,"write");
```

Again, lists for all sub detectors or the MC data have to be initialized, e.g.:

```
TList *SDTDigitList = treeManager->SDTDigitList()
```

for the precision tracker data. For each event, a digit has to be created:

```
RSDTDigit *SDTDigit = new RSDTDigit()
```

Now the data can be filled into the digit:

```
SDTDigit->SetTube(<tubenumber>)
```

When the digit is filled, it can be added to the list:

```
SDTDigitList->Add(SDTDigit)
```

If all digits for one event have been added to the lists they are given to the TreeManager:

```
treeManager->setSDTDigitList(SDTDigitList)
```

and finally filled into the tree:

```
treeManager->fill()
```

Before recording a new event, the TreeManager has to be cleared again:

```
treeManager->clear()
```

The last step is to finalize the tree:

```
treeManager->write()
```

Modifying data

When modifying data, the TreeManager can open two trees simultaneously, one for reading the original data and one for writing the modified data.:

```
TreeManager *treeManager = TreeManager::giveThis(oldTree,newTree)
```

Of course all trees have to be initialized first. A tool to cut data has been developed within this thesis using this function. Depending on the cut criteria whole events or single hits from an event can be removed from the Lists and digits with this tool.

A.2 Data Conversion

A described in Appendix B, ASCII data with TDC sensor numbers and channel numbers have to be mapped to SM number, plane number, layer number and tube number. A conversion tool to transform these values has been written within this thesis and is also used for the conversion done in the OpRelease data conversion from ASCII to root.

Appendix B

PT TDC Mapping

Each PT plane consist of either 15 or 17 modules. For each row, nine TDCs are reserved, two modules are connected to one TDC. The first TDC sensor id for the PT starts at 1052. For HPT four there is one exception, the last (17^{th}) module is not connected to sensor 1087, channels 1-48 but to sensor 1078, channels 49-96. The basic TDC mapping is shown in Figure B.1. Database readout provides both the sensor and channel id. A tool for converting these into HPT number (1-6), layer number (1-4), module number (1-15/17) and tube number (1-180/204) has been written. The routine for finding these values has also been included in the OPERA Software. Free TDC channels are used for RPC trigger time measurements, their mapping is as yet not final and thus not included here.

	sensor id	channel id	modules
HPT 1	1052-1058	1-96	1-14
	1059	1-48	15
HPT 2	1061-1068	1-96	1-16
	1069	1-48	17
HPT 3	1070-1077	1-96	1-16
	1078	1-48	17
HPT 4	1078	49-96	17
	1079-1086	1-96	1-16
HPT 5	1088-1095	1-96	1-16
	1096	1-48	17
HPT 6	1097-1103	1-96	1-14
	1104	1-48	15

Table B.1: Overview of the TDC mapping

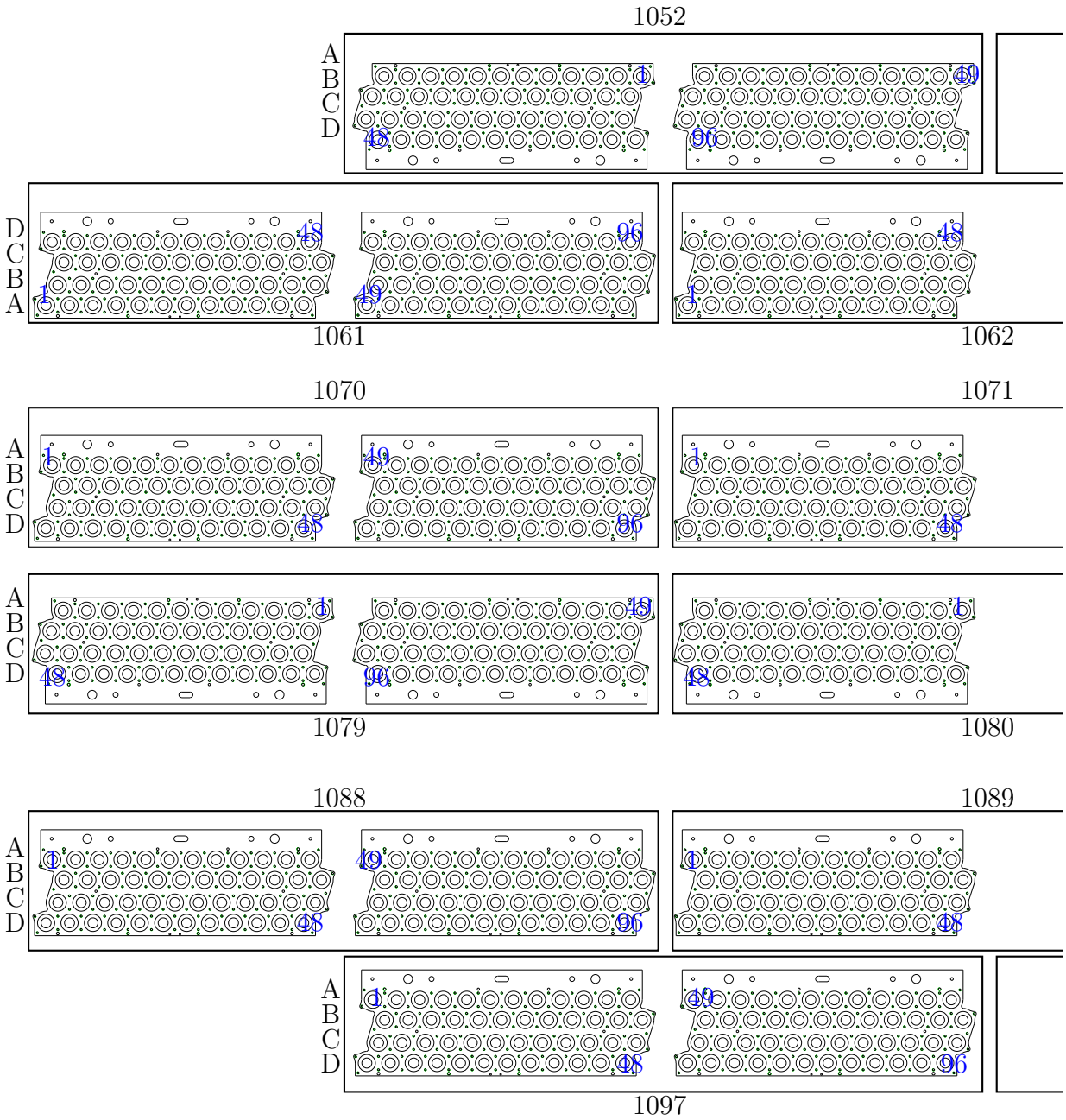

Figure B.1: TDC numbering scheme for super module 1. The rows represent from top to bottom HPT 1 through 6. Each black box shows the sensor id of the connected TDC. The letters on the side of each row indicate the cable labels. The blue numbers give an orientation for the channel number of each tube. Note that for TDC number 1087/1078 the cabling has been changed.

Appendix C

Overview of All Modules in SM1

To determine noisy modules, all 7149 events from the second run were analyzed. The distributions of hits per module for all 98 modules of SM1 are presented here.

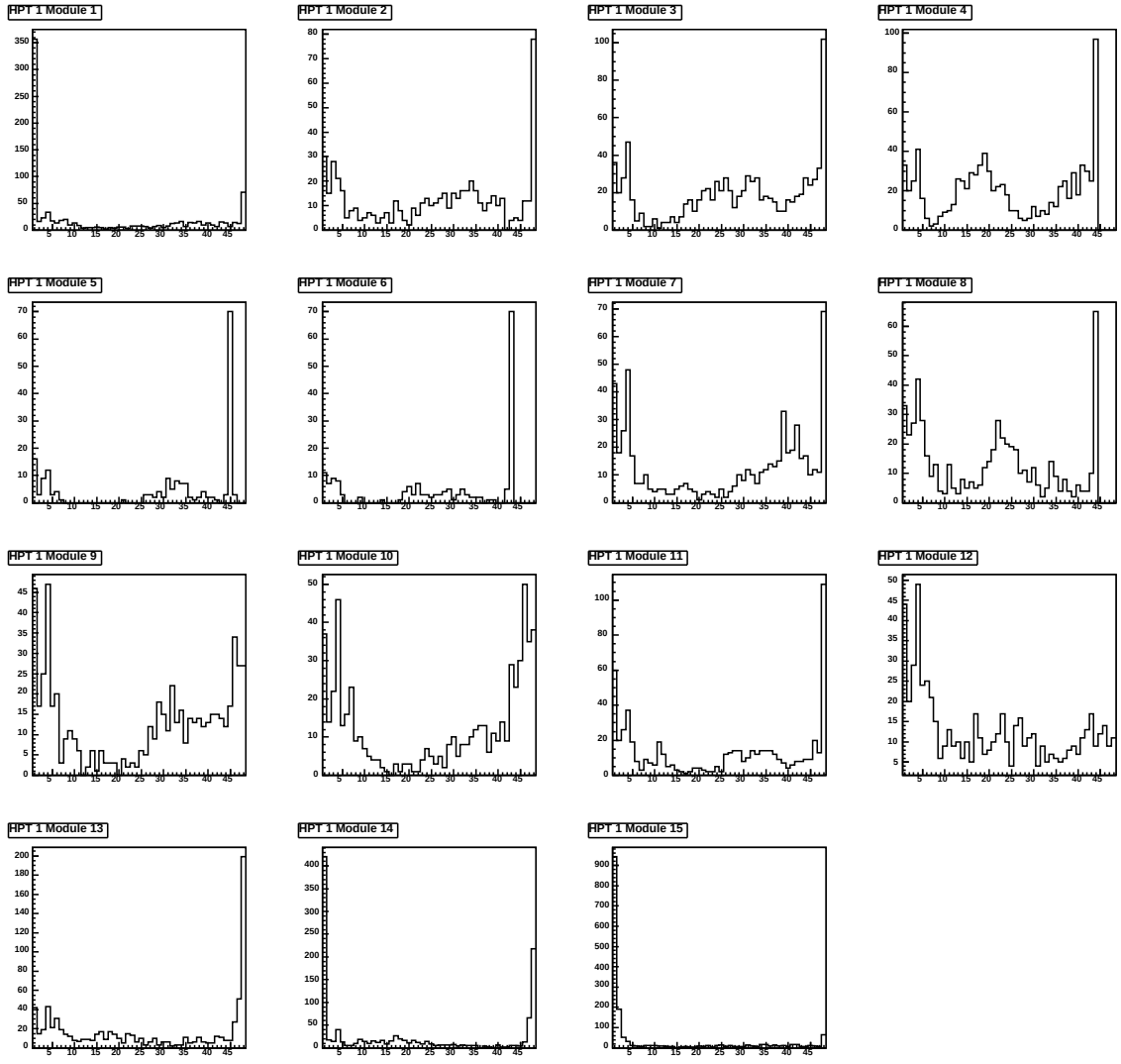

Figure C.1: Number of hits per module for HPT 1

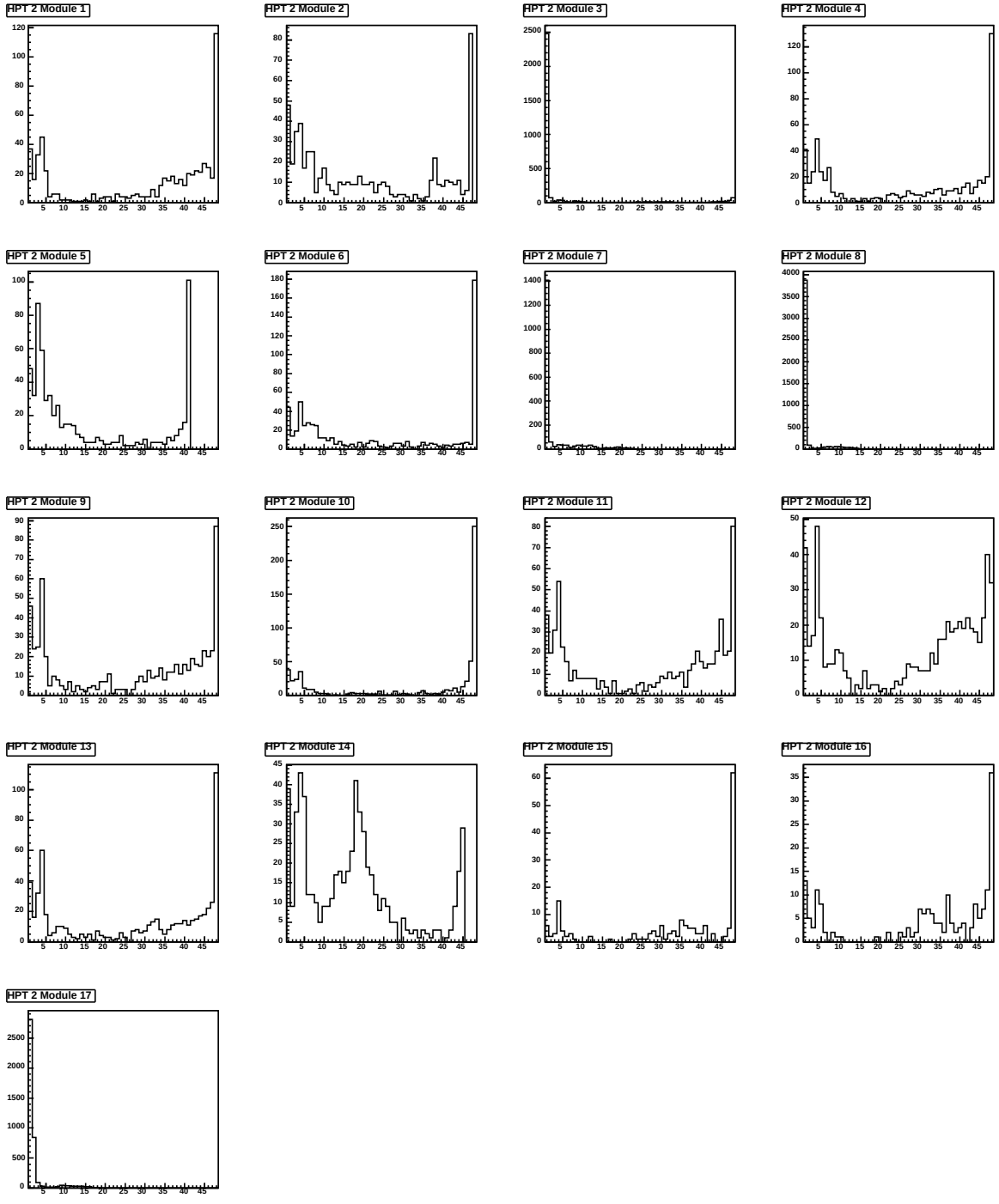

Figure C.2: Number of hits per module for HPT 2

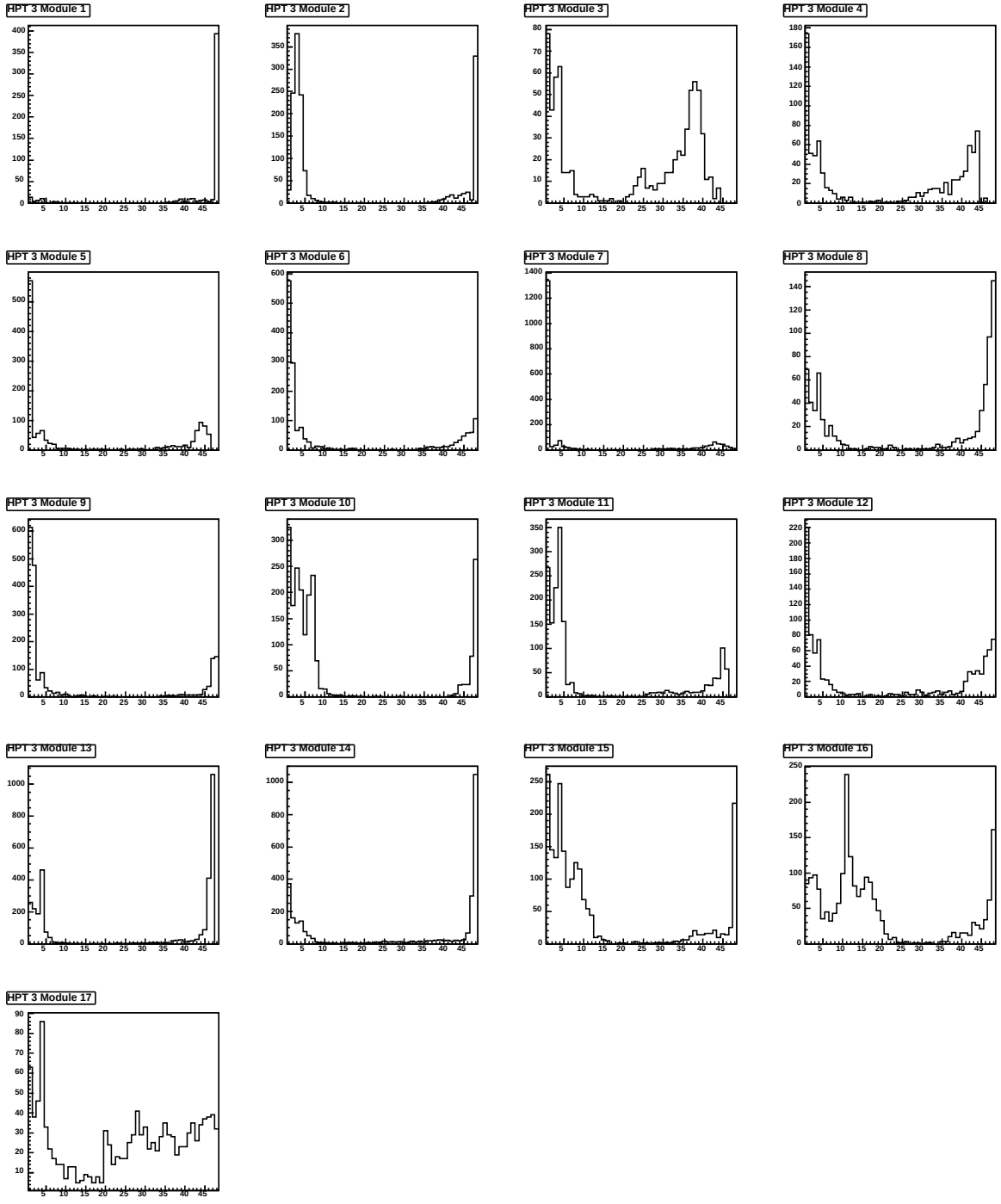

Figure C.3: Number of hits per module for HPT 3

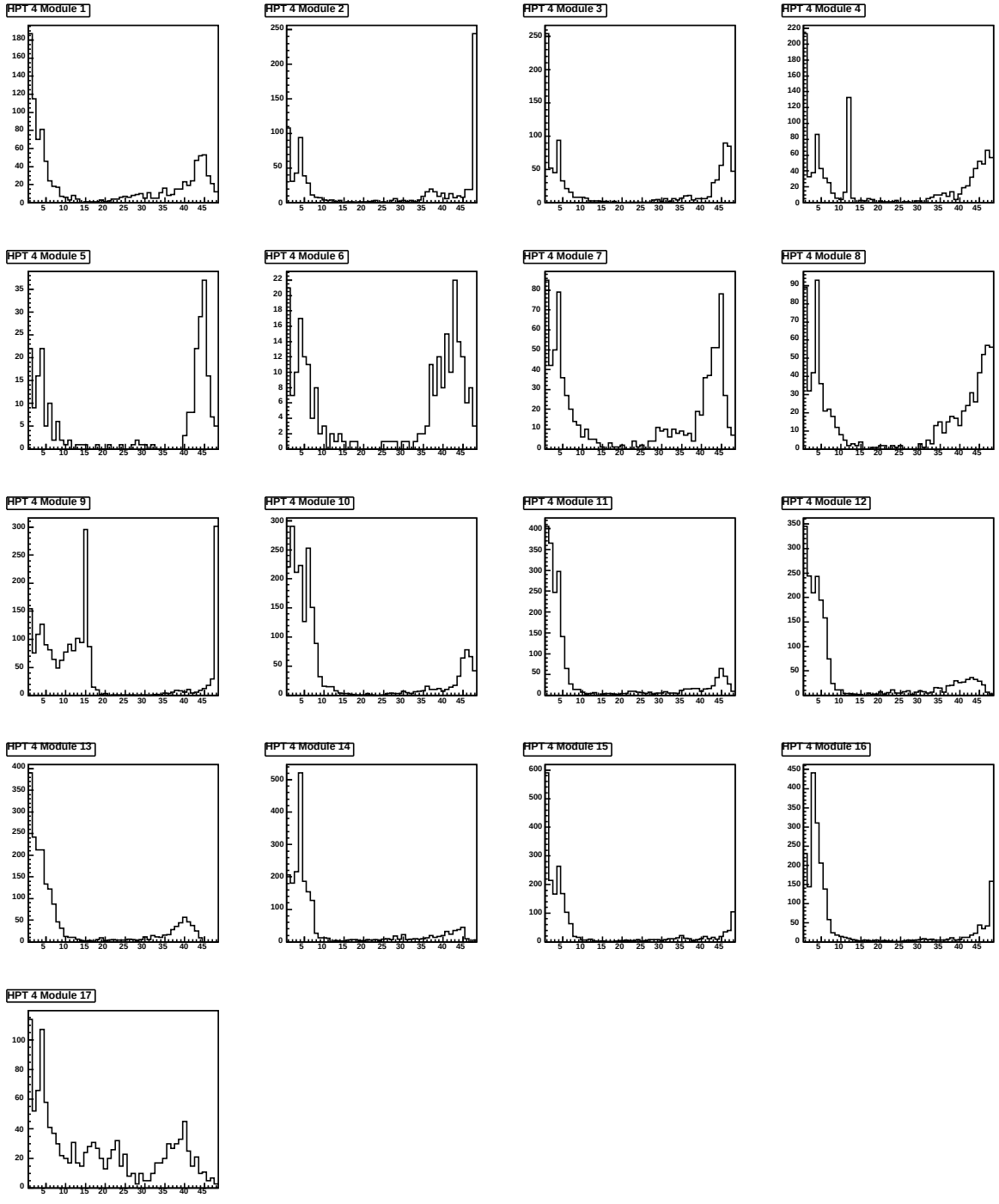

Figure C.4: Number of hits per module for HPT 4

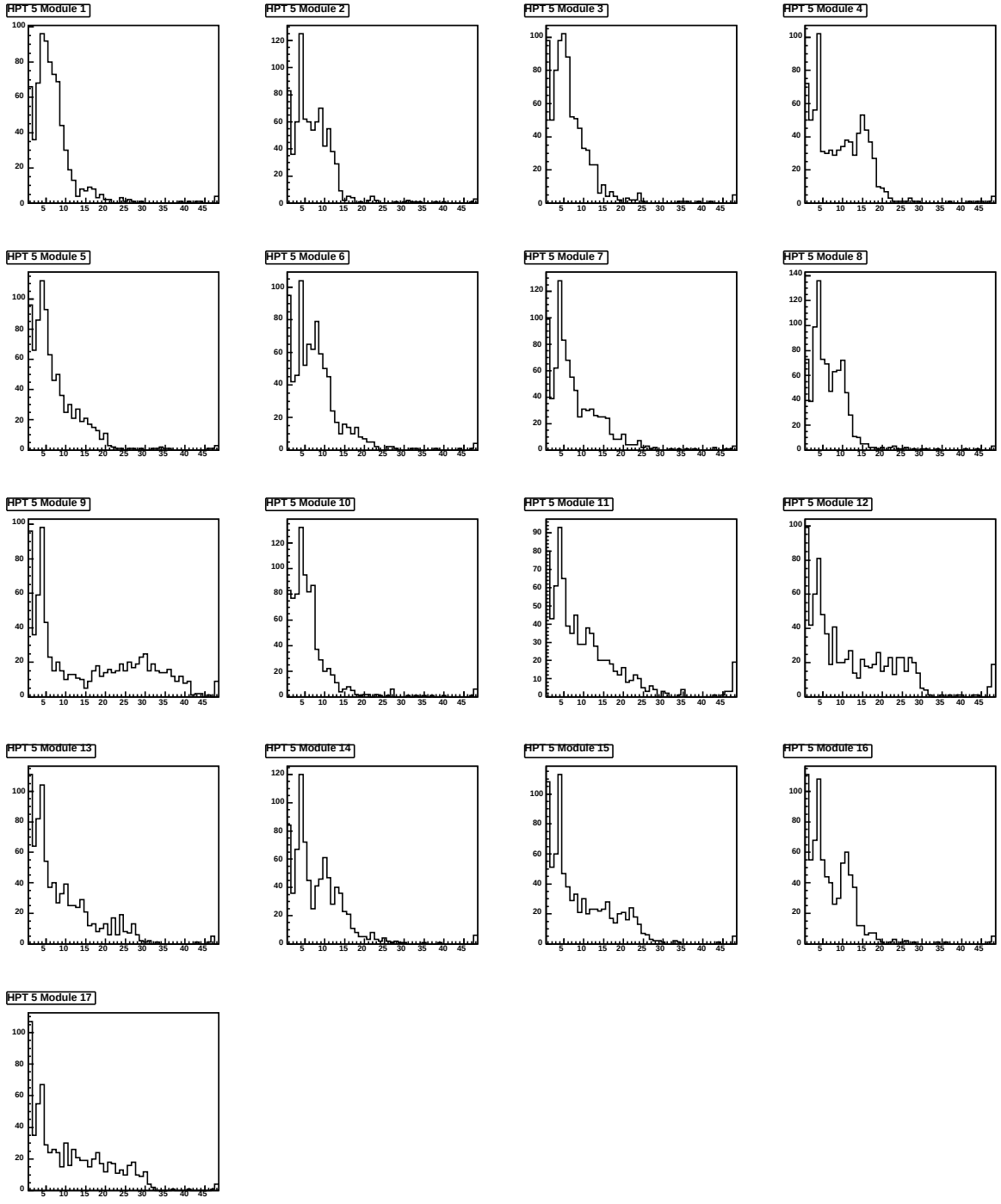

Figure C.5: Number of hits per module for HPT 5

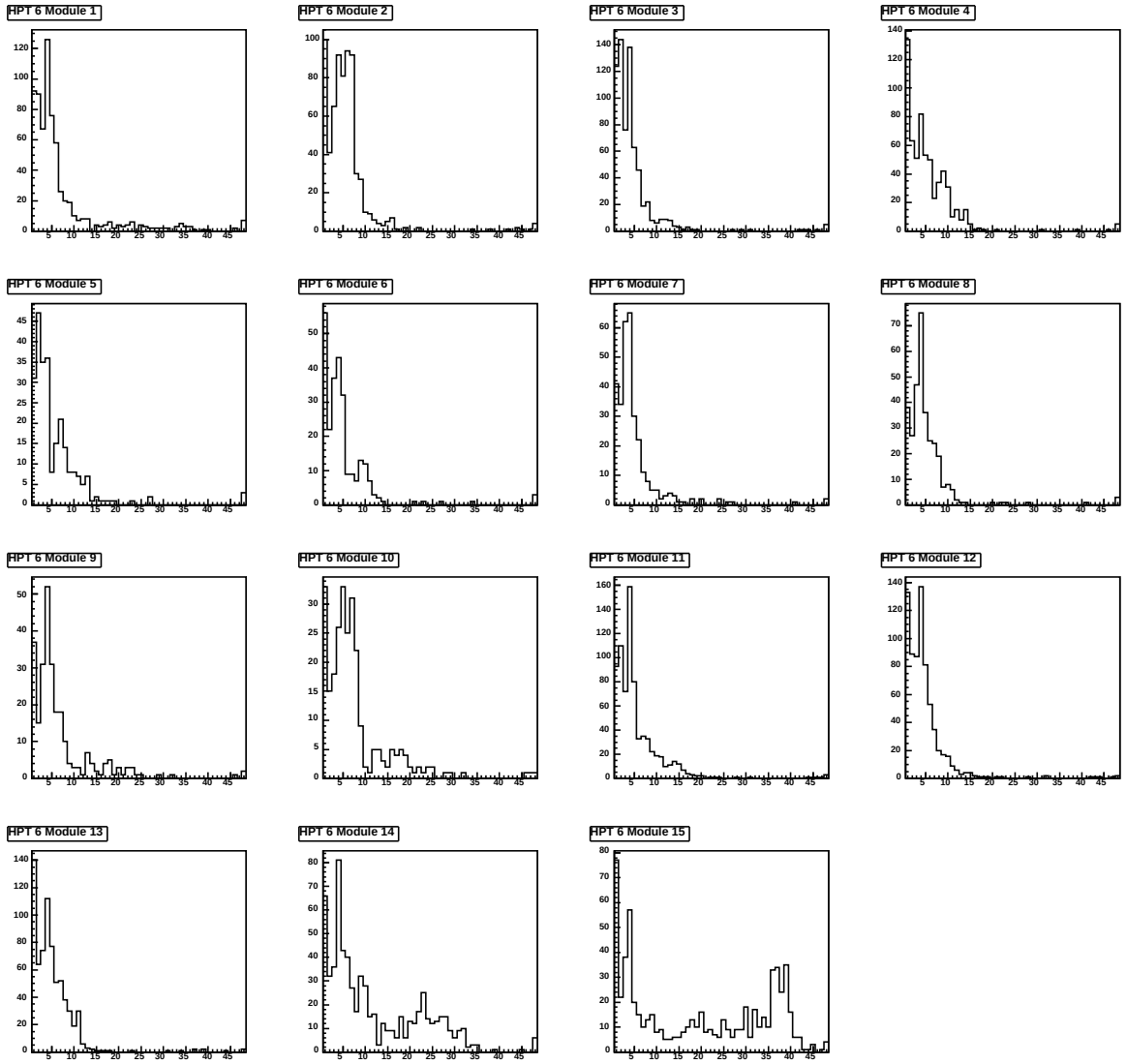

Figure C.6: Number of hits per module for HPT 6

Plane	Module	N.of Events	< 20	> 44	$= 48$
1	1	907	565	104	71
1	2	573	196	106	78
1	3	915	238	190	102
1	5	189	48	73	0
1	7	603	228	102	69
1	9	607	234	105	27
1	10	592	220	153	38
1	11	620	249	151	109
1	13	794	328	285	199
1	14	1154	699	301	218
2	1	622	191	184	116
2	2	594	321	93	0
2	4	606	236	182	130
2	6	612	310	197	179
2	9	636	244	153	87
2	10	596	174	335	250
2	11	643	264	156	80
2	12	608	226	109	32
2	13	628	239	177	111
2	15	179	39	69	62
2	16	187	47	59	36
3	1	508	44	411	393
3	2	1480	1016	382	329
3	5	1280	846	134	0
3	6	1572	1142	273	107
3	8	737	308	332	145
3	9	1785	1361	351	146
3	10	2045	1621	389	263
3	12	958	530	219	75
3	13	3102	1281	1559	0
3	14	2817	1029	1434	1049
3	15	1982	1556	271	217
3	16	2033	1542	278	161
3	17	1214	412	146	32
4	1	1031	593	116	12
4	2	828	387	290	244
4	3	997	561	278	47
4	4	1091	657	224	57
4	5	244	101	65	5
4	6	245	103	29	3
4	7	833	400	123	7
4	8	821	391	207	56
4	9	2108	1667	360	301
4	10	2100	1665	251	42
4	16	2057	1626	277	158

Table C.1: Possible noisy modules. For all modules in the list, more than 44 tube fired for at least 10% of the events. The table shows also the fraction of less than 20 tube hits per event as well as the number of events when all tubes fired. These noisy modules can be explained by false threshold settings. A problem in the CAN line was discovered. This has been corrected meanwhile.

Appendix D

Comparison of Simulated and Reconstructed Muon Spectra

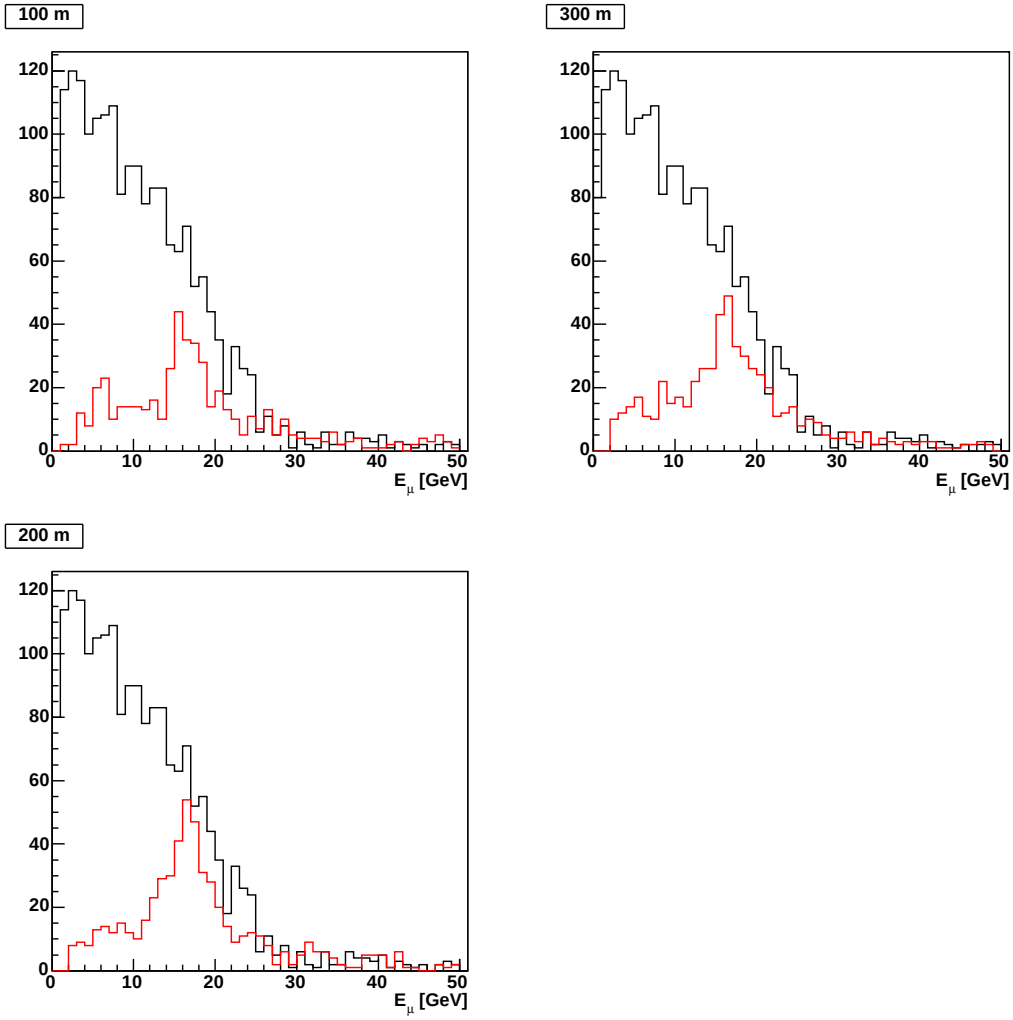

Figure D.1: Muon spectra for the near method. The black histogram shows the generated spectra, the red histogram shows the reconstructed muons.

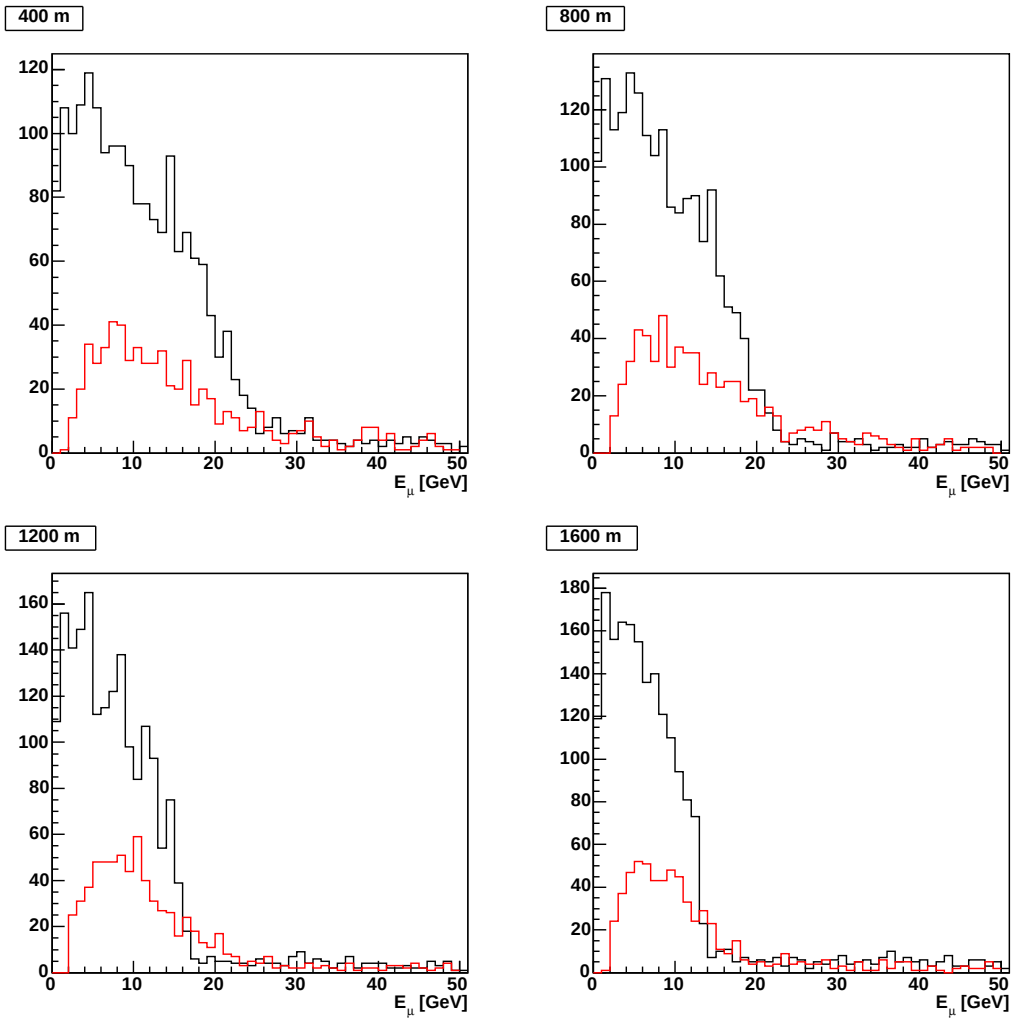

Figure D.2: Muon spectra for the far method. The black histogram shows the generated spectra, the red histogram shows the reconstructed muons.

Bibliography

[1] S. Weinberg, Phys. Rev. Lett. **19** (1967) 1264.

[2] W. Pauli, Wissenschaftlicher Briefwechsel mit Bohr, Einstein, Heisenberg, u.a., Vol. II: 1930-1939, ed, by K. v. Meyenn, (Springer-Verlag, Berlin 1985).

[3] F. Reines and C. L. Cowan, Nature **178** (1956) 446.

[4] G. Danby, J. M. Gaillard, K. Goulianos, L. M. Lederman, N. B. Mistry, M. Schwartz and J. Steinberger, Phys. Rev. Lett. **9** (1962) 36.

[5] M. L. Perl, SLAC-PUB-1652 *Presented at Symposium on New Directions in Hadron Spectroscopy, Argonne National Lab., Ill., Jul 7-10, 1975.*

[6] R. Rameika [DONUT Collaboration], *Prepared for 28th SLAC Summer Institute on Particle Physics: Neutrinos from the Lab, the Sun, and the Cosmos (SSI 2000), Stanford, California, 14-25 Aug 2000.*

[7] [ALEPH Collaboration], Phys. Rept. **427** (2006) 257 [arXiv:hep-ex/0509008].

[8] W. M. Yao *et al.* [Particle Data Group], J. Phys. G **33** (2006) 1.

[9] M. Goldhaber, L. Grodzins and A. W. Sunyar, Phys. Rev. **109** (1958) 1015.

[10] J. H. Christenson, J. W. Cronin, V. L. Fitch and R. Turlay, Phys. Rev. Lett. **13** (1964) 138.

[11] N. Cabibbo, Phys. Lett. B **72** (1978) 333.

[12] B. Pontecorvo, Sov. Phys. JETP **6** (1957) 429 [Zh. Eksp. Teor. Fiz. **33** (1957) 549].

[13] Z. Maki, M. Nakagawa and S. Sakata, Prog. Theor. Phys. **28** (1962) 870.

[14] V. N. Gribov and B. Pontecorvo, Phys. Lett. B **28** (1969) 493.

[15] L. Wolfenstein, Phys. Rev. D **17** (1978) 2369.

[16] H. A. Bethe, Phys. Rev. **55** (1939) 434.

[17] J. N. Bahcall, M. C. Gonzalez-Garcia and C. Pena-Garay, Phys. Rev. Lett. **90** (2003) 131301 [arXiv:astro-ph/0212331].

[18] R. J. Davis, D. S. Harmer and K. C. Hoffman, Phys. Rev. Lett. **20** (1968) 1205.

[19] B. T. Cleveland *et al.*, Astrophys. J. **496**, 505 (1998).

[20] J. N. Bahcall, A. M. Serenelli and S. Basu, Astrophys. J. **621** (2005) L85 [arXiv:astro-ph/0412440].

[21] P. Anselmann *et al.* [GALLEX Collaboration], Phys. Lett. B **285**, 376 (1992).

[22] A. I. Abazov *et al.*, Phys. Rev. Lett. **67** (1991) 3332.

[23] M. Altmann *et al.* [GNO Collaboration], Phys. Lett. B **616**, 174 (2005) [arXiv:hep-ex/0504037].

[24] K. S. Hirata *et al.* [Kamiokande II Collaboration], Phys. Rev. Lett. **63** (1989) 16.

[25] Y. Fukuda *et al.* [Kamiokande Collaboration], Phys. Rev. Lett. **77** (1996) 1683.

[26] J. Hosaka *et al.* [Super-Kamkiokande Collaboration], Phys. Rev. D **73** (2006) 112001 [arXiv:hep-ex/0508053].

[27] B. Aharmim *et al.* [SNO Collaboration], Phys. Rev. C **72** (2005) 055502 [arXiv:nucl-ex/0502021].

[28] S. N. Ahmed *et al.* [SNO Collaboration], Phys. Rev. Lett. **92**, 181301 (2004) [arXiv:nucl-ex/0309004].

[29] K. Scholberg [Super-Kamiokande Collaboration], [arXiv:hep-ex/9905016].

[30] Y. Fukuda *et al.* [Super-Kamiokande Collaboration], Phys. Rev. Lett. **81** (1998) 1562 [arXiv:hep-ex/9807003].

[31] Y. Ashie *et al.* [Super-Kamiokande Collaboration], Phys. Rev. D **71**, 112005 (2005) [arXiv:hep-ex/0501064].

[32] K. Abe *et al.* [Super-Kamiokande Collaboration], Phys. Rev. Lett. **97** (2006) 171801 [arXiv:hep-ex/0607059].

[33] M. Ambrosio *et al.* [MACRO Collaboration], Eur. Phys. J. C **36** (2004) 323.

[34] W. W. M. Allison *et al.* [Soudan-2 Collaboration], Phys. Rev. D **72** (2005) 052005 [arXiv:hep-ex/0507068].

[35] K. Eguchi *et al.* [KamLAND Collaboration], Phys. Rev. Lett. **90**, 021802 (2003) [arXiv:hep-ex/0212021].

[36] T. Araki *et al.* [KamLAND Collaboration], Phys. Rev. Lett. **94** (2005) 081801 [arXiv:hep-ex/0406035].

[37] M. Apollonio *et al.*, Eur. Phys. J. C **27** (2003) 331 [arXiv:hep-ex/0301017].

[38] F. Ardellier *et al.* [Double Chooz Collaboration], arXiv:hep-ex/0606025.

[39] C. Bemporad, G. Gratta and P. Vogel, Rev. Mod. Phys. **74** (2002) 297 [arXiv:hep-ph/0107277].

[40] K. Kaneyuki [K2K Collaboration], Nucl. Phys. Proc. Suppl. **145** (2005) 124.

[41] N. Tagg [MINOS Collaboration], eConf **C060409** (2006) 019 [arXiv:hep-ex/0605058].

[42] A. Aguilar *et al.* [LSND Collaboration], Phys. Rev. D **64** (2001) 112007 [arXiv:hep-ex/0104049].

[43] B. Armbruster *et al.* [KARMEN Collaboration], Phys. Rev. D **65** (2002) 112001 [arXiv:hep-ex/0203021].

[44] I. Stancu [MiniBooNE Collaboration], Nucl. Phys. Proc. Suppl. **155** (2006) 164.

[45] K. Assamagan *et al.*, Phys. Rev. D **53** (1996) 6065.

[46] R. Barate *et al.* [ALEPH Collaboration], Eur. Phys. J. C **2** (1998) 395.

[47] C. Kraus *et al.*, Eur. Phys. J. C **40** (2005) 447 [arXiv:hep-ex/0412056].

[48] C. Weinheimer, [arXiv:hep-ex/0306057].

[49] D. N. Spergel *et al.*, arXiv:astro-ph/0603449.

[50] J. F. Beacom and P. Vogel, Phys. Rev. D **58** (1998) 093012 [arXiv:hep-ph/9806311].

[51] P. Vogel, Prog. Part. Nucl. Phys. **48** (2002) 29 [arXiv:nucl-th/0111016].

[52] E. Majorana, Nuovo Cim. **14** (1937) 171.

[53] S. R. Elliott and J. Engel, J. Phys. G **30** (2004) R183 [arXiv:hep-ph/0405078].

[54] H. V. Klapdor-Kleingrothaus, A. Dietz, H. L. Harney and I. V. Krivosheina, Mod. Phys. Lett. A **16** (2001) 2409 [arXiv:hep-ph/0201231].

[55] H. V. Klapdor-Kleingrothaus, I. V. Krivosheina, A. Dietz and O. Chkvorets, Phys. Lett. B **586** (2004) 198 [arXiv:hep-ph/0404088].

[56] C. Arnaboldi *et al.*, Phys. Rev. Lett. **95** (2005) 142501 [arXiv:hep-ex/0501034].

[57] K. Kodama *et al.* [OPERA Collaboration], LNGS-LOI-19-99.

[58] R. Zimmermann [OPERA Collaboration], [arXiv:physics/0604101].

[59] K. Elsener [CERN] CERN-AC-Note-2000-03.

[60] G. Acquistapace *et al.*, CERN-98-02.

[61] T. Nakamura *et al.*, Nucl. Instrum. Meth. A **556**, 80 (2006).

[62] [OPERA Collaboration], New J. Phys. **8** (2006) 303 [arXiv:hep-ex/0611023].

[63] L. Arrabito *et al.*, Nucl. Instrum. Meth. A **568** (2006) 578 [arXiv:physics/0604043].

[64] M. Guler *et al.* [OPERA Collaboration], CERN-SPSC-2000-028.

[65] R. Santonico, R. Cardarelli, A. Di Biagio and A. Lucci, Nucl. Instrum. Meth. A **263** (1988) 20.

[66] S. Dusini, *Prepared for 9th ICATPP Conference on Astroparticle, Particle, Space Physics, Detectors and Medical Physics Applications, Villa Erba, Como, Italy, 17-21 Oct 2005.*

[67] F. Sauli, CERN-77-09.

[68] R. Zimmermann *et al.*, Nucl. Instrum. Meth. A **555** (2005) 435 [Erratum-ibid. A **557** (2006) 690].

[69] A. Fassò, A. Ferrari, J. Ranft, P. Sala

`http://www.mi.infn.it/~psala/Icarus/cngs.html` .

[70] R. Bailey, CERN-SL/99-034(DI), INFN/AE-99/05.

[71] A. E. Ball, F. Pietropaolo, P. R. Sala, N. Vassilopoulos, H. Vincke and A. Guglielmi, CERN-EP-2001-037.

Acknowledgments

I would like to thank my supervisor Prof. Dr. Caren Hagner for giving me the opportunity to write this thesis in the fascinating area of neutrino physics. Thanks go also to Prof. Dr. Walter Schmidt-Parzefall for the second opinion.

This thesis would not have been possible without my colleagues from the OPERA Hamburg working group. Many thanks go to Joachim Ebert for Finland stories and Acquasanta, Raoul Zimmermann for organizing the group's work, Benjamin Janutta for explanations of hardware details and Gin Tonic, Christoph Göllnitz for Kinder Delice, Torben Ferber for Heavy Metal, Benjamin Orth for "Sorry, I don't speak Italian.", Jan Lenkeit for all those neat little gadgets *we* now own, Jörn Boysen – Klippo!, and all the *new* diploma students: Matthias Frohwann, Burkhard Steinke, Michael Chabior, Carsten Kreyser and especially Eike Frank for inspiring ROOT talk and matrix element discussions. Special thanks go to Björn Wonsak for all the help with the OPERA software and his reconstruction.

Thanks go also to Richard Ford for the fascinating tour of SNO.

My interest in physics was greatly influenced by Lothar Ebeling-Brand whom I wish to thank for his enthusiasm in teaching this wonderful subject.

I would like to extend my gratitude to my many friends who have accompanied me through my studies and supported me during the making of this thesis, to name a few: Maik Brachmann for various travels, cooking and emails, Erik Butz for valuable hints and proof reading of this thesis „Jeden Tag so schnell... Jaaaa!", Björn Opitz for particles („Teilchen") and philosophy, Ole Roß for catering and logistics and all the stories, Christoph "Toffi" Lüdeling for more proof reading and LaTeX-tips, Tammo Gsänger for learning together and solving problems and Thorsten Ihler for legal advice, Ruben Meimbresse for giving me the feeling to achieve at least something when helping him with Linux issues during the making of my thesis and radiophonic support, the squash crew for keeping me fit, PoG for overcoming frontiers and of course all my other friends who are not mentioned here.

Love and thanks go to Susanne Schweighofer for her encouragement and for being that special someone.

And last but not least also to my family, especially my parents for their love and support.

Versicherung und Einverständniserklärung zur Veröffentlichung

Hiermit versichere ich, dass ich die vorliegende Diplomarbeit selbstständig und ausschließlich mit den angegebenen Quellen verfasst habe. Ferner erkläre mich mit der Bereitstellung der vorliegenden Diplomarbeit in den Bibliotheken des Instituts für Experimentalphysik und des Fachbereichs Physik der Universität Hamburg einverstanden.

Hamburg, den 14. Februar 2007